



HAL
open science

Viscoelastic properties of in vivo thigh muscle and in vivo phantom using magnetic resonance elastography (MRE)

Mashhour Chakouch

► **To cite this version:**

Mashhour Chakouch. Viscoelastic properties of in vivo thigh muscle and in vivo phantom using magnetic resonance elastography (MRE). Biomechanics [physics.med-ph]. Université de Technologie de Compiègne, 2015. English. NNT : 2015COMP2236 . tel-01376744

HAL Id: tel-01376744

<https://theses.hal.science/tel-01376744>

Submitted on 5 Oct 2016

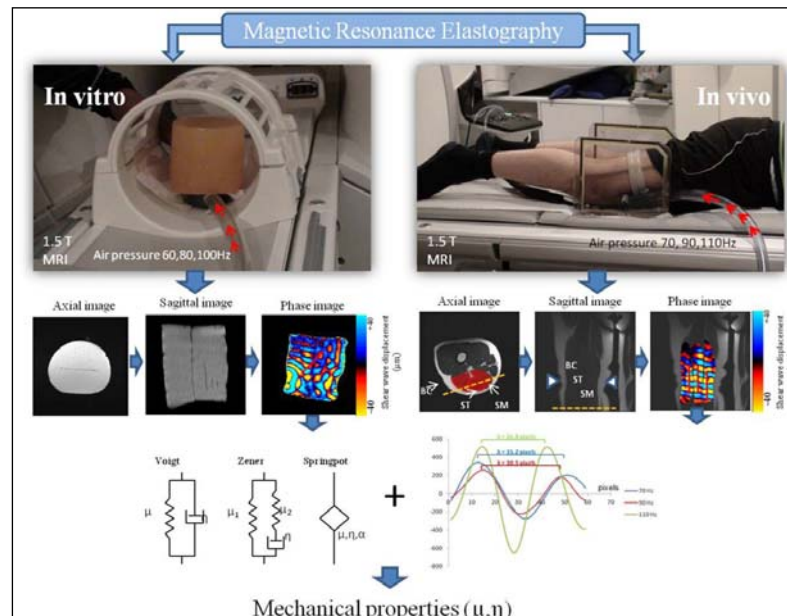
HAL is a multi-disciplinary open access archive for the deposit and dissemination of scientific research documents, whether they are published or not. The documents may come from teaching and research institutions in France or abroad, or from public or private research centers.

L'archive ouverte pluridisciplinaire **HAL**, est destinée au dépôt et à la diffusion de documents scientifiques de niveau recherche, publiés ou non, émanant des établissements d'enseignement et de recherche français ou étrangers, des laboratoires publics ou privés.

Par **Mashhour CHAKOUCH**

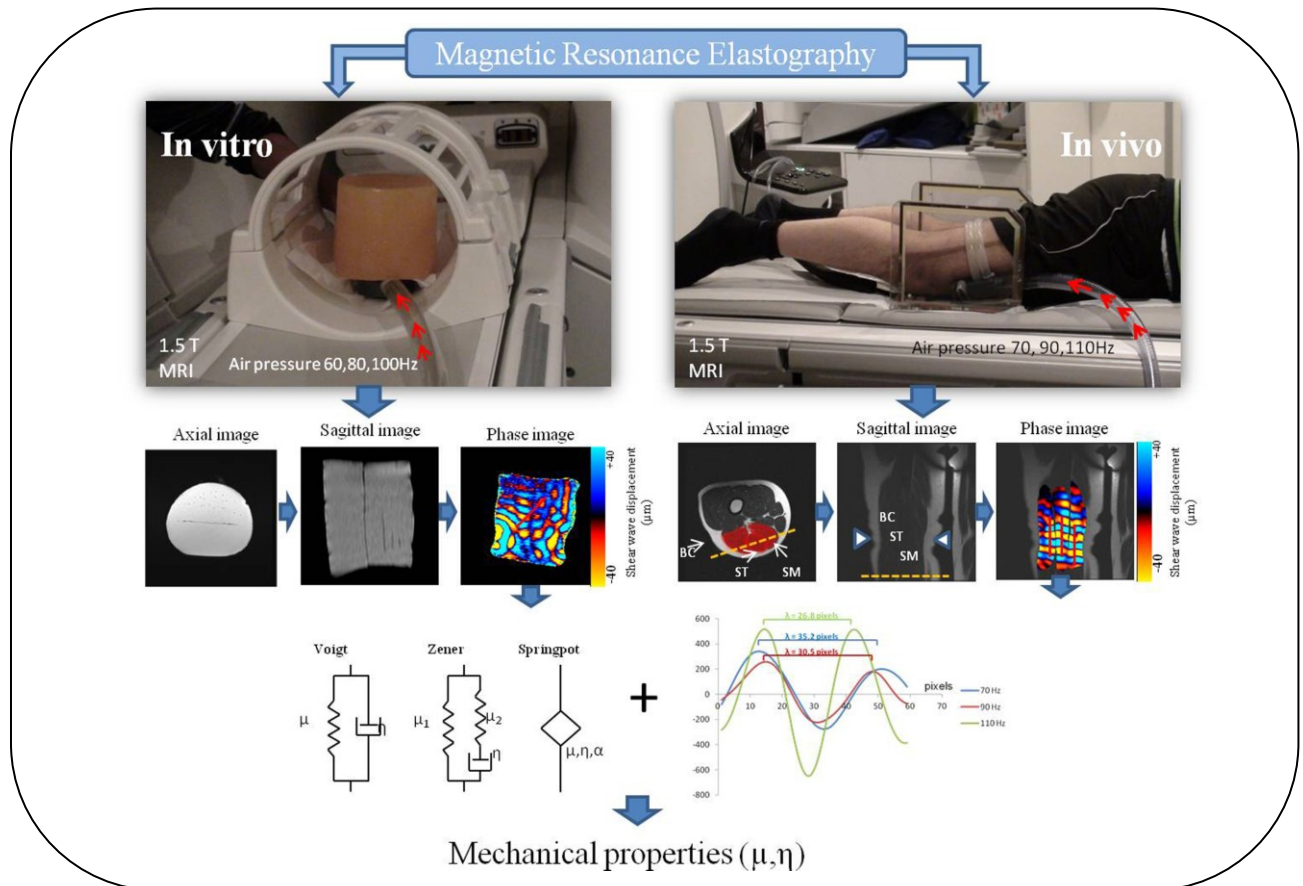
Viscoelastic properties of in vivo thigh muscle and in vitro phantom using magnetic resonance elastography (MRE)

Thèse présentée
 pour l'obtention du grade
 de Docteur de l'UTC



Soutenue le 07 décembre 2015
Spécialité : Biomechanics and Bioengineering

**Viscoelastic properties of in vivo thigh muscle and in vitro phantom using
magnetic resonance elastography (MRE)**



Jury Member

M. Jean-Marc Constans

Centre Hospitalier d'Amiens

Reviewer

M. Jean-Michel Franconi

Université Bordeaux 2

Reviewer

Mme. Marie-Christine Ho Ba Tho

Université de Technologie de Compiègne

Examiner

M. Fabrice Charleux

ACRIM-Polyclinique Saint Côme

Examiner

M. Philippe Pouletaut

Université de Technologie de Compiègne

Examiner

Mme. Sabine Bensamoun

Université de Technologie de Compiègne

Supervisor

Thanks

To...

FIGURES LISTS

<i>Figure 1.1: Types of skeletal muscles</i>	21
<i>Figure 1.2: The three types of muscle-tendon arrangement, a) the parallel-fibered muscle, b) the unipennate muscle and c) the bipennate muscle. P.C.S. marks the physiological cross-section that cuts all the fiber. Reprint from Gray's Anatomy (Gray et al., 1924)</i>	22
<i>Figure 1.3: Identification of slow and fast fibers, according to Kim and Choi, 2009</i>	23
<i>Figure 1.4: multi scale organization of the muscle system</i>	24
<i>Figure 1.5: Sarcomere structure</i>	25
<i>Figure 1.6: Axial image with the investigated thigh muscles. Quadriceps muscle (VL: vastus lateralis, VI: vastus intermedius, VM: vastus medialis, RF: rectus femoris), Sr: sartorius, Gr: gracilis, AD: adductor, hamstring muscles (ST: semitendinosus, SM: semimembranosus, BC: long and short biceps)</i>	26
<i>Figure 1.7: Schematic representation of muscle architecture.</i>	27
<i>Figure 1.8: Mechanical model of muscle Shorten-Hill (1987); CC: Contractile component, PEC: Parallel elastic component, SEC: Series elastic component</i>	29
<i>Figure 1.9: Different simplest cases of stresses and strains and their associated tensors (illustrated in 2D)</i>	31
<i>Figure 1.10: The principle of incompressibility. The volume of the incompressible object remains constant during (Lindberg, 2013).</i>	34
<i>Figure 1.11: Representation of the compression (A) waves and the shear (B) waves.</i>	37
<i>Figure 1.12: Variation of the mechanical compression and shear modulus of various biological tissues. Ranges associated with each modulus for a given tissue type are indicated by the shaded regions (Sarvazyan et al., 1998).</i>	38
<i>Figure 1.13: Rheological models used in the literature for the characterization of biological tissues. G^* is the complex shear modulus, μ is shear modulus, η is viscosity, f is the frequency and ω is the pulsation ($2.\pi.f$)</i>	40
<i>Figure 1.14: a: Custom built for the characterization of mechanical properties of liver (Schwartz et al., 2005). b: Experimental setup high speed cyclic testing rig. (A) Top platen; (B) bottom platen; (C) LVDT transducer; (D) static load cell; (E) dynamic load cell; and (F) connection with shaker (Van Loocke et al., 2009).</i> .	42
<i>Figure 1.15: Experimental setup for testing by indentation(Carter et al., 2001)</i>	44
<i>Figure 1.16: 1: the ultrasounds are successively focused at different depths to create pushes by radiation pressure. The constructive interferences of the shear waves form a supersonic Mach cone (in which the speed of the source is greater than the speed of the generated wave) and a quasi-plane shear wave is created; 2: the ultrasound machine then switch into an ultrafast imaging mode to follow the shear wave that is propagating through the medium (Gennisson et al., 2013).</i> .	48
<i>Figure 1.17: Shear waves velocity cartographies, obtained on the biceps brachii and brachialis by Supersonic Shear Imaging technology for different loads (Gennisson et al., 2010).</i>	49

Figure 1.18: The vibrator gives a low frequency pulse (adjustable from 10 Hz to 500 Hz) in the medium creating, among others, a shear wave. The ultrasound transducer, which is placed on the vibrator, thus allows following, by axial intercorrelation of the ultrasound speckle and more than one thousand times per second, the propagation of the shear wave depending on the depth over time. We can then deduce the speed of the shear wave and thus the Young's modulus of the medium (Gennisson et al., 2013). 49

Figure 1.19: Comparison between (a) the numerical simulation of the time/depth profile and (b) the time/depth profile in a muscle in vivo. The slope allows to work back to the speed of the shear wave and thus the Young's modulus of the medium (Gennisson, 2003). 50

Figure 1.20: The ultrasound array, mounted on a vibrator, gives a low frequency shock in the medium (around 50 Hz). The shear waves generated on the borders of the array interfere within the imaging plane as a quasi-plane wave propagating on the depth; 2: the ultrasound, then, switches into an ultrafast imaging mode to follow the shear wave , propagating through the medium (Gennisson et al., 2013). 51

Figure 1.21: a: breast elastography. An adenocarcinoma appears stiffer in the elasticity image (Bercoff et al., 2003). 51

Figure 1.22: The velocity of the shear wave in a human bicep contracted by various loads. . 52

Figure 1.23: MRE head driver with a loud speaker coupled with a long carbon fiber rod (Sack et al., 2008). 53

Figure 1.24: MRE liver driver with a loud speaker coupled with a plastic air-filled tube (Talwalkar et al., 2008) 54

Figure 1.25: MRE tests composed of a driver (tube) with a loud speaker coupled with a plastic air-filled tube (Bensamoun et al., 2006)..... 54

Figure 1.26: Schematic diagram of MRE sequence. Modified extracts (Manduca et al., 2001; Yin et al., 2007) 56

Figure 1.27: Images obtained during an MRE sequence: anatomical image (A) and phase image (B). The example is taken from a phantom..... 56

Figure 1.28: Measurement shear modulus (μ , kPa) from the calculation of the wavelength λ (mm) by placing a profile (red) in the direction of the wave propagation direction on the phase image. 57

Figure 1.29: MRE results for normal (35 volunteers) and fibrotic (48 volunteers) livers. Anatomical images for normal (a) and fibrotic (d) liver. Displacement images for normal (b) and fibrotic (e) liver. Stiffness maps for normal (c) and fibrotic (f) liver. (Yin et al. 2007) 61

Figure 1.30: Experimental data for shear moduli (A) and shear viscosity (B) acquired at 25 Hz (circles) and 50 Hz (triangles) wave excitation. The error bars correspond to the standard deviations of the data for each frequency and volunteer (Sack et al., 2008). 62

Figure 1.31: A:Principle of the mechanical excitation of shear waves inside the agar gel phantom, B:Phase image (G =shear modulus) (Hamhaber et al., 2003). 67

<i>Figure 1.32: A: example of actuator, B-C: MRE of transverse and longitudinal strain waves. The wavelength of longitudinal strain waves is longer than that of transverse strain waves. (Oida et al., 2004).</i>	67
<i>Figure 1.33: A: Setup of the MRE scan on an agarose gel phantom, B: A superior view of a MRE wave image for the cylindrical 2% agarose gel phantom at frequency of 150Hz. I. Round gel phantom in a container, II. The applicator of the electromechanical driver. The diameter of the tip is 10 mm, III. The electromechanical driver which is phase-coupled with oscillating the motion sensitizing gradient, IV. Head coil (Chen et al., 2005b).</i>	68
<i>Figure 1.34: Experimental setup for MRE heart phantom (Kolipaka et al., 2009b)</i>	68
<i>Figure 1.35: Magnetic Resonance Elastography (MRE) tests performed on a plastic phantom with a pneumatic driver (Leclerc et al., 2013b).</i>	69
<i>Figure 2.1: Manufacturing protocol for plastic phantoms</i>	92
<i>Figure 2.2: Fibers orientation</i>	93
<i>Figure 2.3: MRI sagittal acquisitions of the thigh muscles (A) (RF: rectus femoris, VI: vastus intermedius) and (B) the phantom showing similar structures.</i>	93
<i>Figure 2.4: Device to stretch the fibers</i>	94
<i>Figure 2.5: Set up of the hyper-frequency viscoelastic spectroscopy tests performed on the different small phantoms</i>	95
<i>Figure 2.6: MRE tests performed on the large phantom with two different drivers.</i>	96
<i>Figure 2.7: MRE Experimental set-up for the homogeneous phantom (a) (50% plastic). Phase images showing wave's displacement inside the phantoms at 60 Hz (b), 80Hz (c) and 100 Hz (d).</i>	97
<i>Figure 2.8: a: MRE tests performed on the homogeneous phantom (50%) showing the wave's displacement. B: Behaviors of the waves traveling along the red profile.</i>	98
<i>Figure 2.9: Illustration of the process for the evaluation of attenuation. a: Phase image with the propagation of the shear wave through the phantom where a profile (black arrow) is drawn in the direction of propagation. b: Amplitude of the profile along the distance x. c: Plot of the extrema of the amplitude profile and of the least-square fitted line for the calculation of the attenuation coefficient.</i>	100
<i>Figure 2.10: MRE setup placed inside a 1.5 T MRI machine. a: A participant laid supine on a custom-built ergometer to characterize the quadriceps (VL, RF, VI, and VM) and sartorius (Sr) muscles. b: Participant laid in prone position to analyze the ischio (ST, SM, BC) and gracilis (Gr) muscles. Waves were generated at 70 Hz, 90 Hz and 110Hz through a pneumatic driver (silicon tube) attached around the thigh muscles, where a coil was placed.</i>	104
<i>Figure 2.11: Illustration of the three MRE steps to obtain the phase image. A (step #1): The first column showed the orientation of the imaging plan (IP) as represented by a dashed line, within the target muscle. B (step #2): Sagittal images obtained from step #1 and represented the investigated muscles along the thigh. C (step #3): MRE sequence was performed on the selected sagittal image leading to the</i>	

<i>acquisition of the phase image, representing the displacement of the shear waves within the muscle.</i>	106
Figure 2.12: <i>Behavior of the shear wave ($f=90\text{Hz}$) along the profile placed in the gracilis (Gr) muscle.</i>	107
Figure 2.13 : <i>Phase images of Gr muscle at different frequencies (70, 90, 110 Hz)</i>	108
Figure 2.14: <i>Representation of the wavelengths (λ) measured within the gracilis (Gr) muscle, along the red profile, for the three frequencies (70, 90, 110 Hz).</i>	108
Figure 3.1: <i>A-B: phase images obtained from MRE tests performed on phantoms with different plastic concentrations. A_1-B_1: Behaviors of the waves traveling along the red profile.</i>	113
Figure 3.2: <i>A-B: Axial and sagittal anatomical images of the phantom (50%) where the fibers and plastic sheet are localized. Phase images obtained through MRE experiments performed at 90Hz with the round driver in contact with the media without inclusion (A_1-B_1) and with inclusion (A_2-B_2). Red arrows indicate the direction of the wave propagation.</i>	114
Figure 3.3: <i>A-B-C: Views of the axial (A) and sagittal (B) anatomical images of the phantom (50%) with inclusion and the muscle (C). A_1-B_1: Result of the MRE experiments (90Hz) performed with the tube driver attached around the phantom. C_1: MRE tests (90Hz) performed on thigh muscle. Wave direction indicated by arrows along the red profile.</i>	115
Figure 3.4: <i>Viscoelastic parameters (G', G'') measured by rheometer</i>	116
Figure 3.5 : <i>Behaviours of the wave obtained at 60, 80 and 100 Hz</i>	117
Figure 3.6: <i>Illustration of the three MRE steps to obtain the phase image. A (step #1): The first column showed the orientation of the imaging plan (IP) as represented by a dashed line, within the target muscle. B (step #2): Sagittal images obtained from step #1 and represented the investigated muscles along the thigh. C (step #3): MRE sequence was performed on the selected sagittal image leading to the acquisition of the phase image, representing the displacement of the shear waves within the muscle.</i>	119
Figure 3.7: <i>Visualization of clear and unclear wave propagation. A: Axial image with two different orientations of the imaging planes (IP#2, IP#3) through semimembranosus (SM) and semitendinosus (ST). Phase images showing clear (B) wave with measurable wavelength (λ) (C) and unclear (D) waves with non measurable wavelength (E). P1: Profile 1, P2: Profile 2.</i>	121
Figure 3.8: <i>Shear modulus (μ) with SEM obtained for the different thigh muscles and adipose tissues.</i>	122
Figure 3.9: <i>Phase images of Gr muscle at different frequencies (70, 90, 110 Hz)</i>	123
Figure 3.10: <i>Representation of the wavelengths (λ) measured within the gracilis (Gr) muscle, along the red profile, for the three frequencies (70, 90, 110 Hz).</i>	123
Figure 3.11: <i>Mean \pm SEM of the dynamic experimental viscoelastic parameters (a: G', b: G'' and c: G'/G'') measured with MRE at the three drive frequencies for the</i>	

semimembranosus (SM), semitendinosus (ST), biceps (BC), and gracilis (Gr) muscles. 124

Figure 3.12: Mean \pm SEM of the viscoelastic parameters (**a**: viscosity (η). **b**: elasticity (μ_1). **c**: elasticity (μ_2)) of the four thigh muscles (semimembranosus (SM), semitendinosus (ST), biceps (BC), and gracilis (Gr) muscles) obtained from the Zener model. (** $P < 0.05$, * $P < 0.1$). 126

Figure 3.13: Comparison of the viscoelastic parameters (mean \pm SEM) (**a**: ratio α . **b**: elasticity μ).of the four thigh muscles (semimembranosus (SM), semitendinosus (ST), biceps (BC), and gracilis (Gr) muscles) obtained from the springpot model. (** $P < 0.05$, * $P < 0.1$). 127

TABLES LISTS

<i>Table 1-1: List of conversions between Lamé coefficients, Young’s modulus, Poisson’s ratio, and C_{ij} for an isotropic elastic homogeneous medium</i>	34
<i>Table 1-2: In vitro compression tests performed on biological tissues</i>	43
<i>Table 1-3: Mean of the shear modulus (μ) of healthy muscles at rest and in contraction. Several muscles are mentioned such as biceps, flexor digitorum profundus (FDP), tibialis anterior (TA), medial gastrocnemius (MG), lateral gastrocnemius (LG), soleus (Sol), vastus lateralis (VL), vastus medialis (VM), Sartorius (Sr), and the quadriceps femoris (QF). “\perp” denotes the stiffness measured perpendicular to the muscle fibers, “\parallel” denotes stiffness measured parallel to the muscle fibers. MVC: maximum voluntary contraction.</i>	63
<i>Table 1-4: Mean of the shear modulus (μ) for pathological muscles at different condition. MVC: maximum voluntary contraction</i>	64
<i>Table 1-5: Viscoelastic properties of the phantoms using mechanical tests.....</i>	66
<i>Table 1-6: Elastic properties of the phantoms</i>	70
<i>Table 3-1: Experimental viscoelastic data for the large phantom (50%).....</i>	117
<i>Table 3-2: Summary of the viscoelastic parameters (G', G'') measured with MMRE and HFUS technique at three drive frequencies (mean \pm standard deviation).....</i>	118
<i>Table 3-3: Rheological model parameters (mean \pm SEM) and error of the fit measured from MMRE tests realized from four thigh muscles</i>	125

FIGURES LISTS	4
GENERAL INTRODUCTION	15
CHAPTER 1 LITERATURE REVIEW	17
A. The skeletal muscle architecture	20
1. Introduction	20
2. Different types of muscle in the body	20
3. Chemical composition of muscle	21
4. Multi-scale Structure of skeletal muscle	21
4.1 Organization of the muscle fiber	21
4.2 The functional unit of muscle	24
4.3 The thigh muscles	25
4.3.1 Composition of the thigh muscles	25
4.3.2 Determination of the morphological properties with imaging techniques	26
4.3.3 Aponeurosis	28
B. Mechanical properties of the muscle	28
1. Functional characteristics of skeletal Muscle Tissue	28
2. The Hill model	28
3. Hooke's law	30
4. Stress and strain Tensors	31
5. Tensor of elasticity in isotropic medium	31
6. Incompressible property	34
7. Propagation of waves in a soft material	35
8. Viscoelastic comportment	38
8.1 Elastic properties	38
8.2 Viscous properties	39
C. Techniques used for the characterization of the mechanical properties	42
1. In vitro methods	42
1.1 Compression tests	42
1.2 Indentation tests	44
1.3 Dynamic Mechanical Analysis (DMA)	44
1.4 Torque meter technique	45
2. In vivo methods	45
2.1 Palpation	45

2.2	Electromyography (EMG)	45
2.3	Myotonometric	46
2.4	Elastography techniques	46
2.4.1	Introduction	46
2.4.2	Ultrasound (US) elastography techniques.....	47
2.4.3	Magnetic resonance elastography (MRE) technique	52
	I. Introduction	52
	II. Description of the technique	53
2.4.4	Applications	60
D.	Phantoms developed for elastography.....	65
1.	Mechanical tests	66
2.	Magnetic resonance elastography Tests	67
3.	Mechanical properties	70
	References	71
	CHAPTER 2 MATERIELS AND METHODS	89
A.	Phantom study	92
1.	Phantom preparation	92
2.	Development of phantom with similar muscle architecture	93
3.	Development of a device to stretch the fiber	94
4.	Determination of the mechanical properties	94
	1. Hyper-Frequency Viscoelastic Spectroscopy (HFVS)	94
	2. Magnetic Resonance Elastography tests	95
	2.1 MR elastography set-up for the artificial muscle.....	95
	2.2 Multifrequency MRE set-up performed on the homogeneous phantom.....	96
	2.3 Phase Image processing and data analysis.....	98
	2.4 Summary of the different tests applied to the developed phantoms.	101
B.	Thigh muscle study.....	102
1.	Ethics Statement.....	102
2.	Participants.....	102
3.	Experimental configuration.....	102
4.	Acquisition of the anatomical and phase images of the muscle	105
5.	Phase Image Processing and Data Analysis.....	107
6.	Statistical analysis	109

CHAPTER 3 RESULTS	111
A. Phantom study	113
1. Elastic properties of the phantoms as a function of the:	113
1.1 Concentration of plastisol	113
1.2 Type of drivers	113
2. Viscoelastic properties of the phantoms:	116
2.1 Hyper-Frequency Viscoelastic Spectroscopy (HFVS) tests	116
2.2 Multifrequency MRE tests	117
B. Muscle thigh study	119
1. Propagation of the shear waves within the nine muscles	119
2. Comparison of the elastic property between the nine muscles at rest condition	121
3. Comparison of the viscoelastic property between the four muscles (ST, SM, BC, Gr) at rest condition using rheological model	122
CHAPTER 4	128
DISCUSSION AND PERSPECTIVES	128
A. Phantom study	130
B. Thigh muscle study	131
1. Elastic property	131
2. Viscoelastic property	133
CHAPTER 5	139
SUMMARIES	139
A. Summary of the in vitro studies	140
B. Summary of the in vivo studies	141
CHAPTER 6	142
RESUMES	142
A. Résumé de l'étude in vitro	143
B. Résumé de l'étude in vivo	144

GENERAL INTRODUCTION

GENERAL INTRODUCTION

Muscle is a biological tissue whose mechanical properties vary with activity. Skeletal muscles are vital in the normal activities of a human being. Their main functions are to produce force and cause motion. The real-time estimation of muscle contractile properties is difficult due to the changes that may exist between muscle size, morphology and the exercised force. There are many muscular disorders which affect muscle function or structure, e.g. spastic paraplegia, muscular dystrophies or myositis. Our knowledge of muscle changes in diseases and treatments remains incomplete. **Thus, the development of a non-invasive *in vivo* technique could provide information on a contracted or at rest muscle and will be essential to improve our understanding of muscle tissues.** Biopsies and palpations remain the conventional clinical tests to diagnose and to monitor (Hsieh et al., 2000; Lew et al., 1997; Palacio-Torralba et al., 2015a) diseases, respectively. However, these techniques are invasive and subjective.

MRE (Magnetic Resonance Elastography) is a non-invasive medical imaging technique, developed with magnetic resonance imaging (MRI) (Bensamoun et al., 2007; Brauck et al., 2007; Debernard et al., 2011a, 2011b; Dresner et al., 2001), which allows assessment of the shear elasticity of tissues by applying a mechanical or compression excitation. Motion-sensitive MR sequences have been introduced to analyze the propagation of shear waves created by this excitation, through soft tissues (Muthupillai et al., 1995). MRE was applied to different healthy (Green et al., 2013a) and pathological soft tissues (Bensamoun et al., 2007, 2011a; Serai et al., 2012; Venkatesh et al., 2008) in order to provide quantitative data to the clinician from superficial to deep areas. This data would track the evolution of a disease, to better know the pathophysiology of this disease, to choose the most suitable treatment and to evaluate long-term effects of treatment with a gain of tissue function.

Recent application of MRE has studied skeletal muscle biomechanics (Bensamoun et al., 2006a; Debernard et al., 2011a). **The aim of my thesis** is to develop experimental protocols to characterize the mechanical properties of healthy thigh muscles with MRE technology (Magnetic Resonance Elastography). A better knowledge of muscle behavior, through analysis of its mechanical properties, will improve the diagnosis, the treatment, and the follow-up of muscle disorders. Thus, a database of the muscle viscoelastic properties (G' , G'') have been constituted with the passive state of the thigh muscles.

In parallel to this in vivo study, phantoms are developed with similar mechanical and structural properties to the investigated muscles. This test-objects will enable to test, MRE parameters, MRE sequence, and to develop new protocols before to apply in vivo the MRE muscle test. The particularity of the laboratory BioMechanic and Bioengineering (BMBI), where this PhD project belongs, is to associate experimental and numerical research. Thus, the present experimental functional properties will be used for the numerical model.

This manuscript is composed of four chapters.

The first one will be devoted to some anatomical reminders on the muscle tissue, followed by a state of the art of the experimental techniques used for the mechanical characterization of muscle (in vivo) and phantom (in vitro).

In the second chapter, the different materials and methods developed in this study will be explained through two parts:

The first in vitro part is devoted to the development and characterization of a test object, which has the same structural and mechanical properties as the muscle.

The second in vivo part aims at developing experimental MRE protocols to determine the viscoelastic properties of healthy thigh muscles.

The third chapter will present the results of these experimental in vitro and in vivo analyses.

The fourth chapter will provide a discussion of all the results, with the future experiments follow-up by **the fifth chapter** composed of a conclusion.

CHAPTER 1

LITERATURE REVIEW

CHAPTER 1	LITERATURE REVIEW	17
A.	The skeletal muscle architecture	20
1.	Introduction	20
2.	Different types of muscle in the body	20
3.	Chemical composition of muscle	21
4.	Multi-scale Structure of skeletal muscle	21
4.1	Organization of the muscle fiber	21
4.2	The functional unit of muscle	24
4.3	The thigh muscles	25
4.3.1	Composition of the thigh muscles	25
4.3.2	Determination of the morphological properties with imaging techniques	26
4.3.3	Aponeurosis	28
B.	Mechanical properties of the muscle	28
1.	Functional characteristics of skeletal Muscle Tissue	28
2.	The Hill model	28
3.	Hooke's law	30
4.	Stress and strain Tensors	31
5.	Tensor of elasticity in isotropic medium	31
6.	Incompressible property	34
7.	Propagation of waves in a soft material	35
8.	Viscoelastic compartment	38
8.1	Elastic properties	38
8.2	Viscous properties	39
C.	Techniques used for the characterization of the mechanical properties	42
1.	In vitro methods	42
1.1	Compression tests	42
1.2	Indentation tests	44
1.3	Dynamic Mechanical Analysis (DMA)	44
1.4	Torque meter technique	45
2.	In vivo methods	45
2.1	Palpation	45
2.2	Electromyography (EMG)	45

2.3	Myotonometric.....	46
2.4	Elastography techniques	46
2.4.1	Introduction.....	46
2.4.2	Ultrasound (US) elastography.....	47
2.4.3	Magnetic resonance elastography (MRE) technique	52
I.	Introduction	52
II.	Description of the technique.....	53
2.4.4	Applications	60
D.	Phantoms developed for elastography.....	65
1.	Mechanical tests	66
2.	Magnetic resonance elastography Tests.....	67
3.	Mechanical properties	70
	References	71

A. The skeletal muscle architecture

1. Introduction

Muscle tissues are a system capable of changing its length, exert force and convert chemical energy to mechanical energy. The tissues that generate movements of the human body are the striated or skeletal muscles. The body contains over 600 skeletal muscles representing 40-50% of the total weight of the human body (Bonnell et al., 2009). The contraction of skeletal muscle, placed under the control of the somatic nervous system, doesn't only allows humans to move in its environment, to control, modify, seize and move objects but also, it plays an important role in body temperature regulation.

2. Different types of muscle in the body

There are three types of muscles in the human body, namely the smooth muscle, the cardiac muscle, and the skeletal muscle (Figure 1.1).

- The skeletal muscle tissues:

Skeletal muscles form approximately 40 % of the body weight in men and 32 % of that in women (Sherwood, 2015). Their function is to engage and to mobilize the skeleton. They are the third key element of the locomotor system. This muscle is called "striated" because its macroscopic observation suggests parallel streaks with each other. Its activity is voluntary and is dependent on the somatic nervous system. Skeletal muscle is an essential component of the body and is primarily responsible for the production of the movement.

- The smooth muscle tissues:

They are found in the walls of the organs, vessels and bronchi. Their work is independent of their wills and therefore is under the control of the autonomic nervous system.

- The heart muscle tissues:

They are striated and their activity is involuntary, but under the control of the autonomic nervous system. Although there are significant differences in structures, mechanical properties and control mechanism between these three types of muscles.

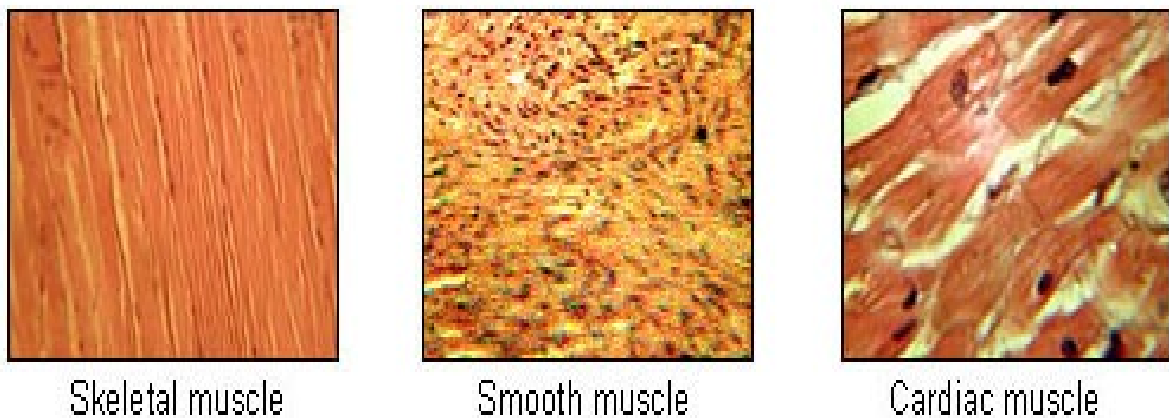


Figure 1.1: Types of skeletal muscles

3. Chemical composition of muscle

The skeletal muscle is constituted of about 75% water and 20% protein; the rest consists of inorganic salts and other substances such as high energy phosphate, urea, lactic acid and various minerals, enzymes and pigments, ions, amino acids, fats and sugars.

The most abundant muscle proteins are myosin, actin and tropomyosin. They represent respectively 52%, 23% and 15% of the muscle protein content. In addition, it is about 700 mg of myoglobin per 100 g of muscle tissue (Robertson, 1961)

4. Multi-scale Structure of skeletal muscle

4.1 Organization of the muscle fiber

- **Circular Muscles:** These muscles appear circular in shape and are normally sphincter muscles which surround an opening such as the mouth and the eyes.
- **Convergent Muscles:** These are muscles where the origins (the attachment to a fixed bone, usually the proximal attachment) are wider than the point of insertion. This fiber arrangement allows a maximum force production.
- **Parallel or Fusiform Muscles:** Parallel muscles have fibers which run parallel to each other and are sometimes called strap muscles such as biceps femoris, semitendinosus, gracilis, biceps brachii and sartorius. They cause large movement because they are long muscles which are not very strong but have good endurance.

- **Pennate Muscles:** Muscles with fibers that run oblique to insert the tendon are called *pennate* muscles. They can be divided into:
 - **Unipennate** muscles have their fibers arranged in a diagonal direction to insert onto the tendon that allow great strength such as vastus medialis and vastus lateralis,
 - **Bipennate** muscles have two rows of muscle fibers which are placed in opposite diagonal directions, allowing a high power but a less range of motion such as rectus femoris.
 - **Multipennate:** As the name suggests multipennate muscles have multiple rows of diagonal fibres with a central tendon that are inserted into two or more tendons.

The physiological cross-section (P.C.S), which is the area that cuts all the fiber of the muscle and often used to approximate the number of muscle fibers, is much larger in pennate muscles (Figure 1.2).

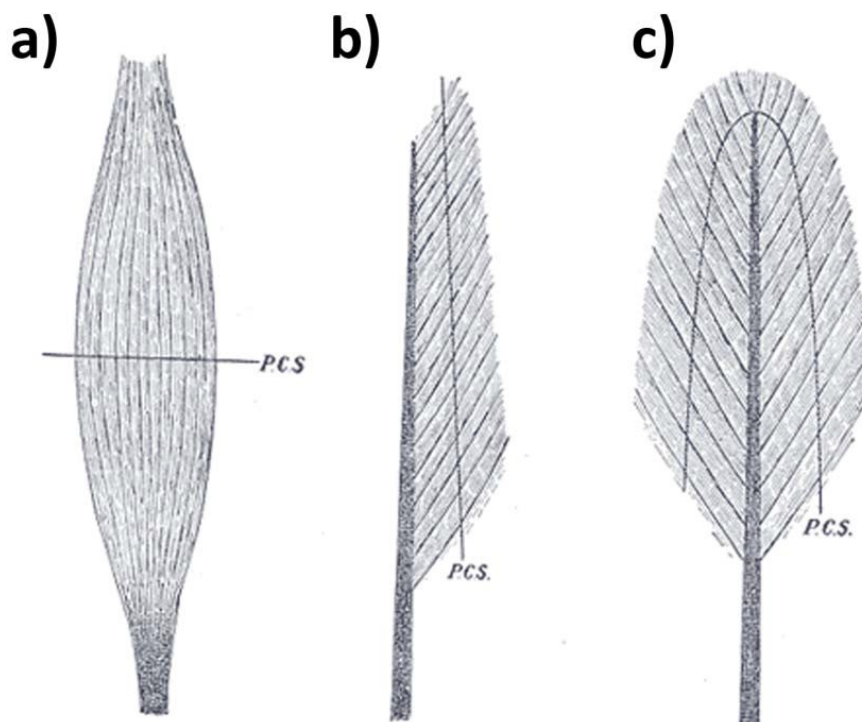


Figure 1.2: The three types of muscle-tendon arrangement, a) the parallel-fibered muscle, b) the unipennate muscle and c) the bipennate muscle. P.C.S. marks the physiological cross-section that cuts all the fiber. Reprint from *Gray's Anatomy* (Gray et al., 1924).

These types of fiber differ in their morphology, their contractile and biochemical properties and play an important role on the developed force. Their distribution in the muscles varies from one muscle to another. Histology with coloring techniques (Brooke and Kaiser, 1970; Brooke MH and Kaiser KK, 1970; Choi and Kim, 2009) have distinguished three types of muscle fibers, divided into two major groups (figure 1.3), slow fibers (**I**) and fast fibers (**II**) (Pette and Vrbová, 1985) (Plaghki, 1985). They have each their own specificities.

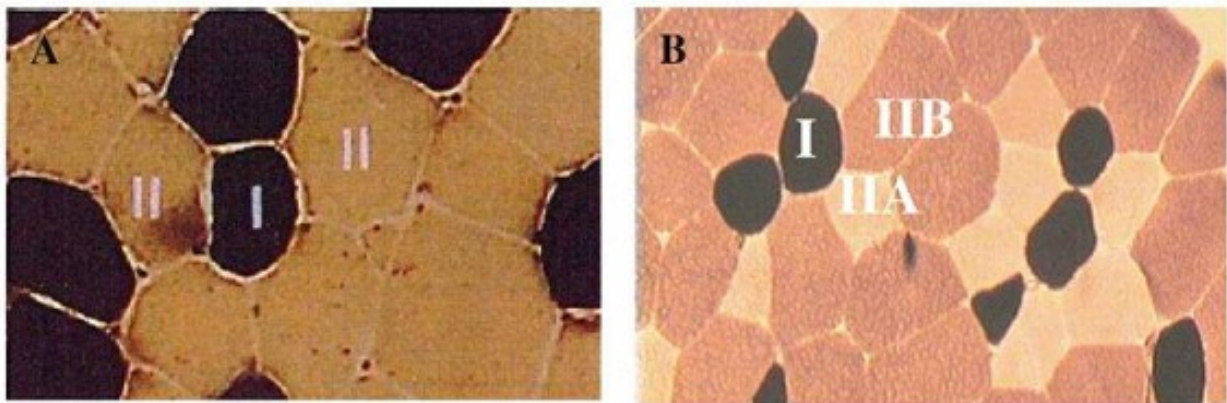


Figure 1.3: Identification of slow and fast fibers, according to Kim and Choi, 2009

- **Slow fibers (type I)** : They have a high level of oxidative enzymes, low glycogen level and a high density of mitochondria. They contract slowly and have high resistance to fatigue. They are rich in myoglobin and blood capillaries that causes their red color. They are found in the muscles having a postural function.
- **Fast fibers (type II)** : On the contrary they are subdivided into two types of fibres, IIA (red) and IIB (white) which are able to contract quickly and have a lower resistance to fatigue.

Slow fibers are always solicited the first whereas the fast fibers are only solicited during important efforts and short periods.

The skeletal muscle architecture is the structural property of the whole muscles that dominates their function. The skeletal muscles are usually fixed on the bone at each of their ends via a tendon and there are several levels of organization in a skeletal muscle as shown in Figure 1.4 (Marieb and Hoehn, 2014).

The skeletal muscle is composed a large number of smaller bundles of muscle fascicles, which are separated by connective tissue such as epimysium, perimysium, endomysium and

sarcolemma. The muscle fascicle is composed of many skeletal muscle cells, it is known as muscle fiber, which has a cylindrical shaped cell measuring from 10 to 100 micrometers as diameter and until 75 cm as length (Sherwood, 2015). Each muscle fiber is protected by a cell membrane called the sarcolemma. The muscle fiber is composed of a set of myofibrils.

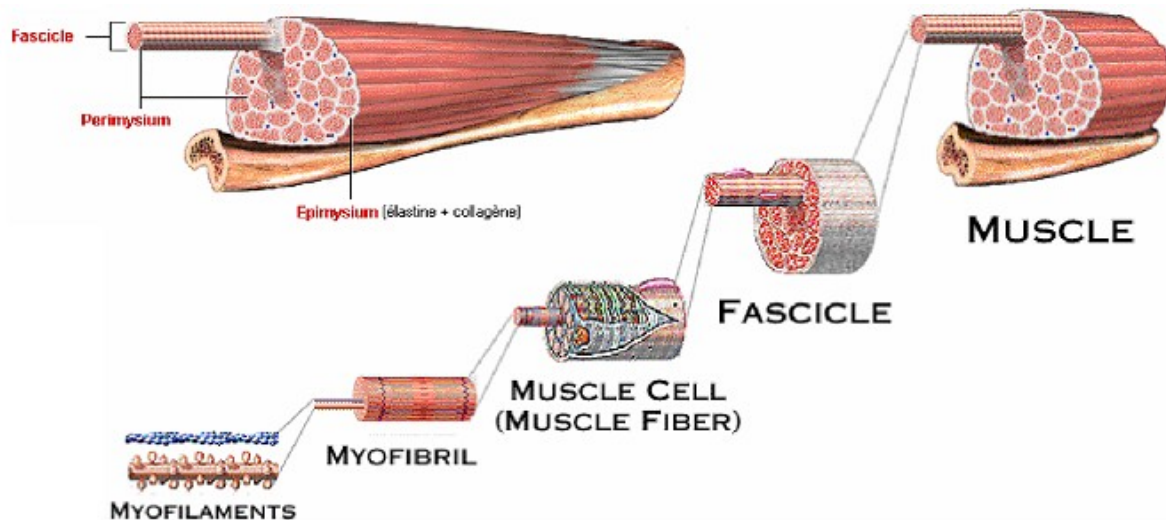


Figure 1.4: multi scale organization of the muscle system

Myofibrils have specific contractile intracellular elements that are composed of a succession of sarcomeres in series. The sarcomere is the smallest contractile intracellular element and consists of thin (actin) and thick (myosin) myofilaments that, through their interactions, can perform a shift that induce tension production in muscle, through interconnectivity and movement with each other (Huxley and Simmons, 1971) (Huxley and Taylor, 1958). Several proteins are presented in the muscle cell. Indeed, besides actin and myosin which are contractile proteins, it contains regulatory proteins such as troponin and tropomyosin or structural like titin, nebulin and alpha-actinin of the muscle system.

4.2 The functional unit of muscle

The principal function of skeletal muscle is to produce movement of the body set or body parts and perform work through coordinated and voluntary muscle contraction such as lifting weights or walking. Moreover, skeletal muscles are important for maintaining the position of the body and give it its shape. It also generates heat as a by-product of muscle activity, which assists in maintaining normal body temperature.

The fibers are surrounded by endomysium and include a set of myofibrils surrounded by a membrane called the sarcolemma. Typically there are hundreds of these membranes in one cross section of a muscle fiber. It is divided into segments called sarcomeres.

Sarcomeres are composed of thick filaments (composed of a protein, myosin, whose diameter is 12 to 18 nm) and thin filaments (compound of another contractile protein, actin, which has a diameter of 5 to 8 nm). They are surrounded by two dark colored bands (characterizing anisotropic zones, highly birefringent) called Z-discs or Z-lines. These Z-discs are dense protein discs that do not allow easily the passage of light and thus appear black under the microscope.

The area between the Z-discs is fourthly divided into two lighter colored bands of actin at either end called the I-bands (characterize isotropic zones) and a darker, grayish band of myosin in the middle called the A-band .

During muscle contraction, each muscle sarcomere shortens as the thin filaments slide closer to each other between the thick filaments so that the Z lines are pulled closer (Figure 1.5).

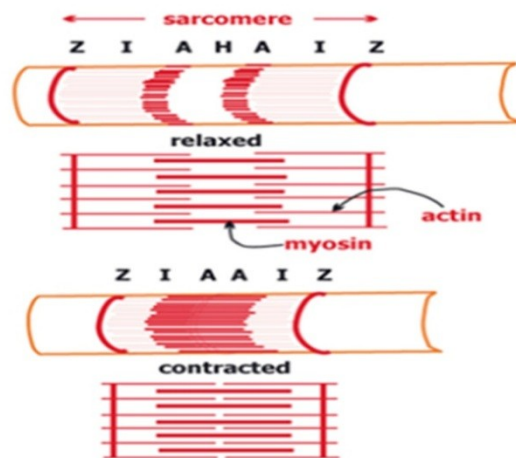


Figure 1.5: Sarcomere structure

4.3 The thigh muscles

4.3.1 Composition of the thigh muscles

The thigh is composed of ten muscles located in the anterior, medial and posterior area.

- **The anterior thigh muscles:** The muscles of the anterior part of the thigh include the quadriceps group and Sartorius. The quadriceps muscle is a group of four muscles that originate in different locations and that form the front of the thigh. Rectus femoris forms the middle portion of the quadriceps, vastus lateralis is the lateral-most of the

quadriceps, vastus medialis is the most medial of the quadriceps and vastus intermedius lies behind the rectus femoris. The main action of this muscle group is the extension and the stabilization of the leg.

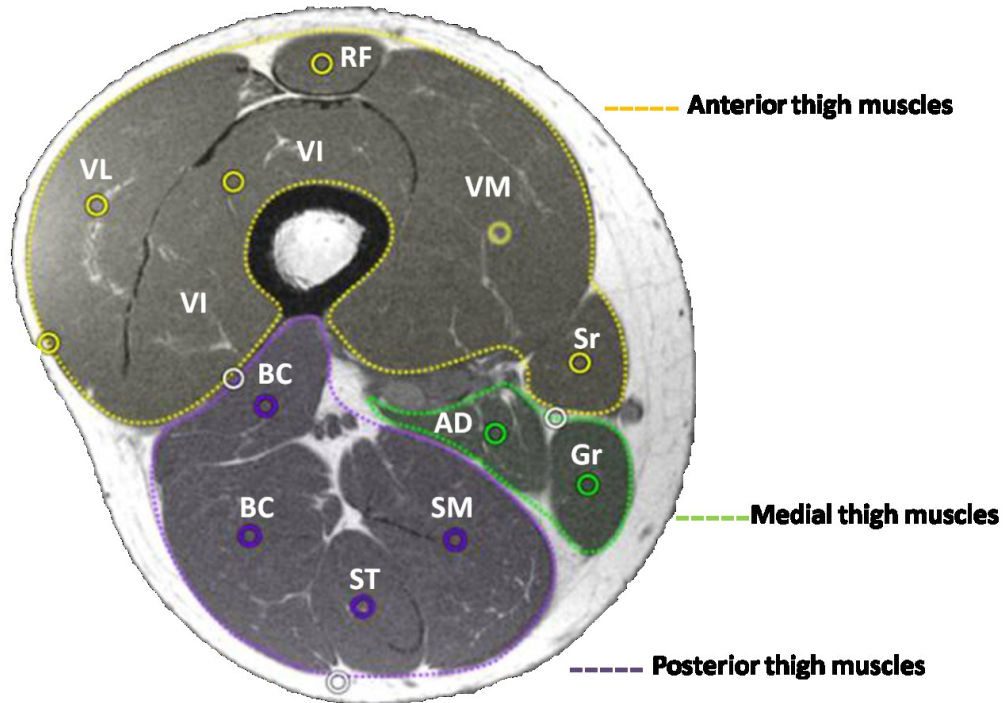


Figure 1.6: Axial image with the investigated thigh muscles. Quadriceps muscle (VL: vastus lateralis, VI: vastus intermedius, VM: vastus medialis, RF: rectus femoris), Sr: sartorius, Gr: gracilis, AD: adductor, hamstring muscles (ST: semitendinosus, SM: semimembranosus, BC: long and short biceps)

- **The medial thigh muscles:** The muscles of the medial part of the thigh have the adductor and gracilis muscles that bring the thigh toward the midline and that rotate it.
- **The posterior thigh muscles:** The posterior thigh is known as the hamstring muscles. They are composed of three muscles, semimembranosus, semitendinosus and biceps, that form the back of thigh. Theirs roles are to flex the leg.

4.3.2 Determination of the morphological properties with imaging techniques

The ultrasonic imaging (US), is one of medical imaging technique that is widely used in clinical studies, has been used to make an evaluation of muscle geometric parameters. In the muscle, the muscle fibers are arranged in different orientations compared to aponeurosis. The angle formed between these muscle fibers, which connect the tendon and aponeurosis, is

called the pennation angle (figure 1.7). Ultrasound is simplest method to visualize the orientation of the muscle fascicles. Moreover, any authors use this technique to evaluate the muscle thickness, the pennation angle (θ) (figure 1.7) , and the fascicle length (Abe et al., 1998, 2000; Arampatzis et al., 2007; Brechue and Abe, 2014; Chow et al., 2000; Fukunaga et al., 1992, 1997a, 1997b; Hodges et al., 2003; Ichinose et al., 1997; Reeves and Narici, 2003).

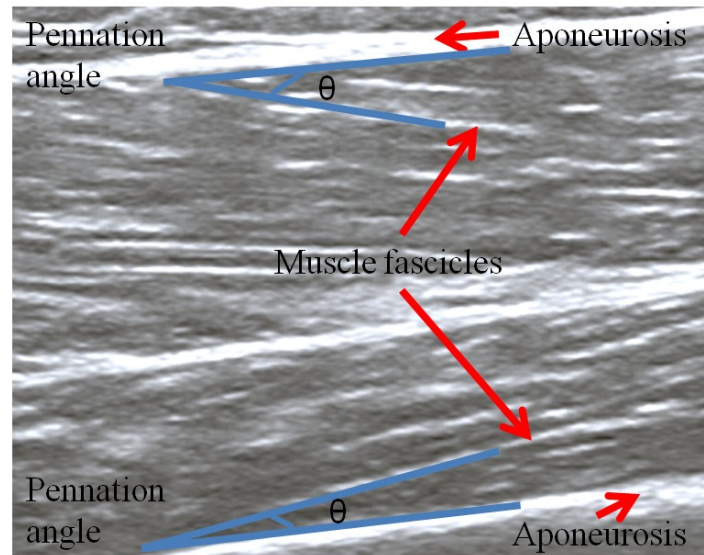


Figure 1.7: Schematic representation of muscle architecture.

These studies are valuable because they have defined a new typology of the human body muscles according to the arrangement of the muscle fibers.

Several studies use the ultrasound imagery technique to determine the structural parameters of muscle such as: the muscular thickness (Kubo et al., 2003), the thickness of the subcutaneous adipose tissue (Heckmatt et al., 1988a; Saito et al., 2003; Scholten et al., 2003), the pennation angle (Debernard et al., 2011a; Fukunaga et al., 1997a; Henriksson-Larsen et al., 1992; Hodges et al., 2003; Kawakami et al., 1993; Kubo et al., 2003; Maurits et al., 2004), the length of fascicule (Kubo et al., 2003), and the muscle area (*Cross-Sectional Area (CSA)*) (Maurits et al., 2004; Walton et al., 1997).

These studies were capable of determining the healthy muscle architecture (Heckmatt et al., 1988a; Maurits et al., 2004; Scholten et al., 2003) in order to study the effects of hypertrophy (Kawakami et al., 1993), the age, the sex (Kubo et al., 2003; Men et al., 1985; Young et al., 1984) and neuromuscular diseases (Heckmatt et al., 1988b; Maurits et al., 2004; Scholten et al., 2003) on the eventual modification of the muscular architecture.

These parameters along with the muscular area (Beneke et al., 1991) and the muscular volume (Walton et al., 1997) can be defined with magnetic resonance imaging (MRI) to

decrease the acquisition protocol, the methods and cutting numbers by optimizing the acquisition time for these purposes (Fukunaga et al., 2001; Lund et al., 2002; Morse et al., 2007; Nordez et al., 2009; Tracy et al., 2003). However MRI has certain limitation of visualization and characterization of the depth of the muscular architecture compared to the ultrasonic imaging technique (US).

4.3.3 Aponeurosis

A white or yellowish membrane is glossy, very resistant and is made of intersecting fibers, either termination or intersection muscles that attach the bone or muscle envelope to hold it in place. It constitutes a very thin envelope that surrounds and connects the various organs of our body. This tissue is found deep in the muscles, bones, nerves, heart, lung, cortex, ligaments and internal organs. Around the muscles and muscle bundles, the aponeurotic bulkheads form groups called lodges that allow easily to differentiate each muscle (Figure 1.7)

B. Mechanical properties of the muscle

1. Functional characteristics of skeletal Muscle Tissue

The Muscle is the only body tissue with the properties of **irritability, contractility, extensibility and elasticity.**

The **irritability** property of a muscle is the ability to respond to a stimulus, that produces a muscle contraction. Stimulus can be internal or external. The **Contractility** refers to the ability to shorten or contract causing an increase in the tension between its ends and length that may shorten, or remain the same. The **extensibility** means the ability to stretch in response to a force and the **elasticity** is the ability to recoil when a stretch force is removed to returns the muscle to its resting length.

The characterization of the skeletal muscles properties are carried out by complex mechanical behaviours such as anisotropy, quasi-incompressibility, non-linear elasticity and viscoelasticity with time dependent creep and stress relaxation, rate dependence and hysteresis in addition to the ability to undergo large deformation (Fung and Cowin, 1994).

2. The Hill model

For further explanation and to identify the behavior of the muscle in its active and passive states, simple models have been proposed with the combination of springs and

dashpots elements. The first model, that represents muscle response, is a simple spring. It characterizes the effect of the muscle length as a function of the developed force. To study the influence of the speed of contraction, a viscous element is added in parallel by Hill (Hill, 1922). In 1927, Levin and Wyman complicated the Hill model by adding an elastic component in series to take into account the influence of the tendon on the myo-tendon complex (Levin and Wyman, 1927). This model was modified by Hill in 1938 and revisited by Shorten in 1987. It is a three-component model; where each component reflects a property of the muscle behavior (Goubel and Lenseil-Corbeil, 2003):

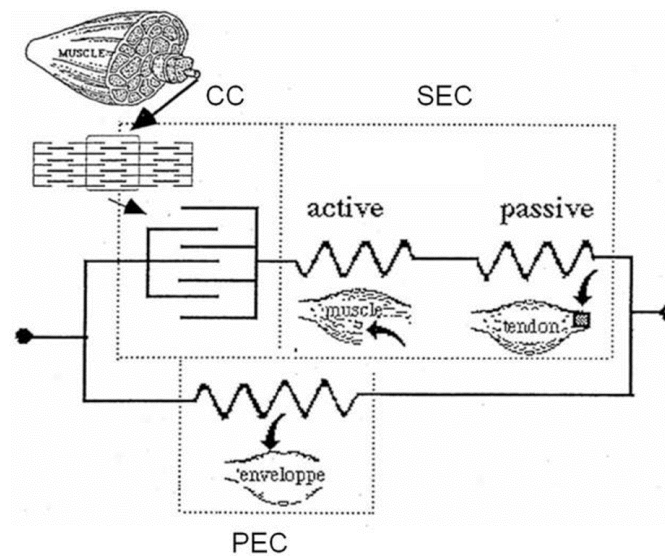


Figure 1.8: Mechanical model of muscle Shorten-Hill (1987); CC: Contractile component, PEC: Parallel elastic component, SEC: Series elastic component

- Contractile component (CC) (muscle fiber) is similar to a shock absorber and has their shortening velocity related to the force developed by the muscle.
- Parallel elastic component (PEC) (muscle membrane or fascia) represents the muscle behavior when reaching important extensions.
- Series elastic component (SEC) (tendon) explains the significant and rapid decrease of efforts when the muscle is contracted at a constant length (isometric conditions) and subjected to a rapid shortening. It also intervenes in enhancing the muscle performance by storing mechanical potential energy developed by the muscle.

Specific tests performed on in vitro muscle and then extended to in vivo tests allow the studying of each of these components: Contractile component (CC), Elastic component parallel (ECP) and Elastic component series (ECS).

The elastic component series and the contractile component allow the modeling of the specific behavior within the myofibril, the muscle contraction. The parallel elastic components allow the reproduction of the elastic compartment of the conjunctive tissue that includes the muscle membranes: endomysium, perimysium and epimysium.

The continuum mechanics is the field of physics interested in the deformation of the solid and the fluid flow and that describes all mechanical changes of an environment: static compression or extension and the mechanical wave propagation of all kinds. To discuss continuous mechanics, several hypotheses must be respected: a continuous medium, homogeneity and isotropy. Mechanical waves are the carriers of information in the continuum mechanics that allow us to identify the mechanical properties of tissues. These waves will be propagate through tissue with parameters dependant on its properties.

The theory of the continuous medium mechanics is based on the law made by Hooke (Chapman, 2004). This law allows to connect the force exerted on a solid to its deformation. It also describes all the mechanical modification of the object on the environment: static compression or extension and the propagation of the mechanical waves of all kinds. Subsequently, it is possible to introduce parameters that can describe the continuous media.

3. Hooke's law

Muscle tissues are non-linear, viscoelastic, anisotropic and incompressible. However, to simplify the analysis, the mechanical properties are usually modeled to behave the muscle as linear, elastic and isotropic materials (Bensamoun et al., 2006a; Krouskop et al., 1998; Ophir et al., 1999). The elasticity is the quality of a material to be deformable while resuming its original shape when the applied stress disappears. The conventional theory of elasticity describes the mechanical properties of elastic solids where stress is proportional to strain in small deformations. Thus, the elasticity of a muscle means that the muscle can return to its original length and form after a contraction or a stretch.

Robert Hooke created a law named hook's law proving that strength is always proportional to the elongation. Originally developed to describe the behavior of the springs, this law is then applied by physicists in soft solid element in the case of small deformations. When a deformation (strain) is applied to the solid, volume internal forces to the object will be created in order to reduce the solid to its equilibrium state. These volume internal forces are called constraints (stress).

Hooke's law allows to connect a stress (σ) (force) to a strain (ε) (local elongation) and elasticity (E):

$$\sigma = E \cdot \varepsilon$$

4. Stress and strain Tensors

They allow to extend the concepts of strain and stress to a case of an elementary volume of three dimension according to the tensor formalism. They are defined as follows (Figure 1.9):

The stress tensor σ_{ij} corresponds to the i^{th} component of the stress applied to the facet normal \vec{n}_i (vector).

The strain tensors ε_{ij} are defined as $\varepsilon_{ij} = \frac{1}{2} \left(\frac{\partial u_i}{\partial x_j} + \frac{\partial u_j}{\partial x_i} \right)$, where u is the field displacement.

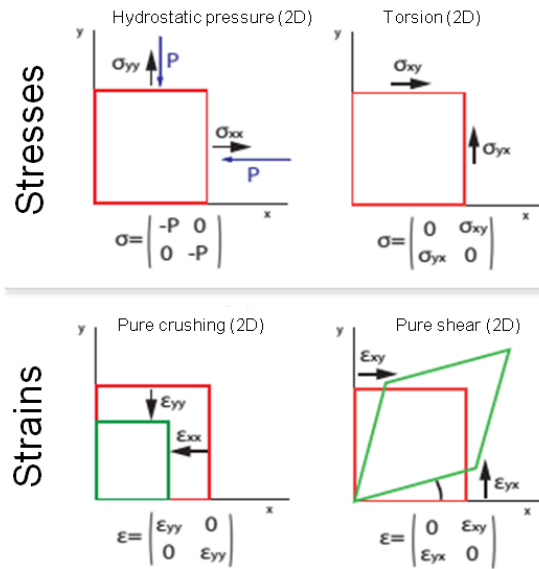


Figure 1.9: Different simplest cases of stresses and strains and their associated tensors (illustrated in 2D) .

5. Tensor of elasticity in isotropic medium

Hooke's law can be extended to a three-dimensional problem when considering an elementary volume, in the approximation of small strains that links the stress tensor (σ) to the strain tensor (ε) with an elastic tensor. In fully anisotropic homogeneous material, the stress-strain relationship can be described by Hooke's law:

$$\sigma_i = C_{ij} \cdot \varepsilon_j$$

where σ_i is the stress matrix and ε_j the strain matrix and C_{ij} is a fourth order tensor that linearly relates ε and σ .

C_{ij} is sometimes named the elastic rigidity tensor and contains 81 elements that completely describe the elastic characteristics of the medium. Because of the symmetry of σ and ε , only 36 elements of C_{ij} are independent in general cases. The stiffness tensor C_{ij} consists of 21 independent variables due to symmetry considerations (i.e. $C_{ij} = C_{ji}$).

$$\{C_{ij}\} = \begin{bmatrix} C_{11} & C_{12} & C_{13} & C_{14} & C_{15} & C_{16} \\ C_{12} & C_{22} & C_{23} & C_{24} & C_{25} & C_{26} \\ C_{13} & C_{23} & C_{33} & C_{34} & C_{35} & C_{36} \\ C_{14} & C_{24} & C_{34} & C_{44} & C_{45} & C_{64} \\ C_{15} & C_{25} & C_{35} & C_{45} & C_{55} & C_{65} \\ C_{16} & C_{26} & C_{36} & C_{46} & C_{56} & C_{66} \end{bmatrix}$$

By exploiting the symmetries of the medium, the tensors of stresses (ε_j) and the strains (σ_i) can be reduced to tensors each having only 6 items. Moreover, only 2 independent constants of rigidity are present in C_{ij} for linear homogeneous isotropic purely elastic medium: Lamé coefficients λ and μ have a stress dimension; λ is related to longitudinal strain and μ to shear strain. However, the transversely isotropic material contains only six independent parameters due to the axis of symmetry.

$$\{C_{ij}\} = \begin{bmatrix} C_{11} & C_{12} & C_{13} & 0 & 0 & 0 \\ C_{12} & C_{11} & C_{13} & 0 & 0 & 0 \\ C_{13} & C_{13} & C_{33} & 0 & 0 & 0 \\ 0 & 0 & 0 & C_{44} & 0 & 0 \\ 0 & 0 & 0 & 0 & C_{44} & 0 \\ 0 & 0 & 0 & 0 & 0 & C_{66} \end{bmatrix}$$

Lamé coefficients are defined from C_{ij} as follows:

$$C_{11} = C_{22} = C_{33} = \lambda + 2\mu$$

$$C_{12} = C_{13} = C_{23} = \lambda$$

$$C_{44} = C_{55} = C_{66} = (C_{11} - C_{12})/2 = \mu$$

The strain–stress relationship can be written as:

$$\begin{pmatrix} \sigma_{11} \\ \sigma_{22} \\ \sigma_{33} \\ \sigma_{23} \\ \sigma_{13} \\ \sigma_{12} \end{pmatrix} = \begin{pmatrix} \lambda + 2\mu & \lambda & \lambda & & & \\ \lambda & \lambda + 2\mu & \lambda & & & \\ \lambda & \lambda & \lambda + 2\mu & & & \\ & & & \mu & 0 & 0 \\ & & & 0 & \mu & 0 \\ & & & 0 & 0 & \mu \end{pmatrix} \cdot \begin{pmatrix} \varepsilon_{11} \\ \varepsilon_{22} \\ \varepsilon_{33} \\ 2\varepsilon_{23} \\ 2\varepsilon_{13} \\ 2\varepsilon_{12} \end{pmatrix}$$

Employing the lame coefficient, it is possible to define a couple of equivalent parameters (Storaa et al., 2003) whose physical signification differs slightly. This allows to choose the most suitable couple (torque) to the problem:

$$K = \lambda + 2/3\mu$$

where K is the compression module (bulk modulus) and μ is the shear modulus.

The coefficient K is then called the compression module since it connects the compression strain to the strain. This compression module characterizes the change in volume of the solid when stress is applied simultaneously on all sides and perpendicular to all the points of the surface which surround the solid (principle of hydrostatic pressure).

The second coefficient lame μ corresponds to the shear modulus which connects the shear strains to stresses. This shear modulus reflects the difficulty to twist (shear) the solid. Although this coefficient is small in soft biological tissues, it is not negligible. This module changes a lot with tissue pathology, which makes it interesting medically to characterize this parameter. In the literature, the shear modulus (μ) is defined as "shear modulus" when it is independent of the frequency and as "shear stiffness" at a given frequency (Bensamoun et al., 2007; Debernard et al., 2011b; Dresner et al., 2001).

However, it is possible to study the mechanical properties of a solid following a different approach. Under homogeneous deformations, such as hydrostatic pressure, the stress tensor is constant throughout the solid.

Young's modulus (E) and Poisson's ratio (ν) are two parameters that characterize the solid. They are defined as:

$$\nu = \lambda/2(\lambda+\mu) \text{ and } E = \mu (3\lambda+2\mu)/ (\lambda+ \mu)$$

Poisson's ratio (ν) defines the relationship between uniaxial crushing and resulting lateral elongation and is 0.5 for incompressible solids. Young's modulus (E) is the potential crush, always uniaxially, a solid having the ability to deform laterally. Since the stresses are applied uniaxially (in a single direction), other parameters are free to deform. It is possible to express the two lame coefficients (λ) depending on the Young's modulus E and Poisson's ratio ν :

$$\lambda = \frac{E\nu}{(1-2\nu).(1+\nu)} \quad \text{and} \quad \mu = \frac{E}{2(1+\nu)}$$

The table below lists the conversions between Lamé coefficients, Young’s modulus, Poisson’s ratio, and C_{ij} for an isotropic elastic homogeneous medium.

	E, ν	μ, λ	C_{11}, C_{12}, C_{44}
E	E	$\frac{\mu(3\lambda + 2\mu)}{\lambda + \mu}$	$C_{11} - 2\frac{C_{12}^2}{C_{11} + C_{12}}$
ν	ν	$\frac{\lambda}{2(\lambda + \mu)}$	$\frac{C_{12}}{C_{11} + C_{12}}$
λ	$\frac{E\nu}{(1 - 2\nu)(1 + \nu)}$	λ	C_{12}
μ	$\frac{E}{2(1 + \nu)}$	μ	C_{44}
C_{11}	$\frac{E(1 - \nu)}{(1 - 2\nu)(1 + \nu)}$	$\lambda + 2\mu$	C_{11}
C_{12}	$\frac{E\nu}{(1 - 2\nu)(1 + \nu)}$	λ	C_{12}
C_{44}	$\frac{E}{2(1 + \nu)}$	μ	C_{44}

Table 1-1: List of conversions between Lamé coefficients, Young’s modulus, Poisson’s ratio, and C_{ij} for an isotropic elastic homogeneous medium

6. Incompressible property

Muscle is an incompressible material. The volume of the muscle remains constant for any given transformation during compression (Figure 1.10). Due to the conservation of the volume, strain in a certain direction has to be compensated by an inverse strain in other directions. The sum of the strain in all directions must be null (Støylen, 2001) under the hypothesis of no shear strain. An incompressible material is also called an isochoric material.

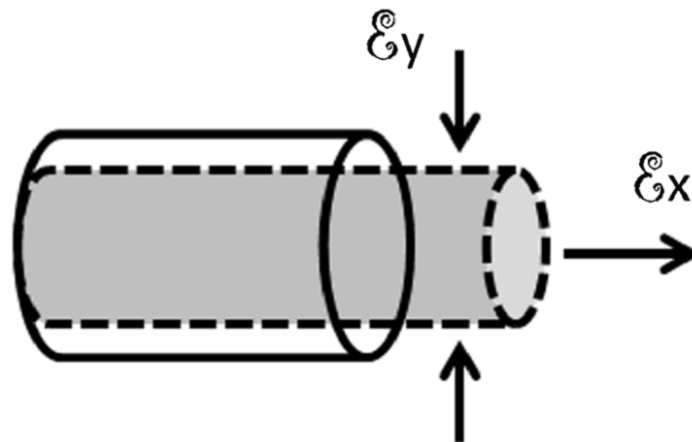


Figure 1.10: The principle of incompressibility. The volume of the incompressible object remains constant during (Lindberg, 2013).

This mechanical property is due to the important quantity of water in the muscle. It is usually used as a Poisson coefficient modeling. Poisson's ratio (ν) is a material constant that can be used to characterize the deformation in such material. This constant describes the relation between the transversal and the axial strain and varies between -1 and 0.5. Even though there are very little quantitative data on the Poisson's ratio of soft biological tissues, researches in animal, human and phantom studies have shown that the Poisson's ratio of soft tissues and muscle is close to 0.5 (Fung and Cowin, 1994; Krouskop et al., 1998; Ophir et al., 1999; Støylen, 2001).

The finite element models (Blemker et al., 2005; JOHANSSON et al., 2000; Leclerc et al., 2013a; Martins et al., 1998; Oomens et al., 2003; Yucesoy et al., 2002) use incompressible or nearly incompressible materials to represent the passive muscle behavior.

Muscle tissues are composed mainly of water and are nearly incompressible, the compression module K is very large compared to the shear modulus μ . The compression modulus K of these tissues is of an order of several GPa contrary to shear modulus μ which is of an order of some tens of kPa.

For medical applications, Poisson's ratio is close to 0.5, $K \gg \mu$ and $K \approx \lambda$. Therefore, the Young's modulus E can be simplified to:

$$E = 3\mu$$

7. Propagation of waves in a soft material

The study of the shear wave propagation in the soft tissue is a very important issue to determine the mechanical properties. The elastography technique, which determines the mechanical properties, is based on this wave propagation which will be described subsequently.

In the case of an elastic solid and supposing that the deformations are low, it is possible to express the equation of motion in function of the mechanical properties of the solid and the displacement (u):

$$\rho \frac{\partial^2 u}{\partial t^2} = \frac{E}{2(1+\nu)(1-2\nu)} \text{grad}(\nabla \cdot u) + \frac{E}{2(1+\nu)} \Delta u$$

where ρ is the density, t is the time, E is the Young's modulus and ν is the Poisson's ratio.

In the case of a plane elastic wave traveling along the x direction, the equation of motion becomes:

$$\begin{cases} \frac{\partial^2 u_x}{\partial x^2} - \frac{1}{V_l} \frac{\partial^2 u_x}{\partial t^2} = 0 \\ \frac{\partial^2 u_y}{\partial x^2} - \frac{1}{V_t} \frac{\partial^2 u_y}{\partial t^2} = 0 \end{cases}$$

where V_l is the velocity of the longitudinal waves (or compression waves, seismic waves P) and V_t is the velocity of the transversal waves (or shear waves, seismic waves S) (Figure 1.11).

These velocities (V_l and V_t) can be expressed in function of the Young's modulus (E) and Poisson's ratio (ν):

$$\begin{cases} V_l = \sqrt{\frac{E(1-\nu)}{\rho(1+\nu)(1-2\nu)}} = \sqrt{\frac{\lambda+2\mu}{\rho}} \approx \sqrt{\frac{K}{\rho}} \\ V_t = \sqrt{\frac{E}{2\rho(1+\nu)}} = \sqrt{\frac{\mu}{\rho}} \approx \sqrt{\frac{E}{3\rho}} \end{cases}$$

As a function of the direction of propagation of the wave, two types of waves can be distinguished:

1. The compression waves (longitudinal) V_L , where the wave propagation direction is parallel to the displacement (Figure 1.11a).
2. The shear waves (transversal) V_T , where the wave propagation direction is perpendicular to the displacement (Figure 1.11b).

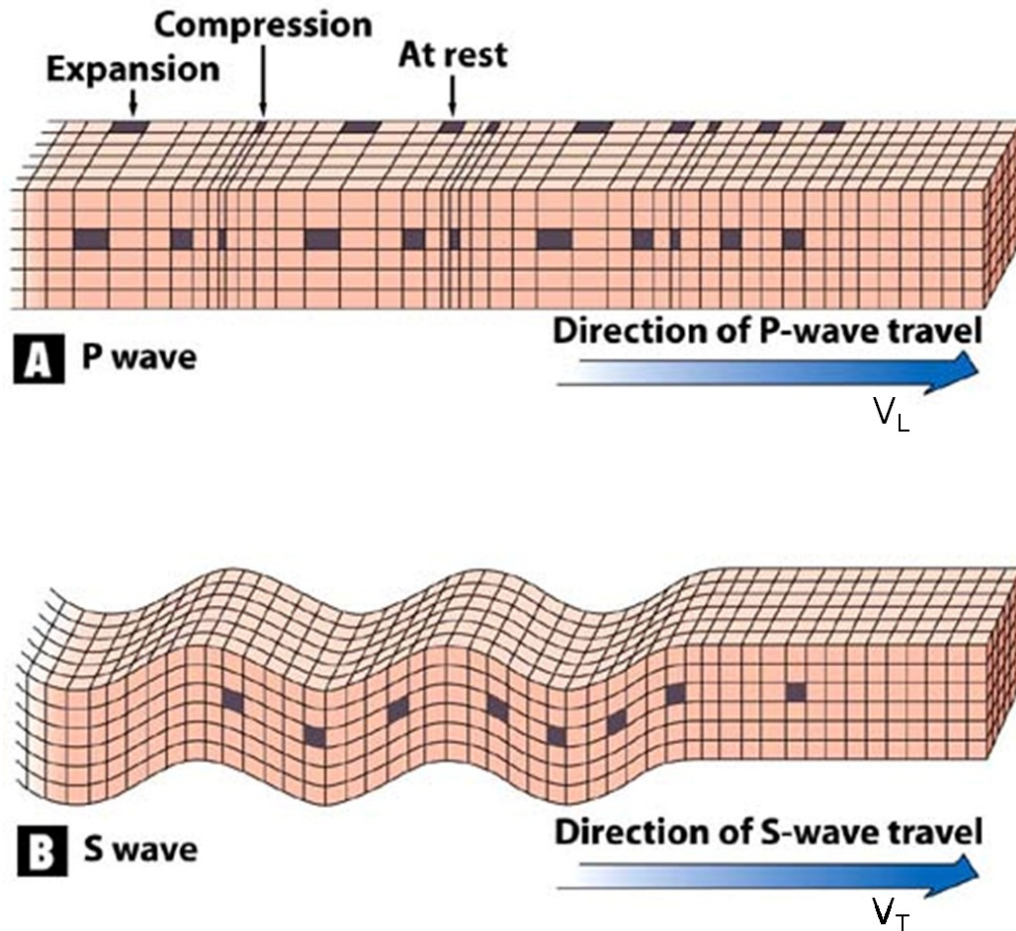


Figure 1.11: Representation of the compression (A) waves and the shear (B) waves.

The expressions of longitudinal and transversal velocities in function of the compression and shear moduli show that the propagation of longitudinal waves is governed by the compression module while the propagation of transverse waves is governed by the shear modulus, which is connected to the Young's modulus.

In homogeneous isotropic elastic medium, it is possible to split the acoustic waves in independent longitudinal and transverse waves, each travelling at a speed V_L and V_T respectively.

For quasi incompressible and soft biological tissues, the compression wave propagation velocities are 1500 m/s, similar to water, and the shear wave propagation velocities are between 1 m/s and 20 m/s. Thus, shear wave could be measured and the soft tissues have different shear moduli (Robert, 2009) (Figure 1.12).

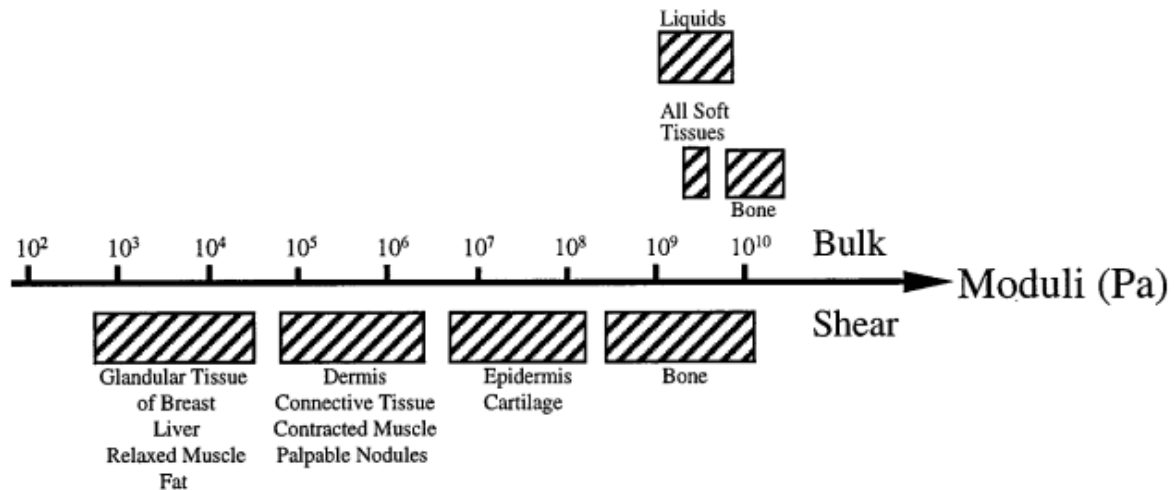


Figure 1.12: Variation of the mechanical compression and shear modulus of various biological tissues. Ranges associated with each modulus for a given tissue type are indicated by the shaded regions (Sarvazyan et al., 1998).

8. Viscoelastic compartment

The word viscoelastic is composed of the words "viscous" and "elastic"; thus a viscoelastic material exhibits both viscous (fluid) and elastic (solid) behaviors, such as the muscle tissue.

Skeletal muscle tissue, like many other biological tissues, is a viscous material. The viscosity has a direct effect on the mechanical properties of the passive muscle. Best et al., (1994) realized a test of traction on rabbit muscle at strain rate between 0.01s^{-1} and 2s^{-1} and showed that the response of the stress is dependent on the strain rate. Similarly Myers et al (1995, 1998) conduct the same type of experiment but with higher strain rate: 1s^{-1} , 10s^{-1} and 25s^{-1} . For the same strain at 20%, they get a Young's modulus of 1.75 MPa for 1s^{-1} , and 2.79 MPa for 25s^{-1} , showing a significant increase in the stiffness as a function of the strain rate.

8.1 Elastic properties

The strain–stress relationship $\sigma_i = C_{ij} \cdot \varepsilon_j$ is valid when the strain is instantaneously provoked by stress, i.e., no dephasing process occurs. The equations of the compression and the shear waves can be reformulated according to the two longitudinally (u_l) and transversely (u_t) displacements of the wave:

$$\begin{cases} \frac{\partial^2 u_l}{\partial x^2} = K \frac{\partial^2 u_l}{\partial t^2} \\ \frac{\partial^2 u_t}{\partial x^2} = \mu \frac{\partial^2 u_t}{\partial t^2} \end{cases}$$

These equations assume that the waves, that propagate in the medium, remain unchanged and can propagate to infinity if the considered solid doesn't exceeded by limit. However shear waves attenuate rapidly during their propagation in biological tissue. In order to take this attenuation in the wave equation, it is necessary to consider that the shear modulus is not a real number but a complex number. It is possible to approach the problem solely in terms of shear considering only the complex shear modulus (G^*) and Hooke's law where the wave equation becomes:

$$\begin{aligned} \sigma &= G^* \cdot \varepsilon \\ \rho \cdot \frac{\partial^2 u}{\partial t^2} &= G^* \cdot \Delta u \end{aligned}$$

The behavior of the material is then mainly described by the expression of the complex shear modulus. The complex shear modulus can simplify the notations and its expression allows modeling of behavior solids. The different behavior modes correspond to the rheological models whose complexity varies according to the desired use.

8.2 Viscous properties

The behavior of viscoelastic materials under uniaxial loading may be represented by means of conceptual models composed of elastic and viscous elements, which provide physical view point and have didactic value. One can build up a model of linear viscoelasticity by considering the combinations of the linear elastic spring and the linear viscous dash-pot. These are known as rheological models or mechanical models.

The complex shear modulus (G^*) and its mechanical behavior is characterized with different rheological models whose complexity varies according to the desired usage. The study of the characteristics of deformable bodies (elasticity, viscosity, plasticity, fluidity) is better known as the rheology study. Indeed the objective of the rheology is to study the fluid flow and the viscoelastical properties of the deformable solid. The two basic components used in rheology are the spring and the dash-pot.

The rheological models can be characterized with respect to their static and dynamic behavior.

The static characterization is obtained through two types of experiments: creep and relaxation:

- Creep consists in applying a constant stress to the system and observes its time deformation.
- Relaxation consists in eliminating comes to release the system stress and observe its behavior at the equilibrium.

The dynamic characterization consists in expressing the shear modulus in function of to the characteristics of the rheological model in consideration and characterizes the mechanical behavior in function of on the applied frequency.

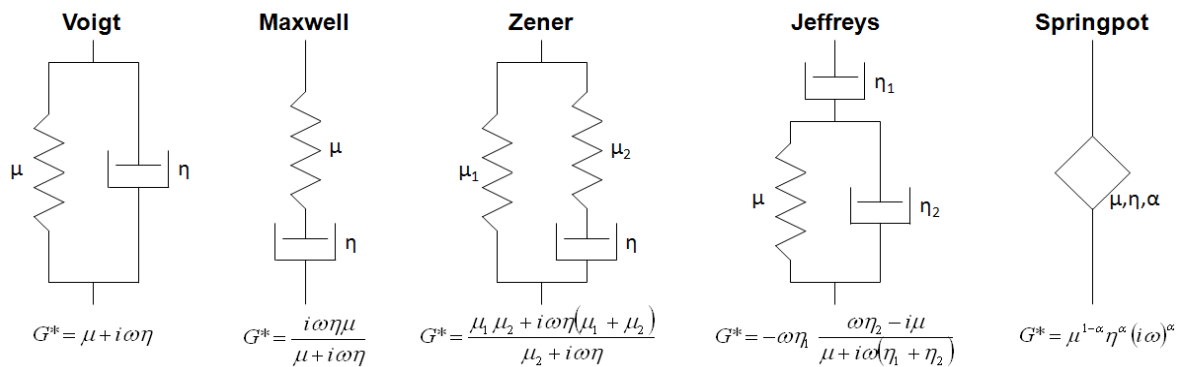


Figure 1.13: Rheological models used in the literature for the characterization of biological tissues. G^* is the complex shear modulus, μ is shear modulus, η is viscosity, f is the frequency and ω is the pulsation ($2.\pi.f$)

The Maxwell model can be represented by a purely viscous dash-pot and a purely elastic spring connected in series. This model is particularly adapted for modeling liquid deformations.

Jeffrey model contains one spring and two dampers and is used normally in fluids,

The Kelvin–Voigt model also called the Voigt model, is a viscoelastic material that has both the elasticity (μ) and the viscosity (η) properties and can be represented by a purely viscous dash-pot and purely elastic spring connected in parallel. The behavior of these objects, described by a Voigt model, is closer to the behavior of a solid rather than that of a liquid.

The **Zener model** also known as the **standard linear solid (SLS) model** is a method that models the behavior of a viscoelastic material using a linear combination of springs and dash-pot to represent elastic and viscous components respectively. This model consists of two elasticity coefficients μ_1 and μ_2 . Often, the more similar Maxwell model and the Kelvin–Voigt model are used. These models are often proven insufficient since the Maxwell model does not describe creep or recovery and the Kelvin–Voigt model does not describe stress relaxation. SLS is the simplest model that predicts both phenomena.

The springpot model is condensed between the spring and dash-pot. The viscoelastic behavior of biological tissues cannot be modeled perfectly with different models previously introduced. The springpot (μ, η, α) model take three parameters into account. The parameter α represented a weighting factor between a purely elastic behavior ($\alpha = 0$) and a purely viscous behavior ($\alpha = 1$). For the springpot model, (μ) and (η) were linearly dependent, meaning that either the value of (μ) or (η) were fixed.

C. Techniques used for the characterization of the mechanical properties.

In this part, the experimental techniques are performed *in vitro* and *in vivo* in order to determine the mechanical properties of soft biological tissues.

1. *In vitro* methods

1.1 Compression tests

In a compression test, the sample is maintained between two plates (steel) while the normal force (F) is measured as a function compression (h), performed at an imposed speed after preloading (Figures 1.14). Then from the slope of the force-displacement curve, the Young's modulus can be calculated as

$$E = \frac{\sigma}{\varepsilon} = \frac{\frac{\Delta F}{A_0}}{\frac{\Delta h}{h_0}} = \frac{h_0}{A_0} \cdot \frac{\Delta F}{\Delta h}$$

where σ is the uniaxial compressive stress, ε is the longitudinal strain, ΔF is the difference of the compressive forces, A_0 is the initial section of the sample and Δh is the height difference between the initial state h_0 and the compressed state.

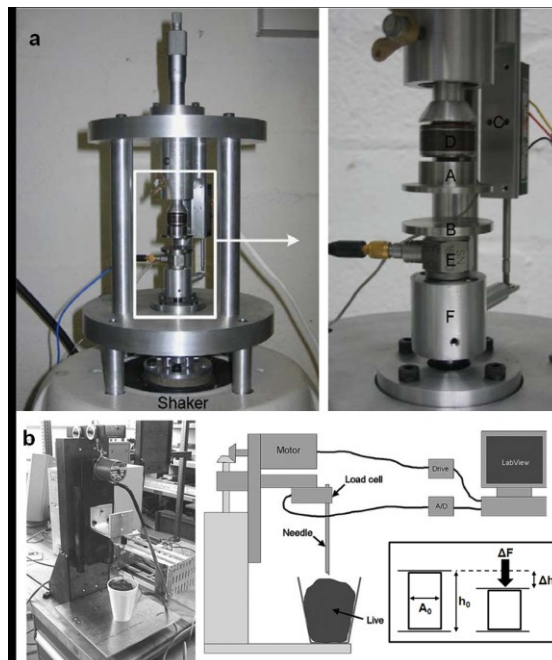


Figure 1.14: *a: Custom built for the characterization of mechanical properties of liver (Schwartz et al., 2005). b: Experimental setup high speed cyclic testing rig. (A) Top platen; (B) bottom platen; (C) LVDT transducer; (D) static load cell; (E) dynamic load cell; and (F) connection with shaker (Van Loocke et al., 2009).*

The characterization of mechanical properties of several tissues using the compression tests are summarized in this table:

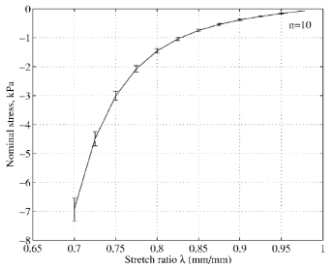
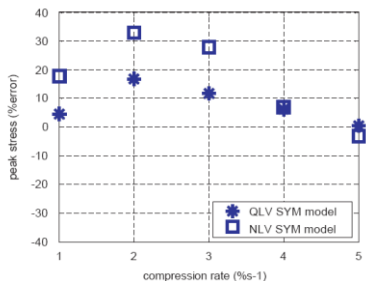
Authors	Samples	Applied parameters	Measured parameters
(Miller, 2000)	Liver and Kidney (Monkey)	Speeds : 5 à 500 cm/s	Mooney-Rivlin coefficients $C_{10} = C_{01} = 6.2$ kPa $C_{20} = C_{02} = 3.5$ kPa
(Schwartz et al., 2005)	Liver (Deer Family)	Speeds : 2 à 10 mm/s	Young's modulus $E = 2.5$ kPa Viscosity $\eta = 600$ Pa.s
(Hollenstein et al., 2006)	Liver (Bovine) 15 mm x 50 mm	Preload : 0.2 N Strain rate : 0.5%/s	Young's modulus $E_1 = 1.1$ MPa $E_2 = 38.5$ MPa
(Roan and Vemaganti, 2006)	Liver (Bovine)	Preload : 0.002 N Strain rate : 0.01/s	Curve of Stress – Stretch 
(Miller and Chinzei, 1997)	Brain (Pork) 30 mm x 13 mm	Force : 0.5 à 9 N Speeds : 0.005 à 500 mm/min	Mooney-Rivlin coefficients $C_{10} = C_{01} = 0.8$ kPa
(Gao et al., 2009)	Liver (Cochon) 51 mm x 11 mm	Vitesse : 1.3 mm/s	Stress – Stretch Ogden model $C_1 = 0.002$ kPa, $C_2 = 169$ kPa $\alpha_1 = 25$, $\alpha_2 = -16.63$ Chui model $C_1 = 60$ MPa, $C_2 = 1.55$ MPa et $C_3 = 100$ MPa
(Van Loocke et al., 2009)	Muscle (Porcine)	Mean compression level of 25% was applied and cycles of 2% and 10% amplitude were performed at 0.2–80 Hz	Percentage errors between experimental and theoretical peak stresses 

Table 1-2: *In vitro* compression tests performed on biological tissues

1.2 Indentation tests

Indentation tests are used to determine the mechanical properties (young modulus) of a material to deformation. The sample is placed on a plane surface with a tip placed vertically above. Then this tip descends to contact with the sample and the indentation depth is measured in function of the stress applied by the probe in order to deduce the sample mechanical properties.

Indentation tests have been studied by some authors on skeletal muscle (Gefen et al., 2005; Palevski et al., 2006; Zheng et al., 1999). However, these have considered the muscle tissue as isotropic and having linear elastic and viscoelastic properties (Carter et al., 2001).

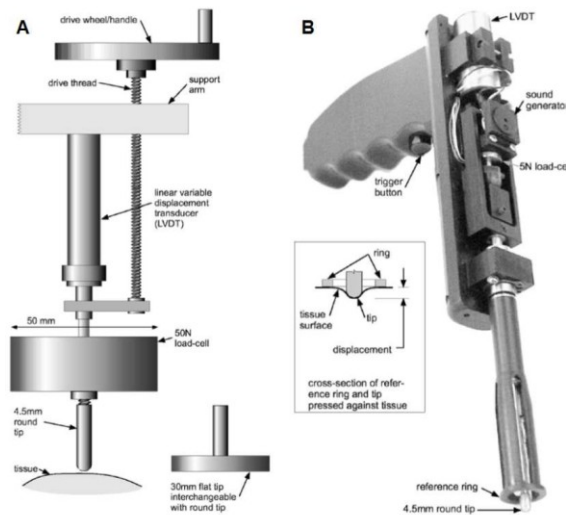


Figure 1.15: Experimental setup for testing by indentation(Carter et al., 2001)

1.3 Dynamic Mechanical Analysis (DMA)

Dynamic mechanical analysis uses a parallel shear motion between the two plates rather than the rotational motion on a frequency interval. The DMA test applies a sinusoidal stress (σ) to the sample and measures the deformation (ϵ) as well as the resulting phase shift (δ). From these parameters, we can consider the complex shear modulus (G^*) composed of a storage modulus (G') and a loss modulus (G'').

$$G^* = G' + i \cdot G'' = \frac{\sigma}{\epsilon} \cos\delta + i \cdot \frac{\sigma}{\epsilon} \sin\delta$$

A study used DMA to calculate the ex vivo shear modulus from the muscle leg of rats. The ranges of elastic properties is between 22 and 33kPa within a frequency range of 1 to 100 rad/s (van Turnhout et al., 2005). Other studies showed the complex shear modulus ($G' = 2.94$

kPa, $G'' = 1.27$ kPa) of the bovine liver at 62.5 Hz (Klatt et al., 2010a) and a variation of the storage modulus and the loss modulus as a function of frequencies (10 - 80Hz).

1.4 Torque meter technique

The torque meter technique is used to define the elastic properties of the skin. This technique applied a torque through a disc joined to the surface of the skin. The measured rotation angle allows to characterize the extensibility of the skin (Evans, 1965). From this test, one obtains several elastic properties of the skin such as Young's modulus and shear modulus (Agache et al., 1980; Grahame, 1969; Tomlinson et al., 1969), was measured. Subsequently, the viscoelastic coefficient (Duggan, 1967; Ridge and Wright, 1966) was also calculated.

2. In vivo methods

The different techniques that characterize the functional properties of the muscle are defined hereafter.

2.1 Palpation

Palpation is the process of using hands to examine the body especially while perceiving/diagnosing a disease or an illness. The rigidity of biological tissues is of great importance for the clinical diagnosis, and palpation is currently used by clinicians to evaluate the rigidity of available organs. Indeed, this information allows clinicians to identify pathological tissues that have a greater rigidity than normal tissues. However, palpation is a subjective method that depends on the physician's experience. That is why that the diagnosis should be confirmed by other procedures.

2.2 Electromyography (EMG)

Electromyography is an attractive muse because it supplies easy access to physiological processes that cause the muscle to generate force, produce movement and accomplish the countless functions which allow us to interact with the world around us. Electromyography is an experimental technique for detecting myoelectric signals during a contraction from recording and analyzing these signals (Basmajian and De Luca, 1985). There are two types of EMG: surface EMG and intramuscular EMG. Surface EMG assesses muscle function by registering muscle activity from the surface above the muscle on the skin by surface electrodes. The Surface EMG represents the muscular activity, characterizes the different action potentials and translates the recruitment process of the muscular fibers.

However, its interpretation faces a number of methodological factors such as the distance of the muscular fibers to the electrodes, the property of the electrode filter and the problem of the orientation of the electrodes relative to the main axis of the muscle. Also intrinsic muscle factors, such as skin, adipose tissue, conjunctive tissue, fibers diameters, muscle length, spatial arrangement of active fibers and pennation angle could be a problem. Moreover physiological **factors** such as the level and the type of muscle fiber, and intramuscular temperature, (Farina et al., 2004; Hogrel, 2005; De Luca, 1997; Merletti et al., 2009) can interfere with the result. All of these factors reside in the signal noising and a better myoelectric signal acquisition (De la Barrera and Milner, 1994).

2.3 Myotonometric

The myotonometric method has been demonstrated to be an effective, reproducible and accurate technique (Bizzini and Mannion, 2003; Viir et al., 2006), but is not applicable for the following conditions: thin muscle, muscle with small mass, obese persons ($BMI > 30 \text{ kg} \cdot \text{m}^{-2}$), patients suffering from severe pain, muscle which are palpable in small volume, and muscles which are located under other muscles (Gapeyeva and Vain, 2008).

2.4 Elastography techniques

2.4.1 Introduction

Biopsy is always the reference method in detecting abnormal tissue changes, revealed by mechanical modifications. Nevertheless, biopsy remains an invasive and a painful method providing an analysis of a small piece of target tissue (local measurement). Thus, the non-invasive evaluation of the functional properties of soft tissues is a key point for the clinicians to evaluate the behavior of various tissues such as muscle (Bensamoun et al., 2006a), brain (Sack et al., 2008), kidney (Leclerc et al., 2013a), prostate (Sahebjavaher et al., 2014), breast (Sinkus et al., 2005a), and liver (Klatt et al., 2010a) before and after treatment (Debernard et al., 2011b).

The elastography techniques are performed with either ultrasound (US) or magnetic resonance (MR) imaging. They have been developed over the past fifteen years to characterize the mechanical properties of soft tissue. The clinical diagnosis, established from imaging tests (MRI, CT, and ultrasound), is mainly based on an analysis of the structural properties of the tissue represented by its texture and morphology (Beers et al., 2011; Zuberi et al., 1999). In addition to the anatomical images, a second one can reveal the mapping of the

stiffness tissue, used for clinical diagnosis (Bensamoun et al., 2006a, 2008a; Niitsu et al., 2011; Shinohara et al., 2010), and the follow-up of disease.

2.4.2 Ultrasound (US) elastography techniques

The ultrasound elastography is one of the most common elastography techniques and different principles are used in order to measure deformations within the tissue.

Different applications can be grouped into a variety of ultrasound elastography techniques:

1. **Quasi-static elastography:** An arbitrary deformation is applied using a pressure sensor and the displacement is visualized by US. In other words, the quasi-static ultrasound elastography is initially based on the estimation of the axial tissue displacement and strain, which corresponds to the displacements estimated along both the direction of insonification and tissue deformation. A characterization of the ultrasonic radiofrequency echo signals, captured from a standard clinical ultrasound diagnostic equipment (Ophir et al., 1991), is performed to measure the elastic parameter.
2. **Sonoelastography:** A mechanical actuator is used to generate shear waves in the tissue. The wave amplitude is obtained by US using the Doppler effect. New applications use two actuators in order to create wave outcome of the interferences. The speed of this wave is slower, which allows the capture of an image with a conventional scanner (Wu et al., 2006).

3. Supersonic Shear Imaging (SSI)

Supersonic shear imaging (SSI) is a new ultrasound-based technique for real-time visualization of soft tissue viscoelastic properties. This technique relies on the ability of the ultrasound probe and therefore the thickness of the adipose tissue can be a limit. In order to build a mapping of the elasticity modulus, the used formula is:

$$E = 3 \cdot \rho \cdot V^2$$

where ρ the density of the tissues: 1000 kg/m^3 .

This technique is based on two principles:

- **Radiation pressure:** Ultrasound is focused at several successive depths generating pushed by radiation force. Each focusing point generates spherical waves which interfere in the manner of a Mach cone creating a planar shear wave. The creation of a single Mach cone allows the characterization of the entire tissue environment, except

at the Mach cone. With this imaging technique, a wave with amplitude of the order of several micrometers (Tanter et al., 2007) is generated.

- **Ultrafast imaging:** It captures images of the propagation of these shear waves. It is performed by ultrafast imaging (Figure 1.16). Ultrafast imaging allows the scanning of the entire imaging plane with a very good temporal resolution in one single acquisition, typically with a frame rate of 5 000 images per second and up to 30 000 images per second in the case of tissues such as the peripheral arteries or the eye.

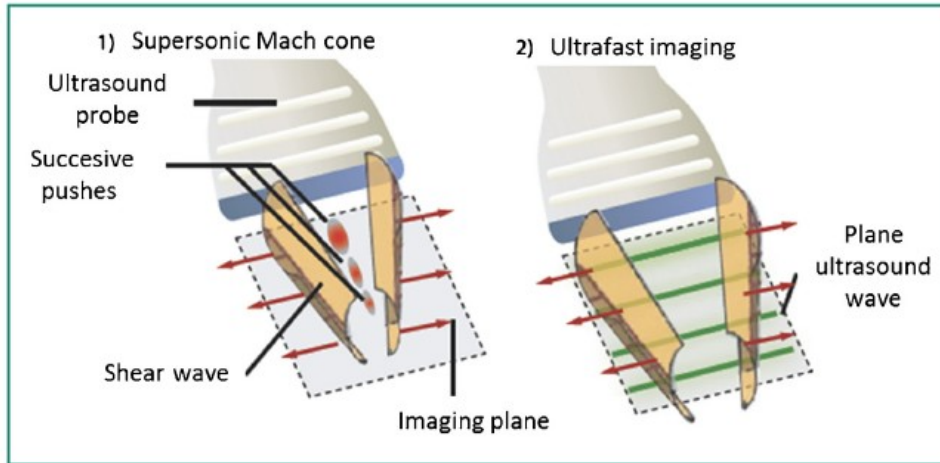


Figure 1.16: 1: the ultrasounds are successively focused at different depths to create pushes by radiation pressure. The constructive interferences of the shear waves form a supersonic Mach cone (in which the speed of the source is greater than the speed of the generated wave) and a quasi-plane shear wave is created; 2: the ultrasound machine then switches into an ultrafast imaging mode to follow the shear wave that is propagating through the medium (Gennisson et al., 2013).

- **Mechanical properties of tissues calculated by SSI.**

This approach has been applied to study the viscoelastic properties of breast lesions (Tanter et al., 2008), liver (Deffieux et al., 2009) and muscles (Deffieux et al., 2009; Gennisson et al., 2010). Muscle applications are on the biceps brachii muscles and brachialis as shown in the following figure (Figure 1.17) for made different loads.

The cartographies of the speed propagation of the shear waves, show an increase in the velocity with respect to the level of contraction.

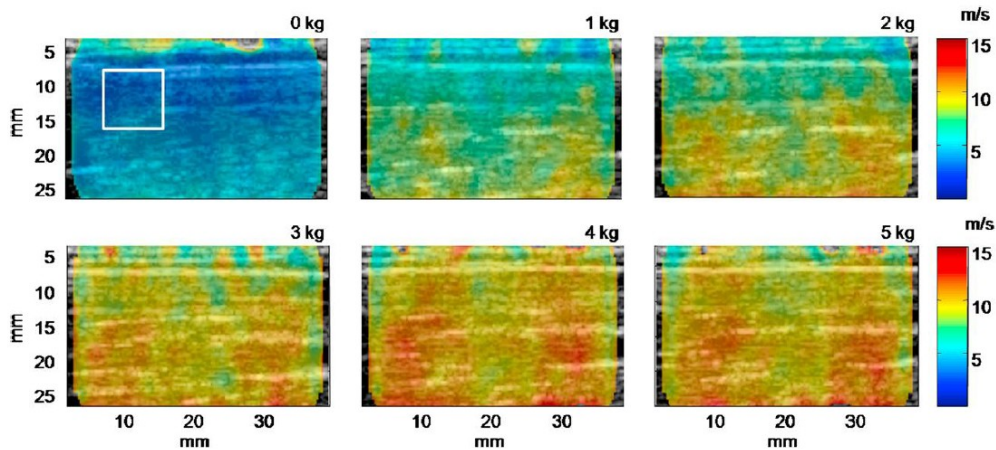


Figure 1.17: Shear waves velocity cartographies, obtained on the biceps brachii and brachialis by Supersonic Shear Imaging technology for different loads (Gennisson et al., 2010).

4. Transient elastography

- 1D transient elastography: the 1D shear elasticity probe

This technique was first developed at the Institute Langevin in 1995 by Catheline et al, 1998. It is based on generating a transient impulse with low frequency pulse (adjustable from 10 Hz to 500 Hz) (little shock) on the medium by a vibrator and recording the shear wave that propagates within the medium by using an ultrasound transducer (Figure 1.18).

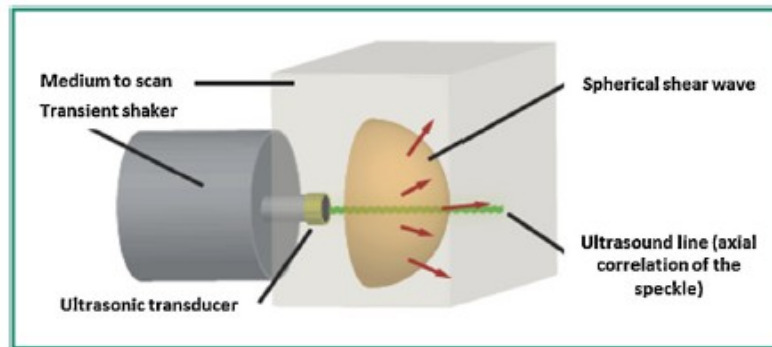


Figure 1.18: The vibrator gives a low frequency pulse (adjustable from 10 Hz to 500 Hz) in the medium creating, among others, a shear wave. The ultrasound transducer, which is placed on the vibrator, thus allows following, by axial intercorrelation of the ultrasound speckle and more than one thousand times per second, the propagation of the shear wave depending on the depth over time. We can then deduce the speed of the shear wave and thus the Young's modulus of the medium (Gennisson et al., 2013).

The front face of the transducer play the role of a piston giving a slight mechanical impulse on the surface of medium, which generates a spherical compression wave as well as a spherical shear wave (Catheline et al., 1999). The detection of the displacement, which is a

function of depth and of time, is made by correlations of retro-diffused echoes (via ultrasound speckle) recorded at a framerate higher than one thousand time per second with a mono-dimensional ultrasound transducer (5 MHz) (Figure 1.19).

By measuring the phase for each depth, we extract the phase speed of the shear wave at the central frequency that leads to an estimation of Young's modulus by considering the medium to be homogeneous, incompressible and non-viscous ($E=3\rho c^2$, where ρ is the density of the medium (kg.m^{-3}) and c is the velocity (m.s^{-2}) of the shear waves propagation).

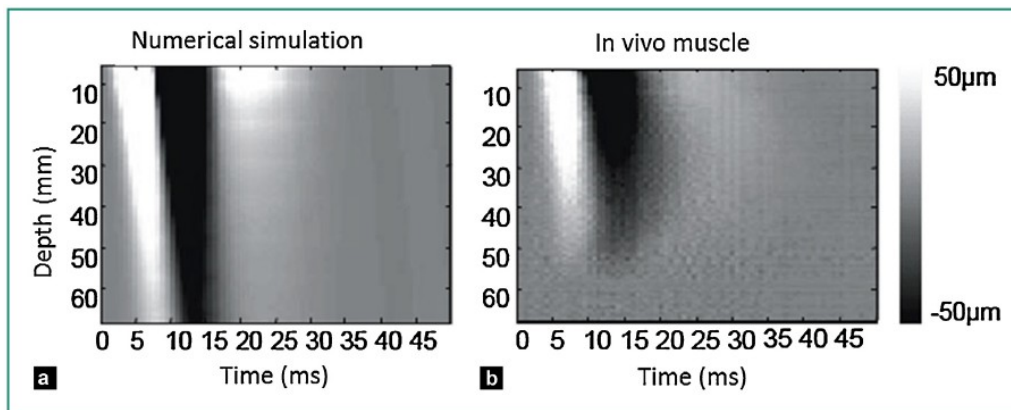


Figure 1.19: Comparison between (a) the numerical simulation of the time/depth profile and (b) the time/depth profile in a muscle in vivo. The slope allows to work back to the speed of the shear wave and thus the Young's modulus of the medium (Gennisson, 2003).

This technique is simple and fast and its practice was extended and marketed by the company echosense (Paris, France) for the detection and monitoring of liver fibrosis. This technique, which was initially developed for quality control in the food industry, was then used in the medical field and developed for the measurement of other mechanical parameters such as anisotropy, viscosity or elastic non-linearity (Catheline et al., 2003, 2004; Gennisson et al., 2003).

- 2D transient elastography

In 1997, the 1D transient elastography technique was extended to 2D which allowed the production of elasticity maps of biological tissues. This technique includes an ultra-fast ultrasonic imaging electronic system that can create up to 5000 frames per second. With such an imaging system, one single low frequency (LF) pulse excitation is necessary to acquire the full data set. A vibrator was fixed to the ultrasound imaging array, which is then used as an impactor to generate a quasi-plane shear wave (Figure 1.20). Once the movie of the propagating shear wave is reconstructed, the wave equation is inverted to recover a map of Young's modulus (Gennisson et al., 2013).

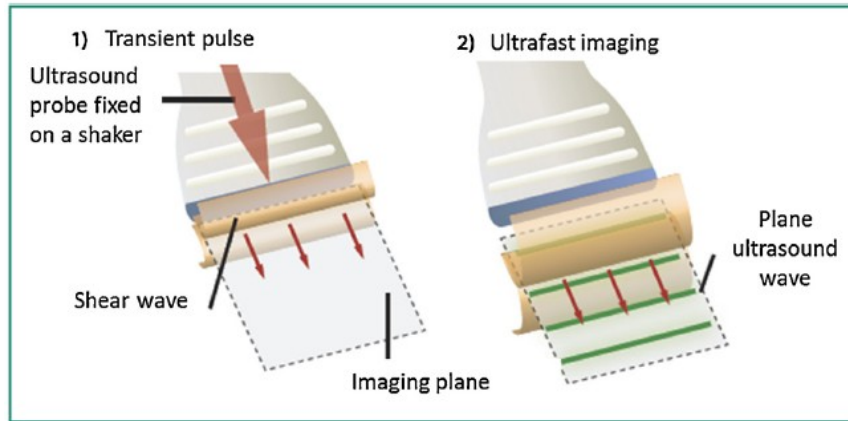


Figure 1.20: The ultrasound array, mounted on a vibrator, gives a low frequency shock in the medium (around 50 Hz). The shear waves generated on the borders of the array interfere within the imaging plane as a quasi-plane wave propagating on the depth; 2: the ultrasound, then, switches into an ultrafast imaging mode to follow the shear wave, propagating through the medium (Gennisson et al., 2013).

- **Mechanical properties of tissues calculated by transient elastography (1D, 2D).**

In 2003 and at Institute Curie, the first in vivo tests were carried out (Figure 1.21). The obtained results were encouraging, but the device was bulky, heavy and difficult to use in practice (Bercoff et al., 2003). This method has been largely applied to determine the mechanical properties of the liver (Castera et al., 2008; Foucher et al., 2006; Friedrich–Rust et al., 2008).

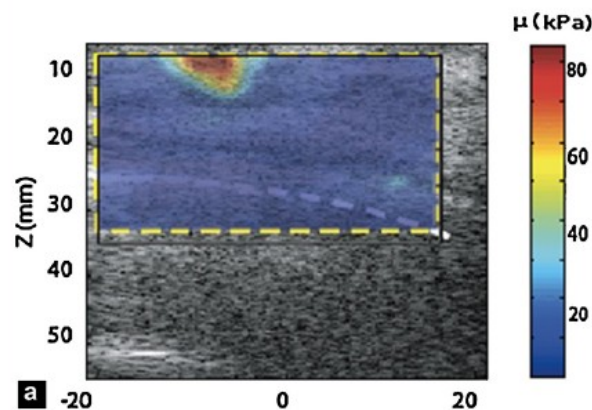


Figure 1.21: a: breast elastography. An adenocarcinoma appears stiffer in the elasticity image (Bercoff et al., 2003).

In 2002, Sandrin et al. calculated the velocity of the shear wave in a human bicep contracted by various loads in function of time and showed that the velocity increases during the

contraction of the muscle and decrease during the unloading (Sandrin et al., 2002) (Figure 1.22).

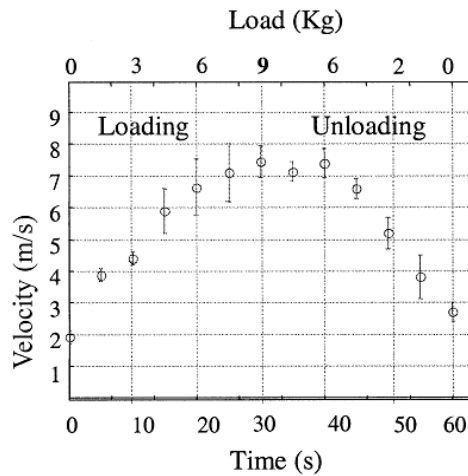


Figure 1.22: The velocity of the shear wave in a human bicep contracted by various loads.

5. Shearwave Dispersion Ultrasound Vibrometry (SDUV)

The interaction between the two beams of very similar frequency (Δf et $f + \Delta f$) causes a radiation force that generates shear waves propagating at a speed C_s . This method was developed by Chen et al. (2004) for the quantitative measurement of the viscoelastic properties. The propagation velocity of shear wave C_s at the frequency ω_s is estimated by measuring the difference of the phase $\Delta\rho_s$ on a propagation path Δr ($C_s = \omega_s * (\Delta r / \Delta\rho_s)$) (Chen et al., 2004). This technique was applied in vivo on beef muscles to determine the elasticity and viscosity parameters along or perpendicular to the fibers (Chen et al., 2009). This method was also applied for in vitro measurements of renal cortex shear elasticity and shear viscosity in healthy swine kidneys (Amador et al., 2011)).

2.4.3 Magnetic resonance elastography (MRE) technique

I. Introduction

The magnetic resonance elastography (MRE) technique associates, as the name suggests, the magnetic resonance imaging (MRI) to visualize the propagation of a shear wave. To the standard MRI sequences (Spin Echo (SE), Gradient Echo (GE), Echo Planar Imaging (EPI) or others), motion-sensitizing gradient (MSG), imposed along a specific direction (switched in polarity at some adjustable frequency (Callaghan and Stepišnik, 1995; Denk et al., 1993), will be synchronized to the local movement, allowing to increase the sensitivity to the phase shift of the spins and thus obtain a better picture of wave propagation. The wave

will be generated with different types of vibrators adapted to the characterized biological tissue.

MRE is a medical imaging technique (Muthupillai et al., 1995), that can non-invasively estimate in vivo the mechanical properties of the tissue. MRE estimates the stiffness of the target tissue based on the displacement caused by the mechanical shear waves.

II. Description of the technique

As any elastography technique, MRE consists of three main steps:

First: The shear waves are induced in the tissue using an external transducer.

Second: The waves are imaged inside the target tissue with MRE sequence.

Third: The resulting displacement data are processed to generate quantitative maps (elastogram) displaying the mechanical properties of the target tissue.

Step 1: Inducing a mechanical deformation in the tissue

- **Different drivers.**

The speaker device, which drives the passive wave generator, is located outside the scanner room to avoid interference. To produce wave, two types of drivers can be used: pneumatic or mechanical. These drivers generate waves at the surface of the biological tissue and must be carefully designed to ensure MR compatibility. The driver is developed as a function of the tissue.

I. Mechanical driver

Sack et al (2008) used a rigid carbon fiber pointer instead of the plastic air tube connected to a driver to characterize the brain (Figure 1.24). However, it was less flexible which limited the orientation, the displacement of the driver in the MRI.

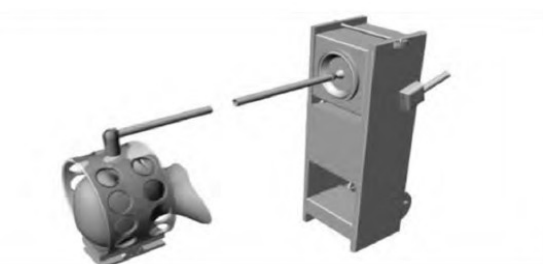


Figure 1.23: MRE head driver with a loud speaker coupled with a long carbon fiber rod (Sack et al., 2008).

II. Round pneumatic driver

Talwalkar et al (Talwalkar et al., 2008) designed a pneumatic MRE transducer for the liver using a loud speaker as the actuator (Figure 1.23). The vibration generated by the speaker travels through an air filled plastic tube to a passive driver placed on the patient's body.

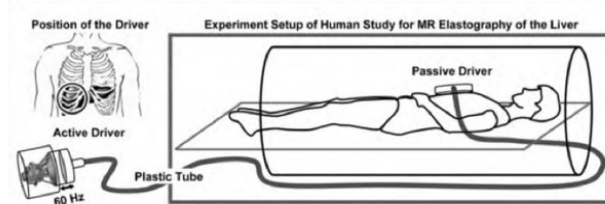


Figure 1.24: MRE liver driver with a loud speaker coupled with a plastic air-filled tube (Talwalkar et al., 2008)

Yin et al (Yin et al., 2007) and Leclerc et al (Leclerc et al., 2012) used a new generation of pneumatic vibrator, which is now used clinically to achieve MRE tests on the liver. This vibrator can transmit waves ranging from 20 to 200 Hz and studies were carried out on the liver at a frequency of 60 Hz.

III. Tube pneumatic driver

Bensamoun et al (2006a) used as a flexible pneumatic driver for the characterization of the thigh muscles using a loud speaker as the actuator. The used vibrator (driver) is silicone tube, this driver is attached around the thigh, and air pressure is sent at 90 Hz from the speaker, the vibration of the tube generates the waves inside the thigh muscle (Figure 1.25).

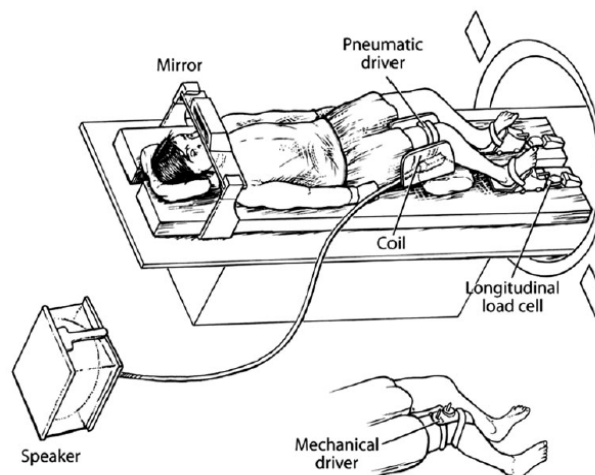


Figure 1.25: MRE tests composed of a driver (tube) with a loud speaker coupled with a plastic air-filled tube (Bensamoun et al., 2006)

Step 2: Imaging the displacement of the wave

The second step aims to visualize the propagation of the shear waves within the target tissue. Thus, in order to spatially map and measure the wave displacement patterns, a phase – contrast MRI technique is used where a motion sensitizing gradient (MSG) echo sequence is imposed along a specific direction and switched in polarity at some adjustable frequency (Callaghan and Stepišnik, 1995; Denk et al., 1993). Trigger pulses synchronize an oscillator unit that drives a transducer, coupled with the surface of the target tissue to be imaged, to induce shear waves in the object at the same frequency as the motion-sensitizing gradient.

During the MRE experiment, any cyclic motion of the spins in the presence of these motion-sensitizing gradients causes a measurable phase shift ϕ in the received MR signal. The displacement at each voxel can be calculated from the measured phase shift. The phase shift caused by a propagating mechanical wave with a wave vector \vec{k} within a medium at a given frequency ($1/T$) in the presence of a cyclic motion-sensitizing gradient (MSG) is given by (Muthupillai et al., 1995, 1996) :

$$\phi(\vec{r}, \theta) = \frac{\gamma NT(\vec{G}_0 \cdot \vec{\xi}_0)}{2} \cos(\vec{k} \cdot \vec{r} + \theta),$$

where ϕ is the phase shift, \vec{r} is the spin position vector, θ (rad) is the relative phase of the magnetic and mechanical oscillations, γ ($\text{rad} \cdot \text{s}^{-1} \cdot \text{T}^{-1}$) is the gyromagnetic ratio of the tissue proton, N is the number of gradient pairs used to sensitize the motion, T (s) is the period of the MSG, \vec{G}_0 is the MSG gradient vector, \vec{k} is the wave vector and $\vec{\xi}_0$ is the displacement amplitude vector.

The accumulated phase shift is proportional to its displacement. The phase shift is also proportional to the period of the MSG (T) and the number of gradient pairs (N). High sensitivity to small amplitude synchronous motion can be achieved by accumulating phase shifts over multiple cycles of mechanical oscillation and the MSG waveform.

An example of a MRE sequence is shown in the figure below.

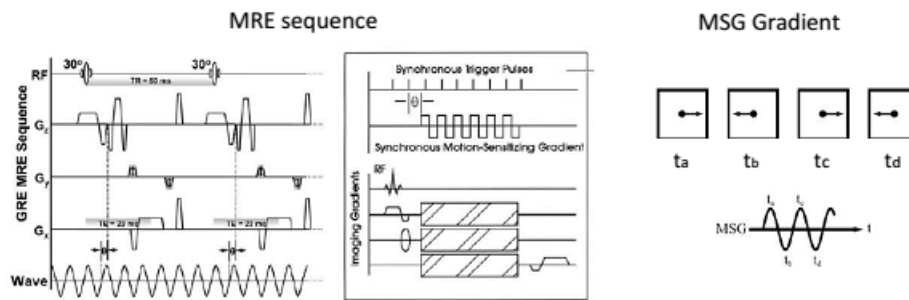


Figure 1.26: Schematic diagram of MRE sequence. Modified extracts (Manduca et al., 2001; Yin et al., 2007)

Thus, the obtained MR image contains both the background phase (anatomical image) and the propagating wave information (phase image), which is typically separated by collecting 2 images with opposite MEG polarities and calculating a phase-difference image. This phase-difference image has only the motion information and is referred to as a wave phase image (Figure 1.27).

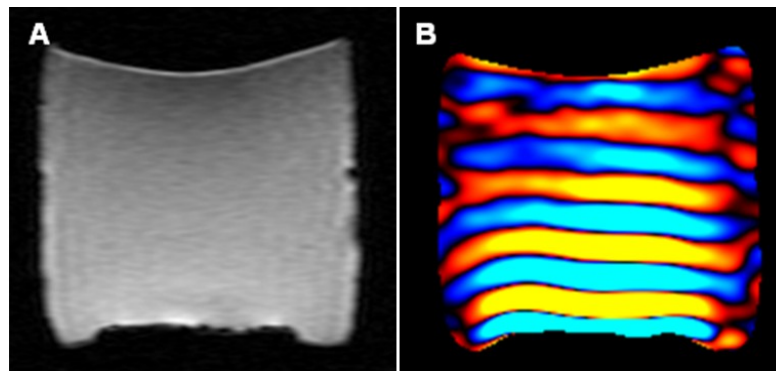


Figure 1.27: Images obtained during an MRE sequence: anatomical image (A) and phase image (B). The example is taken from a phantom.

Step 3: Determination of the mechanical properties.

MRI techniques coupled with elastography sequence allowed to follow the tissue motion and to measure the deformation of the internal tissues (Fowlkes et al., 1995) to image the mechanical properties.

Other MRE techniques use phase contrast imaging that consists of encoding the movement in the phase of the MRI signal. From the MRE displacement data (image phases), we can extract the mechanical properties such as shear modulus by using a variety of reconstruction techniques based on the equation of motion. The complex shear modulus (G^* , kPa) is related

to an elastic component (G' , kPa), that represents the real part, and a viscous component (G'' , Pa.s), that represents the imaginary part.

Different methods used to calculate the mechanical properties, are discussed below:

- **Manual estimation of shear modulus from the phase image**

The displacement of the waves is analyzed, in the phase image, through a quantification of the wavelength (λ) inside the target tissue. Subsequently, assuming that the muscle is linear elastic, isotropic, homogeneous and incompressible, the local shear stiffness (μ) is calculated using the following equation:

$$\mu = \rho \cdot (f \cdot \lambda)^2,$$

where ρ is the muscle density of the biological tissue, fixed to 1000 kg/m^3 because the majority of the tissue content is water, f is the oscillating frequency and λ is the wavelength.

From the phase image, a profile is drawn in the direction of the wave propagation direction for deriving the wavelength (Figure 1.28).

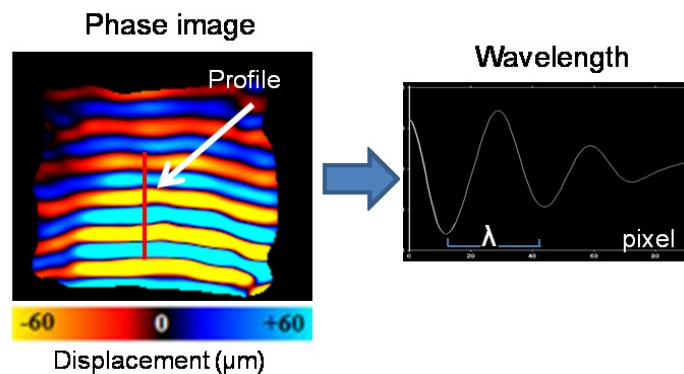


Figure 1.28: Measurement shear modulus (μ , kPa) from the calculation of the wavelength λ (mm) by placing a profile (red) in the direction of the wave propagation direction on the phase image.

- **Cartography of the shear modulus**

From the phase image, it is possible to generate cartography of the shear modulus. To do so, different algorithms can be used.

In the literature, several algorithms have been used such as the algorithm Local Frequency Estimation (LFE) (Manduca et al., 1996a, 2001), the Matched Filter (MF), the Phase Gradient (PG) and the direct inversion (DI). In 2001, Manduca described different algorithms used in magnetic resonance elastography and the main algorithms are described below.

I. Local Frequency Estimation (LFE)

This algorithm estimates at each pixel, the wavelength λ (mm) based on the local spatial frequency of the shear wave and using the equation previously established $\mu = \rho \cdot (f \cdot \lambda)^2$. LFE has been implemented for MRE data reconstruction by Manduca et al. The LFE enables to calculate the shear modulus assuming an isotropic local homogeneous, incompressible and no attenuation.

This algorithm has been tested and shown to be a robust algorithm (Manduca et al., 2001), insensitive to noise (Manduca et al., 1996a), easily extended to 3D (Manduca et al., 1996b), and is extremely sensitive to interference waves. One disadvantage of LFE is the limitation of the resolution where at sharp boundaries the LFE results in blurred estimates. However, this algorithm is not suitable for measuring the shear modulus if the size of the object is smaller than half the wavelength since the elasticity estimation will be incorrect.

II. Phase gradient

The phase gradient (PG) algorithm is an inverse approach based on the estimation of the wavelength along a designated profile (Manduca et al., 2001). The harmonic component of the shear wave was extracted from this method at the excitation frequency with a temporal Fourier transform, and produced both an amplitude and phase of the propagation wave that determine the harmonic at each pixel in the image. The wavelength, calculated from the gradient of this phase can be characterized by a linear curve fitting algorithm (Ringleb et al., 2007) and is equal to the wave number k . The gradient of this phase is inversely proportional to the local wavelength λ :

$$\lambda = FOV \cdot 2\pi / k \cdot N$$

where FOV is the field of view in meters and N is the number of pixels in the field of view.

In principle, the phase gradient method can have a very high resolution, but it is very sensitive to noise and some averaging of the gradient is usually necessary. In addition, it gives inaccurate results in the presence of a superposition of waves or a complex movement (Catheline et al., 1999).

III. Algebraic inversion of the differential equation (AIDE)

Algebraic inversion of the differential equation (AIDE) (Manduca et al., 2001; Oliphant et al., 1999, 2001) stands for for the direct inversion of the motion equations

assuming local homogeneity (Oliphant et al., 1999, 2001). The aim is to determine the components of the matrix A by measuring locally at each pixel, the local derivative of the displacement or phase.

$$A = \begin{bmatrix} A_{11} & A_{12} \\ A_{21} & A_{22} \\ A_{31} & A_{32} \end{bmatrix} = \begin{bmatrix} \frac{\partial^2 U_i}{\partial^2 x_i x_1} & \frac{\partial^2 U_1}{\partial^2 x_i x_i} \\ \frac{\partial^2 U_i}{\partial^2 x_i x_2} & \frac{\partial^2 U_2}{\partial^2 x_i x_i} \\ \frac{\partial^2 U_i}{\partial^2 x_i x_3} & \frac{\partial^2 U_3}{\partial^2 x_i x_i} \end{bmatrix} \quad (1)$$

The linear elastodynamic equation or Navier equation, with the assumption of local homogeneity and a harmonic motion which allows to deduce the Lamé coefficients μ and λ is:

$$(\lambda(\vec{x}) + \mu(\vec{x}))\nabla(\nabla \cdot \vec{u}(\vec{x}, t)) + \mu(\vec{x})\nabla^2 \vec{u}(\vec{x}, t) = -\rho(\vec{x})\omega^2 \vec{u}(\vec{x}, t)$$

Then the solution is given by

$$\begin{bmatrix} \lambda + \mu \\ \mu \end{bmatrix} = -\rho\omega^2 (A^* A)^{-1} A^* \begin{bmatrix} U_1 \\ U_2 \\ U_3 \end{bmatrix} \quad (2)$$

where A^* is the conjugate transpose of A.

Assuming that the longitudinal pressure varies slowly, its derivative is negligible. Thus, the inversion is given by (2) without the λ term. It is not always necessary to know the polarization of the movement in the three directions of the space.

$$\begin{bmatrix} \mu \\ \mu \end{bmatrix} = -\rho\omega^2 (A^* A)^{-1} A^* \begin{bmatrix} U_1 \\ U_2 \\ U_3 \end{bmatrix} \quad (3)$$

Assuming an incompressible material, Helmholtz inversion equation will be:

$$\mu = -\rho\omega^2 \frac{\vec{u}}{\nabla^2 \vec{u}}$$

This equation allows the estimation of the shear modulus (μ) from a single polarization of motion.

2.4.4 Applications

The non-invasive evaluation of the functional properties of soft tissues have been evaluated for: liver (Garteiser et al., 2013; Leclerc et al., 2013a; Yin et al., 2007), muscle (Debernard et al., 2013; Domire et al., 2009; Klatt et al., 2010b; Ringleb et al., 2007), breast (Sinkus et al., 2005a), brain (Green et al., 2008; Sack et al., 2008), heart (Elgeti et al., 2010; Kolipaka et al., 2009a), lungs (Mariappan et al., 2011; McGee et al., 2008), cartilage (Lopez et al., 2008), prostate (Sahebjavaher et al., 2013), spleen (Mannelli et al., 2010) and the kidney (Bensamoun et al., 2011b). The different tissues, using MRE, are described hereafter.

1. Liver tissue

The technique of magnetic resonance elastography (MRE) is used to characterize the mechanical properties of the liver for obese patients and with ascites patients around the liver. Clinical studies have demonstrated that MRE can distinguish between fibrotic liver and healthy livers based on the changes of the tissue stiffness (Asbach et al., 2010; Huwart et al., 2008; Leclerc et al., 2013a).

Rouvière et al (Rouvière et al., 2006) were one of the first who studies 12 healthy subjects and 12 patients with various liver diseases and they found that the shear moduli were 2.7 kPa and 5.6 kPa for the healthy liver and patients, using a 90 Hz frequency, respectively.

In the study of Yin et al. (2007), 35 healthy subjects and 48 patients with different etiologies performed a MRE test. The average shear modulus obtained for healthy liver is 2.20 ± 0.31 kPa. For the 48 patient groups, the mean of the shear modulus is 5.80 ± 2.57 kPa and they represented the MRE maps of displacement to show that the wavelength (λ), at the frequency of excitation 60 Hz, is longer in the liver with fibrosis (Figure 1.29e) than its healthy counterpart (Figure 1.29b). The reconstructed stiffness of the fibrotic liver (Figure 1.29f) is significantly higher than in healthy liver (Figure 1.29c). A cut-off of 2.93 kPa, based on ROC analysis, was established as the optimal threshold for distinguishing healthy to fibrotic livers.

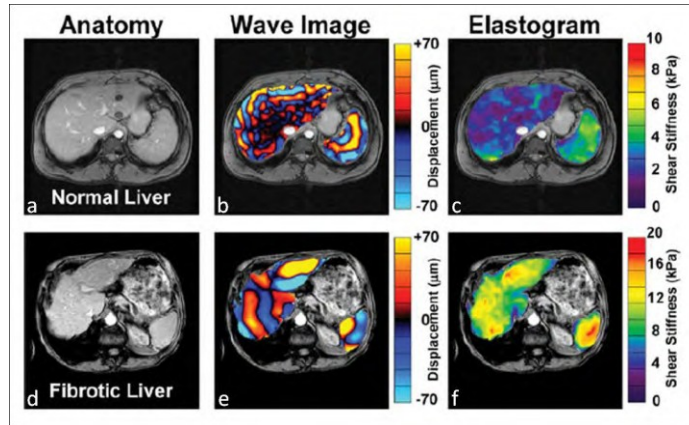


Figure 1.29: MRE results for normal (35 volunteers) and fibrotic (48 volunteers) livers. Anatomical images for normal (a) and fibrotic (d) liver. Displacement images for normal (b) and fibrotic (e) liver. Stiffness maps for normal (c) and fibrotic (f) liver. (Yin et al. 2007)

2. Brain tissue

Recently, several studies used MRE to characterize the mechanical properties of brain (Atay et al., 2008; Green et al., 2008; Ieva et al., 2010; Kruse et al., 2008; Murphy et al., 2011, 2012; Romano et al., 2012; Sack et al., 2008; Schregel et al., 2012; Vappou et al., 2007, 2008; Xu et al., 2007a, 2007b). The variation of the mechanical properties have been one of the criteria to determine the diseases such as hydrocephalus, Alzheimer's disease (AD), multiple sclerosis (MS) and brain tumors.

The work of Green et al. (2008) was to investigate viscoelastic properties of a normal brain tissue via the full 3D reconstruction method by using MRE, based on spin echo and at an excitation frequency of 80 Hz. The in vivo MRE results for elasticity and the first measurements of the viscous properties of grey and white matter regions of the brain showed that the elasticity in grey matter was significantly higher (3.1 kPa) than white matter (2.7 kPa) while there was no significant difference between the two in terms of viscosity.

Sack et al (2008) used the MRE technique at driving frequencies of 25 and 50 Hz for a phase sensitive 2D echo planar imaging acquisition. The elastic results of this study ($\mu=1.17\pm 0.03$ kPa at 25Hz and $\mu=1.56\pm 0.07$ kPa at 50 Hz) show that the shear modulus is about one-third higher with higher vibration frequencies. In contrast, no dispersion was observed for the shear viscosity with mean values of $\eta=3.1\pm 0.4$ Pas and $\eta=3.4\pm 0.2$ Pas at 25 and 50 Hz respectively (Figure 1.30).

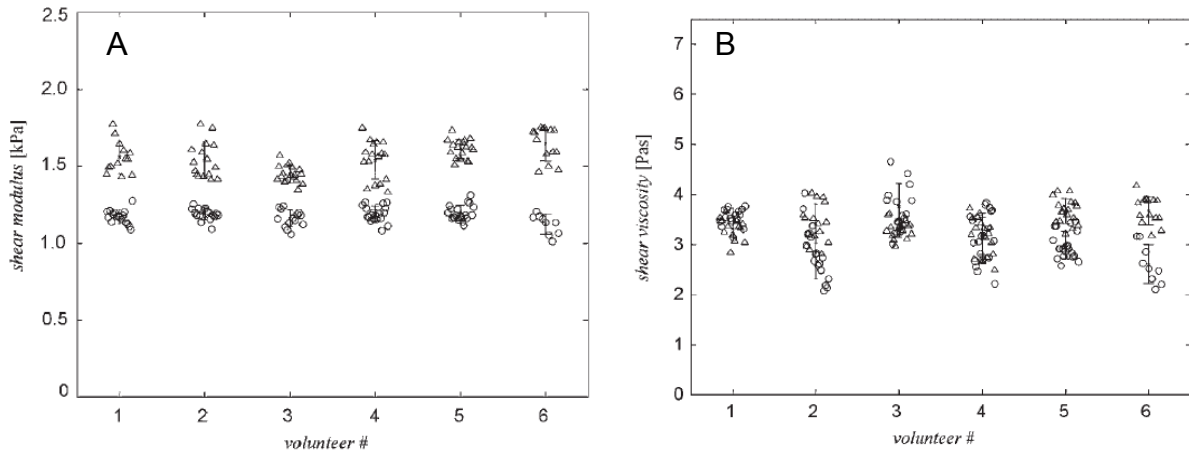


Figure 1.30: Experimental data for shear moduli (A) and shear viscosity (B) acquired at 25 Hz (circles) and 50 Hz (triangles) wave excitation. The error bars correspond to the standard deviations of the data for each frequency and volunteer (Sack et al., 2008).

3. Muscle tissue

3.1 Healthy muscles

A lot of studies have used MR elastography (MRE) technique under various testing condition to analyze the mechanical behavior of healthy muscles such as biceps brachii (Dresner et al., 2001; Papazoglou et al., 2006; Sack et al., 2002), vastus medialis, vastus lateralis, sartorius (Bensamoun et al., 2006a, 2007, 2008b; Debernard et al., 2011b; Domire et al., 2009) and the trapezius muscles (Chen et al., 2007, 2008). Basford et al. (2002), Heers et al. (2003) and Jenkyns et al. (2003) proved that the elasticity values of the tibialis anterior (TA) and (lateral gastrocnemius) (LG) at 150 Hz are in the same range in passive condition. Klatt et al. (2010b) demonstrated that the elasticity increases with the frequency and found that the elasticities of the quadriceps femoris, for healthy subjects, vary from 0.77 to 2.02 kPa in the frequency range of 25 to 62.5 Hz. Green et al (2012) used MRE to follow the physiological response of the gastrocnemius muscles after eccentric exercise. It was found that muscle elasticity increased significantly 48 hours after exercise. Even under the same testing frequencies, different muscle groups have different elasticity values. The elastic properties calculated in several studies were summarized in the table below.

Authors	Muscles types	Excitation frequency (HZ)	Shear modulus (kPa)			
			Relaxed muscle	Level (MVC)-state	Contracted muscle	
Dresner et al 2001	Biceps	150	27.3 ± 11.9		-	
Sack et al., 2002	Biceps	200	21±3		-	
Basford et al 2002	TA	150	12 ± 0.4		-	
	MG		24.9 ± 0.7		-	
	LG		16.2 ± 0.2		-	
	Sol		16.8 ± 0.2		-	
Heers et al 2003	TA	150	11.9 ± 0.6		-	
	MG		20.3 ± 1.1		-	
	LG		16.4 ± 0.2		-	
	Sol		16.4 ± 0.2		-	
Jenkyn et al 2003	TA	150	12.3		-	
	LG		22		-	
Uffmann et al., 2004	Biceps	142	17,9±5,5		-	
	FDP		8.7 ±2.8		-	
	LG		9.9 ± 6.8		-	
	Sol		12.5 ± 7.3		-	
Papazoglou et al., 2006	Biceps	75 - 200	29,3±6,2		-	
Bensamoun et al 2006	Sr	90	7,53±1,6		-	
				10%MVC	4,83±1,68	
	VM	90	3,91±1,2	20% MVC	6,4±1,79	
Brauck et al., 2007	Calf muscles	100	3,83±0,24	5% MVC	18,52±1,26	
				10% MVC	19,18±1,21	
				15% MVC	19,13±1,11	
				20% MVC	19,75±0,99	
Klatt et al 2010	QF	25	0.77 ± 0.14			
		37.5	1.18 ± 0.15			
		50	1.52 ± 0.1			
		62.5	2.02 ± 0.14			
Debernard et al. 2011	VM	90	4,03±1,23	10% MVC	7,33±1,23	
				20% MVC	12,97±0,87	
Green et al., 2012	MG	60	1,15±0,23	1 hour after eccentric exercise	1,25±0,21	
				48 hour after eccentric exercise	1,38±0,27	
				1 week after eccentric exercise	1,18±0,23	
	Sol			1 hour after eccentric exercise	1,10±0,27	
				48 hour after eccentric exercise	1,06±0,2	
				1 week after eccentric exercise	0,96±0,22	
Green et al.2013	MG	75 – 118 Hz	μl = 0.86±0.15		-	
					-	
	Sol			μ⊥ = 0.66±0.19		
				μl = 0.83±0.22		
				μ⊥ = 0.65±0.13		-
				μl = 0.78±0.24		-
TA	μ⊥ = 0.66±0.16					

Table 1-3: Mean of the shear modulus (μ) of healthy muscles at rest and in contraction. Several muscles are mentioned such as biceps, flexor digitorum profundus (FDP), tibialis anterior (TA), medial gastrocnemius (MG), lateral gastrocnemius (LG), soleus (Sol), vastus lateralis (VL), vastus medialis (VM), Sartorius (Sr), and the quadriceps femoris (QF). “ \perp ”

denotes the stiffness measured perpendicular to the muscle fibers, “l” denotes stiffness measured parallel to the muscle fibers. MVC: maximum voluntary contraction.

- : no data

3.2 Pathological muscles

It is well known that the mechanical properties of skeletal muscle changes due to disease and eccentric exercise. Basford et al. (2002) were the first to apply the MRE technique on paraplegic muscles and poliomyelitis, showing an increase in the shear modulus in the case of these pathologies muscle. In addition, the MRE was used in the evaluation of mechanical properties in patients with hyperthyroidism (Bensamoun et al., 2007) and hypogonadism (Brauck et al., 2007). More over, McCullough et al (2011) used MRE to distinguish between myositis patients to normal healthy subjects. Muscle inflammation with myositis show a decrease in the elasticity in the case of these pathologies.

Authors	Muscles types	Pathological muscle	Shear modulus (kPa)	
			Left leg (relaxed)	Right leg (relaxed)
Basford et al., 2002	Tibialis anterior	Paraplegia	24.68±9.47 kPa	35±13.78 kPa
		Poliomyelitis	121.02±8.13 kPa	43.78±0.34 kPa
	Medial gastrocnemius	Paraplegia	34.79±5.59 kPa	68.54±22.38 kPa
		Poliomyelitis	60.91±0.11 kPa	32.36±0.19 kPa
	lateral gastrocnemius	Paraplegia	42.46±8.59 kPa	42.39±10.67 kPa
		Poliomyelitis	28.8±0.68 kPa	22.73±0.91 kPa
	Soleus	Paraplegia	44.86±10.8 kPa	45.2±10.94 kPa
		Poliomyelitis	62.68±1.30 kPa	20.49±3.38 kPa
Chen et al.,2007; 2008	Trapeze	Myofascial	Adjacent muscle (relaxed) 6.2±0.8 kPa	Taut band (relaxed) 9±0.9 kPa
Bensamoun et al.,2007	Vastus medialis	Hyperthyroidism	Before treatment (relaxed) 2.11±0.61 kPa	After treatment (relaxed) 5.52±1.52 kPa
Brauck et al.,2007	Calf muscles	Hypogonadisme	13.42±0.92 kPa	19.54±2.19 kPa
McCullough et al., 2011	Vastus medialis	Myositis	Relaxed Decrease	Contraction No different
Bensamoun et al., 2015	Vastus medialis	Duchenne muscular	Relaxed	10% MVC
		dystrophy (DMD)	4.75 ±0.50 kPa	7.50 ± 0.62 kPa

Table 1-4: Mean of the shear modulus (μ) for pathological muscles at different condition. MVC: maximum voluntary contraction

D. Phantoms developed for elastography

In the field of radiology, phantom (object-test) means any object mimicking the physical properties of human tissues. Test-objects are available within the CIRS Company to perform different studies directly in clinical environment. However, most phantoms, presented in the literature, were designed by the research teams themselves to understand better the investigated biological tissues. The creation of a phantom aims to simulate the mechanical behavior of the organ to be characterized *in vivo*. Thus, the experimental parameters of the elastography techniques (MRE, US) used could be tested *in vitro* before to be applied *in vivo*. In addition, the phantom could be used for calibration and the verification of the phase image. In the literature, phantoms were made with different compositions such as agarose (Chen et al., 2005a, 2007; Hamhaber et al., 2003; Luo et al., 2006; Normand et al., 2000; Papazoglou et al., 2006; Ringleb et al., 2005), bovine gels (Chen et al., 2007, 2008), wirosil® (Chen et al., 2006; Kolipaka et al., 2009a), plastisol® (Leclerc et al., 2012; Samani et al., 2003) and zerdine hydrogel (Oudry et al., 2014). In the literature, the phantoms were used for MRE technique to:

- Study the optimization of the driver: frequency (Chen et al., 2005a, 2006; Leclerc et al., 2012) and boundary conditions (Chen et al., 2005a, 2006; Kolipaka et al., 2009a).
- Study the performance of a driver (Chen et al., 2005b; Hamhaber et al., 2003; Houten et al., 2000; Mariappan et al., 2009a, 2009b; Yin et al., 2008).
- Study the ability of the MRE sequence to detect tumors (Mariappan et al., 2009a), simulated with inclusions inside the phantom (Chen et al., 2008; Houten et al., 2000; Manduca et al., 2003).
- Test the development of inversion algorithms used for the measurement mapping of the mechanical properties (Houten et al., 2000; Kolipaka et al., 2009a; Li et al., 2012; Manduca et al., 2003; Oida et al., 2004).
- Test the development of new MRE sequences (Kolipaka et al., 2009b).
- Test the development of methods for the characterization of the anisotropy behavior (Namani et al., 2009; Papazoglou et al., 2006).
- Determine new data-processing for the characterization of the viscoelastic properties (Leclerc et al., 2012; Okamoto et al., 2011; Papazoglou et al., 2012; Schregel et al., 2010).

- Valide MRE results with other techniques performed on the same phantom. Correlation of the MRE mechanical properties were realized with ultrasound elastography techniques (Baghani et al., 2009; Oudry et al., 2009a, 2009b), dynamic mechanical analysis (Chen et al., 2005a; Okamoto et al., 2011; Ringleb et al., 2005) and compression tests (Hamhaber et al., 2003; Namani et al., 2009).

1. Mechanical tests

The mechanical properties of the phantom have been performed with different mechanical tests summarized hereafter.

Authors	Samples	Mechanical tests	Test condition	Mechanical parameters
Hamhaber et al., 2003	Agar-agar 40 mm x 50 mm	Compression tests	Speed: 1 mm / s Preload: 0.1 N	Shear modulus $\mu = 4.5$ to 550 kPa
Chen et al., 2005a; Chen et al., 2005b; Ringleb et al., 2005; Chen et al., 2006	Agarose 5.5 x 10 x 2 mm	Dynamic Mechanical Analysis (DMA)	0.5%, 1% shear strain 10% clamping compressive strain 0.1 à 120 Hz	Shear modulus $G' = 10$ to 250 kPa
Luo et al., 2006	Agarose 15 mm x 25 mm	Compression tests		Young's modulus $E = 10$ to 70 kPa
Peters et al., 2005	Gelatine 3 mm x 10 mm	Dynamic Mechanical Analysis (DMA)	Compression : 10 %	Young's modulus $E = 5$ to 20 kPa
Oudry et al., 2009a	Copolymer-in-oil 20 mm x 3 mm	Dynamic Mechanical Analysis (DMA)	Pre-compression:50 mN 1% strain	viscoelastic properties $\mu = 0.6$ to 11 kPa $\eta = 1$ to 258 Pa
Hadj Henni et al., 2011	Silicone Plastisol PVA-C Chitosan Hydrogel Agar-gelatin 5 à 14 m	Hyper-frequency viscoelastic spectroscopy (HFVS)	F= 10 and 1000 Hz	Viscoelastic properties of plastisol $G' = 8$ to 10 kPa $G'' = 0.1$ to 2 kPa
Okamoto et al., 2011	Gelatine 100 mm x 5.8 mm	Dynamic shear test (DST)	F= 20 and 200 Hz.	Viscoelastic properties $G' = 0.7$ à 1.1 kPa $G'' = 0.1$ à 0.4 kPa

Table 1-5: Viscoelastic properties of the phantoms using mechanical tests.

2. Magnetic resonance elastography Tests

Specific driver have been developed in order to apply the MRE technique to the phantoms.

In 2003 Hamhaber et al. (2003) used a mechanical vibrator (Figure 1.31) which will generate shear waves on the surface of a phantom. The custom-made vibrator consisted of a Plexiglas bar with a coil at one side and a contact plate at the other extremity. The middle of the bar was fixed by a slack-free bearing. The coil was driven by a signal generator and a power amplifier which produced sinusoidal signals with the desired frequency and amplitude up to 30 V.

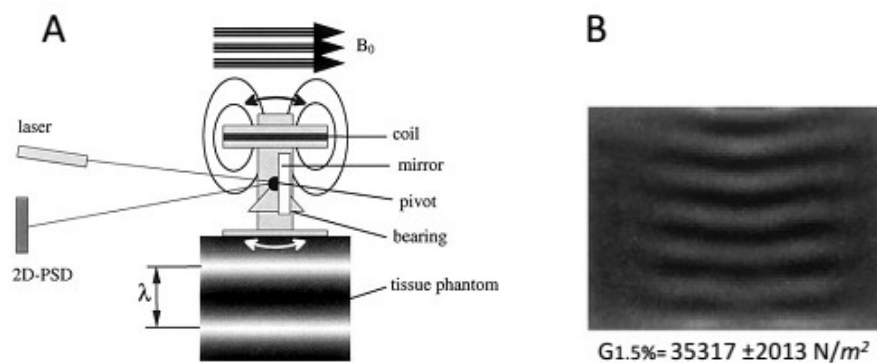


Figure 1.31: A: Principle of the mechanical excitation of shear waves inside the agar gel phantom, B: Phase image (G =shear modulus) (Hamhaber et al., 2003).

A mechanical vibrator in contact with the surface of a phantom (Figure 1.32) was also used by Oida et al. (2004).

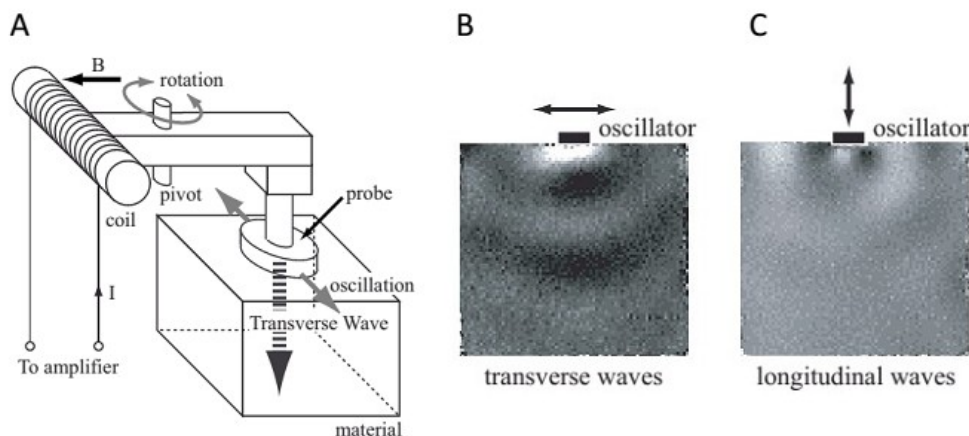


Figure 1.32: A: example of actuator, B-C: MRE of transverse and longitudinal strain waves. The wavelength of longitudinal strain waves is longer than that of transverse strain waves. (Oida et al., 2004).

Chen et al. (2005b) has developed an agarose phantom, placed in a head coil, with an electromechanical driver composed of a rod ($D=10$ mm) inserted in the phantom and tapped on the center of the surface. Then shear waves are propagated along a radial direction.

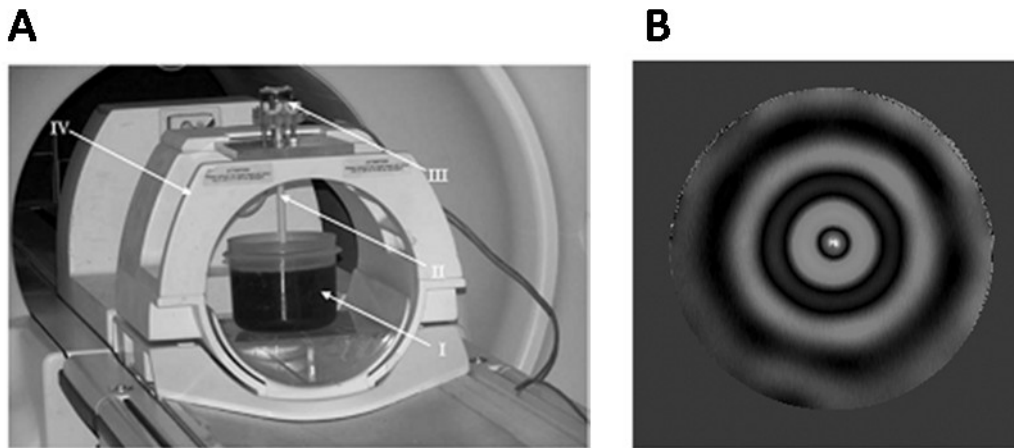


Figure 1.33: A: Setup of the MRE scan on an agarose gel phantom, B: A superior view of a MRE wave image for the cylindrical 2% agarose gel phantom at frequency of 150Hz.. I. Round gel phantom in a container, II. The applicator of the electromechanical driver. The diameter of the tip is 10 mm, III. The electromechanical driver which is phase-coupled with oscillating the motion sensitizing gradient, IV. Head coil (Chen et al., 2005b).

The study of Kolipaka et al. (2009) shows the acoustic driver system for generating motion in the phantom and the hydraulic system, including the computer-controlled flow pump, the pressure transducer for recording the in-line pressure and the plythsmograph for triggering the MRE pulse sequence.

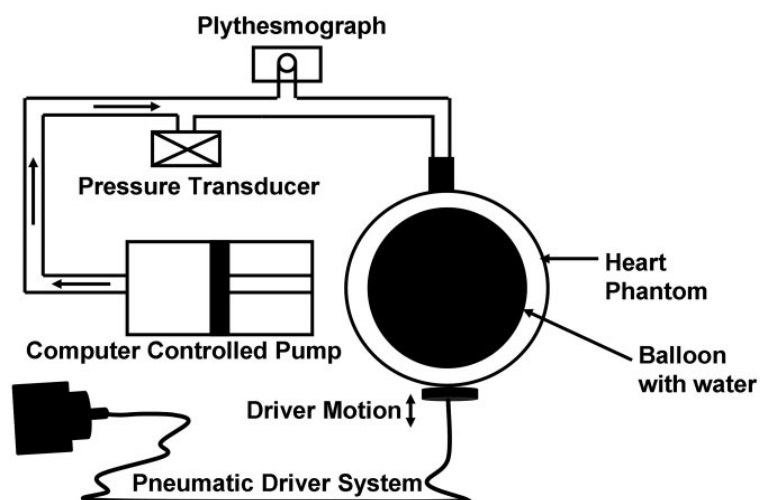


Figure 1.34: Experimental setup for MRE heart phantom (Kolipaka et al., 2009b)

Leclerc et al. (2012) and Debernard et al. (2012) have characterized the viscoelastic property of a plastic phantom mimicking the elastic properties of biological soft tissue using an abdominal pneumatic driver. The phantom was placed inside a head coil (Figure 1.35), resting around the pneumatic driver and connected to a large active loudspeaker to generate waves inside the phantom.

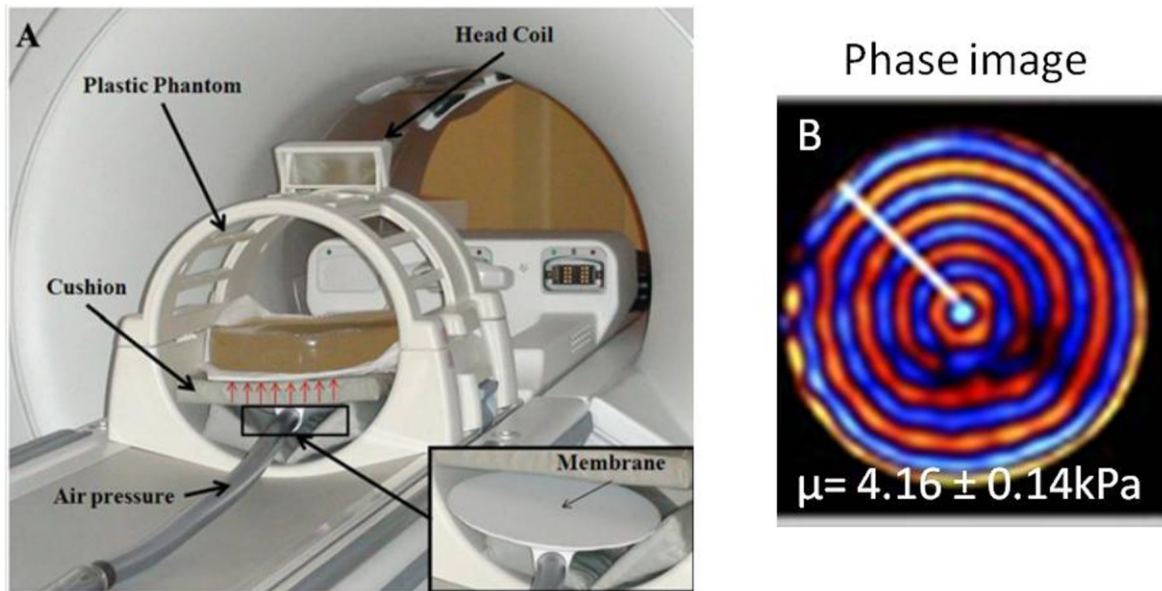


Figure 1.35: Magnetic Resonance Elastography (MRE) tests performed on a plastic phantom with a pneumatic driver (Leclerc et al., 2013b).

3. Mechanical properties

The table, hereafter, summarizes the mechanical properties of the phantoms in the literature.

Authors	phantoms	Frequencies	Different concentrations	μ (kPa)
Hamhaber et al., 2003	Agarose gel	125 Hz	0.5 %	4.5 ± 0.2 kPa
			1.0 %	16.8 ± 0.82 kPa
			1.5 %	35.3 ± 2.0 kPa
			2.0 %	57.3 ± 7.6 kPa
		250 Hz	0.5 %	4.7 ± 0.2 kPa
			1.0 %	15.0 ± 0.6 kPa
			1.5 %	35.0 ± 1.7 kPa
			2.0 %	57.9 ± 3.7 kPa
		400 Hz	0.5 %	4.3 ± 0.3 kPa
			1.0 %	15.1 ± 0.8 kPa
			2.0 %	55.0 ± 3.8 kPa
			200 Hz	2.0%
Ringleb et al., 2005		100 Hz	1.5 %	14.3 ± 1.3 kPa
			2.0 %	25.0 ± 0.2 kPa
		150 Hz	2.5 %	49.3 ± 1.4 kPa
			3.0 %	80.8 ± 1.6 kPa
		200 Hz	3.5 %	108.3 ± 4.4 kPa
Chen et al., 2007, 2008	Bovine gel	250 Hz	8%	13.5 ± 2.0 kPa
			18%	48.6 ± 10.8 kPa
Yin et al., 2008		90 Hz	15%	2.67 ± 0.06 kPa
Chen et al., 2006	Wirosil gel	300Hz		
	Test 1: Phantom (D=300mm and thickness = 25 mm)	350Hz		
	Test 2: Phantom (length = 160 mm, width = 25 mm and thickness = 25 mm)	400Hz		
		450Hz		
Papazoglou et al., 2012	Agar gel	30 Hz		
		40 Hz		
		50 Hz		
		60 Hz		
		70 Hz		
		80 Hz		
		90 Hz		
		100 Hz		
Leclerc et al., 2012	Mixture of softener and plastisol	60 Hz	55% of plastisol	3.34 kPa
		70 Hz	55% of plastisol	3.41 kPa
		80 Hz	55% of plastisol	3.44 kPa

Table 1-6: Elastic properties of the phantoms

References

- Abe, T., Brechue, W.F., Fujita, S., and Brown, J.B. (1998). Gender differences in FFM accumulation and architectural characteristics of muscle: *Med. Sci. Sports Exerc.* *30*, 1066–1070.
- Abe, T., Kumagai, K., and Brechue, W.F. (2000). Fascicle length of leg muscles is greater in sprinters than distance runners: *Med. Sci. Sports Exerc.* *32*, 1125–1129.
- Agache, P.G., Monneur, C., Leveque, J.L., and Rigal, J.D. (1980). Mechanical properties and Young's modulus of human skin in vivo. *Arch. Dermatol. Res.* *269*, 221–232.
- Amador, C., Urban, M., Chen, S., and Greenleaf, J. (2011). Shearwave dispersion ultrasound vibrometry (sdv) on swine kidney. *IEEE Trans. Ultrason. Ferroelectr. Freq. Control* *58*, 2608–2619.
- Anantawaraskul, S. (2005). *Polymer Analysis/Polymer Theory* (Springer Science & Business Media).
- Arampatzis, A., Mademli, L., De Monte, G., and Walsh, M. (2007). Changes in fascicle length from rest to maximal voluntary contraction affect the assessment of voluntary activation. *J. Biomech.* *40*, 3193–3200.
- Asbach, P., Klatt, D., Schlosser, B., Biermer, M., Muche, M., Rieger, A., Loddenkemper, C., Somasundaram, R., Berg, T., Hamm, B., et al. (2010). Viscoelasticity-based Staging of Hepatic Fibrosis with Multifrequency MR Elastography¹. *Radiology* *257*, 80–86.
- Atay, S.M., Kroenke, C.D., Sabet, A., and Bayly, P.V. (2008). Measurement of the Dynamic Shear Modulus of Mouse Brain Tissue In Vivo By Magnetic Resonance Elastography. *J. Biomech. Eng.* *130*, 021013.
- Axel, L., and Dougherty, L. (1989). Heart wall motion: improved method of spatial modulation of magnetization for MR imaging. *Radiology* *172*, 349–350.
- Baghani, A., Eskandari, H., Salcudean, S., and Rohling, R. (2009). Measurement of viscoelastic properties of tissue-mimicking material using longitudinal wave excitation. *IEEE Trans. Ultrason. Ferroelectr. Freq. Control* *56*, 1405–1418.
- Ballyns, J.J., Turo, D., Otto, P., Shah, J.P., Hammond, J., Gebreab, T., Gerber, L.H., and Sikdar, S. (2012). Office-Based Elastographic Technique for Quantifying Mechanical Properties of Skeletal Muscle. *J. Ultrasound Med.* *31*, 1209–1219.
- De la Barrera, E.J., and Milner, T.E. (1994). The effects of skinfold thickness on the selectivity of surface EMG. *Electroencephalogr. Clin. Neurophysiol. Potentials Sect.* *93*, 91–99.
- Basford, J.R., Jenkyn, T.R., An, K.-N., Ehman, R.L., Heers, G., and Kaufman, K.R. (2002). Evaluation of healthy and diseased muscle with magnetic resonance elastography. *Arch. Phys. Med. Rehabil.* *83*, 1530–1536.

- Basmajian, J., and De Luca, C. (1985). Chapter 3: Description and Analysis of EMG signal. *Muscles Alive Their Funct. Reveal. Electromyogr.* 65–100.
- Beers, B.E.V., Doblas, S., and Sinkus, R. (2011). New acquisition techniques: fields of application. *Abdom. Imaging* 37, 155–163.
- Beneke, R., Neuerburg, J., and Bohndorf, K. (1991). Muscle cross-section measurement by magnetic resonance imaging. *Eur. J. Appl. Physiol.* 63, 424–429.
- Bensamoun, S.F., Ringleb, S.I., Littrell, L., Chen, Q., Brennan, M., Ehman, R.L., and An, K.-N. (2006a). Determination of thigh muscle stiffness using magnetic resonance elastography. *J. Magn. Reson. Imaging* 23, 242–247.
- Bensamoun, S.F., Ringleb, S.I., Littrell, L., Chen, Q., Brennan, M., Ehman, R.L., and An, K.-N. (2006b). Determination of thigh muscle stiffness using magnetic resonance elastography. *J. Magn. Reson. Imaging* 23, 242–247.
- Bensamoun, S.F., Ringleb, S.I., Chen, Q., Ehman, R.L., An, K.-N., and Brennan, M. (2007). Thigh muscle stiffness assessed with magnetic resonance elastography in hyperthyroid patients before and after medical treatment. *J. Magn. Reson. Imaging* 26, 708–713.
- Bensamoun, S.F., Wang, L., Robert, L., Charleux, F., Latrive, J.-P., and Ho Ba Tho, M.-C. (2008a). Measurement of liver stiffness with two imaging techniques: Magnetic resonance elastography and ultrasound elastometry. *J. Magn. Reson. Imaging* 28, 1287–1292.
- Bensamoun, S.F., Glaser, K.J., Ringleb, S.I., Chen, Q., Ehman, R.L., and An, K.-N. (2008b). Rapid magnetic resonance elastography of muscle using one-dimensional projection. *J. Magn. Reson. Imaging* 27, 1083–1088.
- Bensamoun, S.F., Robert, L., Leclerc, G.E., Debernard, L., and Charleux, F. (2011a). Stiffness imaging of the kidney and adjacent abdominal tissues measured simultaneously using magnetic resonance elastography. *Clin. Imaging* 35, 284–287.
- Bensamoun, S.F., Robert, L., Leclerc, G.E., Debernard, L., and Charleux, F. (2011b). Stiffness imaging of the kidney and adjacent abdominal tissues measured simultaneously using magnetic resonance elastography. *Clin. Imaging* 35, 284–287.
- Bensamoun S. F., Charleux F., and Themar-Noel C. (2014). Elastic properties of skeletal muscle and subcutaneous tissues in Duchenne muscular dystrophy by magnetic resonance elastography (MRE): a feasibility study. *Innov. Res. Biomed. Eng. IRBM.*
- Bercoff, J., Chaffai, S., Tanter, M., Sandrin, L., Catheline, S., Fink, M., Gennisson, J.L., and Meunier, M. (2003). In vivo breast tumor detection using transient elastography. *Ultrasound Med. Biol.* 29, 1387–1396.
- Best, T.M., McElhaney, J., Garrett Jr, W.E., and Myers, B.S. (1994). Characterization of the passive responses of live skeletal muscle using the quasi-linear theory of viscoelasticity. *J. Biomech.* 27, 413–419.
- Bizzini, M., and Mannion, A.F. (2003). Reliability of a new, hand-held device for assessing skeletal muscle stiffness. *Clin. Biomech.* 18, 459–461.

- Blemker, S.S., Pinsky, P.M., and Delp, S.L. (2005). A 3D model of muscle reveals the causes of nonuniform strains in the biceps brachii. *J. Biomech.* *38*, 657–665.
- Bonnel, F., Marc, T., and Abid, A. (2009). *Le muscle: nouveaux concepts: anatomie, biomécanique, chirurgie, rééducation* (Saurecamps Médicals).
- Bouisset, S., and Maton, B. (1995). *Muscle, posture et mouvement: bases et applications de la méthode électromyographique*. Hermann Paris.
- Brauck, K., Galban, C.J., Maderwald, S., Herrmann, B.L., and Ladd, M.E. (2007). Changes in calf muscle elasticity in hypogonadal males before and after testosterone substitution as monitored by magnetic resonance elastography. *Eur. J. Endocrinol.* *156*, 673–678.
- Brechue, W.F., and Abe, T. (2014). The role of FFM accumulation and skeletal muscle architecture in powerlifting performance. *Eur. J. Appl. Physiol.* *86*, 327–336.
- Brooke, M.H., and Kaiser, K.K. (1970). THREE “MYOSIN ADENOSINE TRIPHOSPHATASE” SYSTEMS: THE NATURE OF THEIR pH LABILITY AND SULFHYDRYL DEPENDENCE. *J. Histochem. Cytochem.* *18*, 670–672.
- Brooke MH, and Kaiser KK (1970). Muscle fiber types: How many and what kind? *Arch. Neurol.* *23*, 369–379.
- Callaghan, P.T., and Stepišnik, J. (1995). Frequency-domain analysis of spin motion using modulated-gradient NMR. *J. Magn. Reson. A* *117*, 118–122.
- Carter, F.J., Frank, T.G., Davies, P.J., McLean, D., and Cuschieri, A. (2001). Measurements and modelling of the compliance of human and porcine organs. *Med. Image Anal.* *5*, 231–236.
- Castera, L., Forns, X., and Alberti, A. (2008). Non-invasive evaluation of liver fibrosis using transient elastography. *J. Hepatol.* *48*, 835–847.
- Catheline, S. (1998). INTERFEROMETRIE-SPECKLE ULTRASONORE : APPLICATION A LA MESURE D’ELASTICITE. phdthesis. Université Paris-Diderot - Paris VII.
- Catheline, S., Thomas, J.-L., Wu, F., and Fink, M.A. (1999). Diffraction field of a low frequency vibrator in soft tissues using transient elastography. *IEEE Trans. Ultrason. Ferroelectr. Freq. Control* *46*, 1013–1019.
- Catheline, S., Gennisson, J.-L., and Fink, M. (2003). Measurement of elastic nonlinearity of soft solid with transient elastography. *J. Acoust. Soc. Am.* *114*, 3087–3091.
- Catheline, S., Gennisson, J.-L., Delon, G., Fink, M., Sinkus, R., Abouelkaram, S., and Culioli, J. (2004). Measurement of viscoelastic properties of homogeneous soft solid using transient elastography: An inverse problem approach. *J. Acoust. Soc. Am.* *116*, 3734–3741.
- Chakouch, M.K., Charleux, F., and Bensamoun, S.F. (2014). New magnetic resonance elastography protocols to characterise deep back and thigh muscles. *Comput. Methods Biomech. Biomed. Engin.* *17 Suppl 1*, 32–33.

- Chapman, A. (2004). *England's Leonardo: Robert Hooke and the Seventeenth-Century Scientific Revolution* (CRC Press).
- Chen, Q., Ringleb, S.I., Hulshizer, T., and An, K.-N. (2005a). Identification of the testing parameters in high frequency dynamic shear measurement on agarose gels. *J. Biomech.* *38*, 959–963.
- Chen, Q., Ringleb, S.I., Manduca, A., Ehman, R.L., and An, K.-N. (2005b). A finite element model for analyzing shear wave propagation observed in magnetic resonance elastography. *J. Biomech.* *38*, 2198–2203.
- Chen, Q., Ringleb, S.I., Manduca, A., Ehman, R.L., and An, K.-N. (2006). Differential effects of pre-tension on shear wave propagation in elastic media with different boundary conditions as measured by magnetic resonance elastography and finite element modeling. *J. Biomech.* *39*, 1428–1434.
- Chen, Q., Bensamoun, S., Basford, J.R., Thompson, J.M., and An, K.-N. (2007). Identification and Quantification of Myofascial Taut Bands With Magnetic Resonance Elastography. *Arch. Phys. Med. Rehabil.* *88*, 1658–1661.
- Chen, Q., Basford, J., and An, K.-N. (2008). Ability of magnetic resonance elastography to assess taut bands. *Clin. Biomech.* *23*, 623–629.
- Chen, S., Fatemi, M., and Greenleaf, J.F. (2004). Quantifying elasticity and viscosity from measurement of shear wave speed dispersion. *J. Acoust. Soc. Am.* *115*, 2781–2785.
- Chen, S., Urban, M.W., Pislaru, C., Kinnick, R., Zheng, Y., Yao, A., and Greenleaf, J.F. (2009). Shearwave dispersion ultrasound vibrometry (SDUV) for measuring tissue elasticity and viscosity. *IEEE Trans. Ultrason. Ferroelectr. Freq. Control* *56*, 55–62.
- Choi, Y.M., and Kim, B.C. (2009). Muscle fiber characteristics, myofibrillar protein isoforms, and meat quality. *Livest. Sci.* *122*, 105–118.
- Chow, R.S., Medri, M.K., Martin, D.C., Leekam, R.N., Agur, A.M., and McKee, N.H. (2000). Sonographic studies of human soleus and gastrocnemius muscle architecture: gender variability. *Eur. J. Appl. Physiol.* *82*, 236–244.
- Debernard, L., Robert, L., Charleux, F., and Bensamoun, S.F. (2011a). Characterization of muscle architecture in children and adults using magnetic resonance elastography and ultrasound techniques. *J. Biomech.* *44*, 397–401.
- Debernard, L., Robert, L., Charleux, F., and Bensamoun, S.F. (2011b). Analysis of thigh muscle stiffness from childhood to adulthood using magnetic resonance elastography (MRE) technique. *Clin. Biomech.* *26*, 836–840.
- Debernard, L., Leclerc, G.E., Robert, L., Charleux, F., and Bensamoun, S.F. (2013). In vivo characterization of the muscle viscoelasticity in passive and active conditions using multifrequency mr elastography. *J. Musculoskelet. Res.* *16*, 1350008.

- Deffieux, T., Montaldo, G., Tanter, M., and Fink, M. (2009). Shear Wave Spectroscopy for In Vivo Quantification of Human Soft Tissues Visco-Elasticity. *IEEE Trans. Med. Imaging* 28, 313–322.
- Denk, W., Keolian, R.M., Ogawa, S., and Jelinski, L.W. (1993). Oscillatory flow in the cochlea visualized by a magnetic resonance imaging technique. *Proc. Natl. Acad. Sci.* 90, 1595–1598.
- Domire, Z.J., McCullough, M.B., Chen, Q., and An, K.-N. (2009). Wave attenuation as a measure of muscle quality as measured by magnetic resonance elastography: Initial results. *J. Biomech.* 42, 537–540.
- Dresner, M.A., Rose, G.H., Rossman, P.J., Muthupillai, R., Manduca, A., and Ehman, R.L. (2001). Magnetic resonance elastography of skeletal muscle. *J. Magn. Reson. Imaging* 13, 269–276.
- Duggan, T. (1967). Dynamic mechanical testing of living tissue.
- Ehman, R.L., Rossman, P.J., Hulshizer, T.C., and Dresner, M.A. (2006). Pressure activated driver for magnetic resonance elastography.
- Elgeti, T., Beling, M., Hamm, B., Braun, J., and Sack, I. (2010). Cardiac Magnetic Resonance Elastography: Toward the Diagnosis of Abnormal Myocardial Relaxation. *Invest. Radiol.* 45, 782–787.
- Evans, J. (1965). The mechanical characteristics of human skin.
- Farina, D., Merletti, R., and Enoka, R.M. (2004). The extraction of neural strategies from the surface EMG. *J. Appl. Physiol.* 96, 1486–1495.
- Feinstein, B., Lindegård, B., Nyman, E., and Wohlfart, G. (1955). MORPHOLOGIC STUDIES OF MOTOR UNITS IN NORMAL HUMAN MUSCLES. *Cells Tissues Organs* 23, 127–142.
- Foucher, J., Chanteloup, E., Vergniol, J., Castéra, L., Bail, B.L., Adhoute, X., Bertet, J., Couzigou, P., and Lédinghen, V. de (2006). Diagnosis of cirrhosis by transient elastography (FibroScan): a prospective study. *Gut* 55, 403–408.
- Fowlkes, J.B., Emelianov, S.Y., Pipe, J.G., Skovoroda, A.R., Carson, P.L., Adler, R.S., and Sarvazyan, A.P. (1995). Magnetic-resonance imaging techniques for detection of elasticity variation. *Med. Phys.* 22, 1771–1778.
- Friedrich–Rust, M., Ong, M., Martens, S., Sarrazin, C., Bojunga, J., Zeuzem, S., and Herrmann, E. (2008). Performance of Transient Elastography for the Staging of Liver Fibrosis: A Meta-Analysis. *Gastroenterology* 134, 960–974.e8.
- Froeling, M., Nederveen, A.J., Heijtel, D.F.R., Lataster, A., Bos, C., Nicolay, K., Maas, M., Drost, M.R., and Strijkers, G.J. (2012). Diffusion-tensor MRI reveals the complex muscle architecture of the human forearm. *J. Magn. Reson. Imaging* 36, 237–248.

Fukunaga, T., Funato, K., and Sikegawa, H. (1992). The Effects of Resistance Training on Muscle Area and Strength in Prepubescent Age. *Ann. Physiol. Anthropol.* *11*, 357–364.

Fukunaga, T., Ichinose, Y., Ito, M., Kawakami, Y., and Fukashiro, S. (1997a). Determination of fascicle length and pennation in a contracting human muscle in vivo. *J. Appl. Physiol.* *82*, 354–358.

Fukunaga, T., Kawakami, Y., Kuno, S., Funato, K., and Fukashiro, S. (1997b). Muscle architecture and function in humans. *J. Biomech.* *30*, 457–463.

Fukunaga, T., Miyatani, M., Tachi, M., Kouzaki, M., Kawakami, Y., and Kanehisa, H. (2001). Muscle volume is a major determinant of joint torque in humans. *Acta Physiol. Scand.* *172*, 249–255.

Fung, Y.C., and Cowin, S.C. (1994). *Biomechanics: Mechanical Properties of Living Tissues*, 2nd ed. *J. Appl. Mech.* *61*, 1007.

Gao, L., Parker, K.J., Lerner, R.M., and Levinson, S.F. (1996). Imaging of the elastic properties of tissue—A review. *Ultrasound Med. Biol.* *22*, 959–977.

Gao, Z., Lister, K., and Desai, J.P. (2009). Constitutive Modeling of Liver Tissue: Experiment and Theory. *Ann. Biomed. Eng.* *38*, 505–516.

Gapeyeva, H., and Vain, A. (2008). *Methodical guide: principles of applying Myoton in physical medicine and rehabilitation*. Est. Muomeetria Ltd.

Garteiser, P., Sahebjavaher, R.S., Ter Beek, L.C., Salcudean, S., Vilgrain, V., Van Beers, B.E., and Sinkus, R. (2013). Rapid acquisition of multifrequency, multislice and multidirectional MR elastography data with a fractionally encoded gradient echo sequence. *NMR Biomed.* n/a – n/a.

Gefen, A., Gefen, N., Linder-Ganz, E., and Margulies, S.S. (2005). In Vivo Muscle Stiffening Under Bone Compression Promotes Deep Pressure Sores. *J. Biomech. Eng.* *127*, 512–524.

GENNISSON, M.J.-L. (2004). *Le palpeur acoustique: un nouvel outil d'investigation des tissus biologiques*. UNIVERSITE PARIS 6.

Gennisson, J.-L., Catheline, S., Chaffai, S., and Fink, M. (2003). Transient elastography in anisotropic medium: Application to the measurement of slow and fast shear wave speeds in muscles. *J. Acoust. Soc. Am.* *114*, 536–541.

Gennisson, J.L., Cornu, C., Catheline, S., Fink, M., and Portero, P. (2005). Human muscle hardness assessment during incremental isometric contraction using transient elastography. *J. Biomech.* *38*, 1543–1550.

Gennisson, J.-L., Deffieux, T., Macé, E., Montaldo, G., Fink, M., and Tanter, M. (2010). Viscoelastic and Anisotropic Mechanical Properties of in vivo Muscle Tissue Assessed by Supersonic Shear Imaging. *Ultrasound Med. Biol.* *36*, 789–801.

Gennisson, J.-L., Deffieux, T., Fink, M., and Tanter, M. (2013). *Ultrasound elastography: Principles and techniques*. *Diagn. Interv. Imaging* *94*, 487–495.

Goubel, F., and Linsel-Corbeil, G. (2003). *Biomécanique: éléments de mécanique musculaire* (Masson).

Grahame, R. (1969). Elasticity of Human Skin in Vivo a Study of the Physical Properties of the Skin in Rheumatoid Arthritis and the Effect of Corticosteroids. *Rheumatology* *10*, 130–136.

Gray, H., 1825-1861, Lewis, W.H., 1870-1964, Gray, H., and 1825-1861 (1924). *Anatomy of the human body*.

Green, M.A., Bilston, L.E., and Sinkus, R. (2008). In vivo brain viscoelastic properties measured by magnetic resonance elastography. *NMR Biomed.* *21*, 755–764.

Green, M.A., Sinkus, R., Gandevia, S.C., Herbert, R.D., and Bilston, L.E. (2012). Measuring changes in muscle stiffness after eccentric exercise using elastography. *NMR Biomed.* *25*, 852–858.

Green, M.A., Geng, G., Qin, E., Sinkus, R., Gandevia, S.C., and Bilston, L.E. (2013a). Measuring anisotropic muscle stiffness properties using elastography. *NMR Biomed.* n/a – n/a.

Green, M.A., Geng, G., Qin, E., Sinkus, R., Gandevia, S.C., and Bilston, L.E. (2013b). Measuring anisotropic muscle stiffness properties using elastography. *NMR Biomed.* n/a – n/a.

Hadj Henni, A., Schmitt, C., Tremblay, M.-É., Hamdine, M., Heuzey, M.-C., Carreau, P., and Cloutier, G. (2011). Hyper-frequency viscoelastic spectroscopy of biomaterials. *J. Mech. Behav. Biomed. Mater.* *4*, 1115–1122.

Hamhaber, U., Grieshaber, F. a., Nagel, J. h., and Klose, U. (2003). Comparison of quantitative shear wave MR-elastography with mechanical compression tests. *Magn. Reson. Med.* *49*, 71–77.

Heckmatt, J.Z., Pier, N., and Dubowitz, V. (1988a). Measurement of quadriceps muscle thickness and subcutaneous tissue thickness in normal children by real-time ultrasound imaging. *J. Clin. Ultrasound* *16*, 171–176.

Heckmatt, J.Z., Pier, N., and Dubowitz, V. (1988b). Assessment of quadriceps femoris muscle atrophy and hypertrophy in neuromuscular disease in children. *J. Clin. Ultrasound* *16*, 177–181.

Heers, G., Jenkyn, T., Alex Dresner, M., Klein, M.-O., R Basford, J., R Kaufman, K., L Ehman, R., and An, K.-N. (2003). Measurement of muscle activity with magnetic resonance elastography. *Clin. Biomech.* *18*, 537–542.

Henriksson-Larsen, K., Wretling, M.-L., Lorentzon, R., and Öberg, L. (1992). Do muscle fibre size and fibre angulation correlate in pennated human muscles? *Eur. J. Appl. Physiol.* *64*, 68–72.

Hill, A. (1922). The mechanism of muscular contraction. *Physiol Rev* *2*, 310.

- Hodges, P.W., Pengel, L.H.M., Herbert, R.D., and Gandevia, S.C. (2003). Measurement of muscle contraction with ultrasound imaging. *Muscle Nerve* 27, 682–692.
- Hogrel, J.-Y. (2005). Clinical applications of surface electromyography in neuromuscular disorders. *Neurophysiol. Clin. Neurophysiol.* 35, 59–71.
- Hollenstein, M., Nava, A., Valtorta, D., Snedeker, J.G., and Mazza, E. (2006). Mechanical Characterization of the Liver Capsule and Parenchyma. In *Biomedical Simulation*, M. Harders, and G. Székely, eds. (Springer Berlin Heidelberg), pp. 150–158.
- Houten, E.E.W.V., Weaver, J.B., Miga, M.I., Kennedy, F.E., and Paulsen, K.D. (2000). Elasticity reconstruction from experimental MR displacement data: initial experience with an overlapping subzone finite element inversion process. *Med. Phys.* 27, 101–107.
- Hsieh, C.Y., Hong, C.Z., Adams, A.H., Platt, K.J., Danielson, C.D., Hoehler, F.K., and Tobis, J.S. (2000). Interexaminer reliability of the palpation of trigger points in the trunk and lower limb muscles. *Arch. Phys. Med. Rehabil.* 81, 258–264.
- Huwart, L., Sempoux, C., Vicaut, E., Salameh, N., Annet, L., Danse, E., Peeters, F., ter Beek, L.C., Rahier, J., Sinkus, R., et al. (2008). Magnetic Resonance Elastography for the Noninvasive Staging of Liver Fibrosis. *Gastroenterology* 135, 32–40.
- Huxley, A.F., and Simmons, R.M. (1971). Mechanical properties of the cross-bridges of frog striated muscle. *J. Physiol.* 218 *Suppl.*, 59P – 60P.
- Huxley, A.F., and Taylor, R.E. (1958). Local activation of striated muscle fibres. *J. Physiol.* 144, 426–441.
- Ichinose, Y., Kawakami, Y., Ito, M., and Fukunaga, T. (1997). Estimation of Active Force-Length Characteristics of Human Vastus lateralis Muscle. *Cells Tissues Organs* 159, 78–83.
- Ieva, A.D., Grizzi, F., Rognone, E., Tse, Z.T.H., Parittotokkaporn, T., Baena, F.R. y, Tschabitscher, M., Matula, C., Trattng, S., and Baena, R.R. y (2010). Magnetic resonance elastography: a general overview of its current and future applications in brain imaging. *Neurosurg. Rev.* 33, 137–145.
- Jenkyn, T.R., Ehman, R.L., and An, K.-N. (2003). Noninvasive muscle tension measurement using the novel technique of magnetic resonance elastography (MRE). *J. Biomech.* 36, 1917–1921.
- JOHANSSON, T., MEIER, P., and BLICKHAN, R. (2000). A Finite-Element Model for the Mechanical Analysis of Skeletal Muscles. *J. Theor. Biol.* 206, 131–149.
- Kanai, H. (2005). Propagation of spontaneously actuated pulsive vibration in human heart wall and in vivo viscoelasticity estimation. *IEEE Trans. Ultrason. Ferroelectr. Freq. Control* 52, 1931–1942.
- Kawakami, Y., Abe, T., and Fukunaga, T. (1993). Muscle-fiber pennation angles are greater in hypertrophied than in normal muscles. *J. Appl. Physiol.* 74, 2740–2744.

- Klatt, D., Friedrich, C., Korth, Y., Vogt, R., Braun, J., and Sack, I. (2010a). Viscoelastic properties of liver measured by oscillatory rheometry and multifrequency magnetic resonance elastography. *Biorheology* *47*, 133–141.
- Klatt, D., Papazoglou, S., Braun, J., and Sack, I. (2010b). Viscoelasticity-based MR elastography of skeletal muscle. *Phys. Med. Biol.* *55*, 6445–6459.
- Kolipaka, A., McGee, K.P., Manduca, A., Romano, A.J., Glaser, K.J., Araoz, P.A., and Ehman, R.L. (2009a). Magnetic resonance elastography: Inversions in bounded media. *Magn. Reson. Med.* *62*, 1533–1542.
- Kolipaka, A., McGee, K.P., Araoz, P.A., Glaser, K.J., Manduca, A., and Ehman, R.L. (2009b). Evaluation of a rapid, multiphase MRE sequence in a heart-simulating phantom. *Magn. Reson. Med.* *62*, 691–698.
- Krouskop, T.A., Wheeler, T.M., Kallel, F., Garra, B.S., and Hall, T. (1998). Elastic Moduli of Breast and Prostate Tissues under Compression. *Ultrason. Imaging* *20*, 260–274.
- Kruse, S.A., Smith, J.A., Lawrence, A.J., Dresner, M.A., Manduca, A., Greenleaf, J.F., Ehman, R.L., Kruse, S.A., Smith, J.A., Lawrence, A.J., et al. (2000). Tissue characterization using magnetic resonance elastography: preliminary results. *Phys. Med. Biol.* *45*, 1579.
- Kruse, S.A., Rose, G.H., Glaser, K.J., Manduca, A., Felmlee, J.P., Jack Jr., C.R., and Ehman, R.L. (2008). Magnetic resonance elastography of the brain. *NeuroImage* *39*, 231–237.
- Kubo, K., Kanehisa, H., Azuma, K., Ishizu, M., Kuno, S.-Y., Okada, M., and Fukunaga, T. (2003). Muscle Architectural Characteristics in Women Aged 20–79 Years: *Med. Sci. Sports Exerc.* *35*, 39–44.
- Leclerc, G.E., Debernard, L., Foucart, F., Robert, L., Pelletier, K.M., Charleux, F., Ehman, R., Ho Ba Tho, M.-C., and Bensamoun, S.F. (2012). Characterization of a hyper-viscoelastic phantom mimicking biological soft tissue using an abdominal pneumatic driver with magnetic resonance elastography (MRE). *J. Biomech.* *45*, 952–957.
- Leclerc, G.E., Charleux, F., Robert, L., Ho Ba Tho, M.-C., Rhein, C., Latrive, J.-P., and Bensamoun, S.F. (2013a). Analysis of liver viscosity behavior as a function of multifrequency magnetic resonance elastography (MMRE) postprocessing. *J. Magn. Reson. Imaging* n/a – n/a.
- Leclerc, G.E., Charleux, F., Ho Ba Tho, M.-C., and Bensamoun, S.F. (2013b). Identification process based on shear wave propagation within a phantom using finite element modelling and magnetic resonance elastography. *Comput. Methods Biomech. Biomed. Engin.* 1–7.
- Levin, A., and Wyman, J. (1927). The Viscous Elastic Properties of Muscle. *Proc. R. Soc. Lond. Ser. B Contain. Pap. Biol. Character* *101*, 218–243.
- Lew, P.C., Lewis, J., and Story, I. (1997). Inter-therapist reliability in locating latent myofascial trigger points using palpation. *Man. Ther.* *2*, 87–90.

- Li, B.N., Chui, C.K., Ong, S.H., Numano, T., Washio, T., Homma, K., Chang, S., Venkatesh, S., and Kobayashi, E. (2012). Modeling shear modulus distribution in magnetic resonance elastography with piecewise constant level sets. *Magn. Reson. Imaging* 30, 390–401.
- Li, K., Dortch, R.D., Welch, E.B., Bryant, N.D., Buck, A.K.W., Towse, T.F., Gochberg, D.F., Does, M.D., Damon, B.M., and Park, J.H. (2014). Multi-parametric MRI characterization of healthy human thigh muscles at 3.0 T – relaxation, magnetization transfer, fat/water, and diffusion tensor imaging. *NMR Biomed.* 27, 1070–1084.
- Lindberg, F. (2013). Ultrasonic Quantification of Skeletal Muscle Dynamics: Feasibility and Limitations.
- Van Loocke, M., Simms, C.K., and Lyons, C.G. (2009). Viscoelastic properties of passive skeletal muscle in compression—Cyclic behaviour. *J. Biomech.* 42, 1038–1048.
- Lopez, O., Amrami, K.K., Manduca, A., and Ehman, R.L. (2008). Characterization of the dynamic shear properties of hyaline cartilage using high-frequency dynamic MR elastography. *Magn. Reson. Med.* 59, 356–364.
- De Luca, C.J. (1997). The use of surface electromyography in biomechanics. *J. Appl. Biomech.* 13, 135–163.
- Lund, H., Christensen, L., Savnik, A., Boesen, J., Danneskiold-Samsøe, B., and Bliddal, H. (2002). Volume estimation of extensor muscles of the lower leg based on MR imaging. *Eur. Radiol.* 12, 2982–2987.
- Luo, B., Yang, R., Ying, P., Awad, M., Choti, M., and Taylor, R. (2006). Elasticity and Echogenicity Analysis of Agarose Phantoms Mimicking Liver Tumors. In *Bioengineering Conference, 2006. Proceedings of the IEEE 32nd Annual Northeast*, pp. 81–82.
- MacCallum, J.B. (1898). On the histogenesis of the striated muscle fibre, and the growth of the human sartorius muscle. *Johns Hopkins Hosp Bull* 9, 208.
- Manduca, A., Muthupillai, R., Rossman, P.J., Greenleaf, J.F., and Ehman, R.L. (1996a). Local wavelength estimation for magnetic resonance elastography. In *International Conference on Image Processing, 1996. Proceedings*, pp. 527–530 vol.3.
- Manduca, A., Muthupillai, R., Rossman, P.J., Greenleaf, J.F., and Ehman, R.L. (1996b). Image processing for magnetic-resonance elastography. pp. 616–623.
- Manduca, A., Oliphant, T.E., Dresner, M.A., Mahowald, J.L., Kruse, S.A., Amromin, E., Felmlee, J.P., Greenleaf, J.F., and Ehman, R.L. (2001). Magnetic resonance elastography: non-invasive mapping of tissue elasticity. *Med. Image Anal.* 5, 237–254.
- Manduca, A., Lake, D.S., Kruse, S.A., and Ehman, R.L. (2003). Spatio-temporal directional filtering for improved inversion of MR elastography images. *Med. Image Anal.* 7, 465–473.
- Mannelli, L., Godfrey, E., Joubert, I., Patterson, A.J., Graves, M.J., Gallagher, F.A., and Lomas, D.J. (2010). MR Elastography: Spleen Stiffness Measurements in Healthy Volunteers—Preliminary Experience. *Am. J. Roentgenol.* 195, 387–392.

Mariappan, Y.K., Glaser, K.J., Manduca, A., Romano, A.J., Venkatesh, S.K., Yin, M., and Ehman, R.L. (2009a). High-frequency mode conversion technique for stiff lesion detection with magnetic resonance elastography (MRE). *Magn. Reson. Med.* *62*, 1457–1465.

Mariappan, Y.K., Rossman, P.J., Glaser, K.J., Manduca, A., and Ehman, R.L. (2009b). Magnetic resonance elastography with a phased-array acoustic driver system. *Magn. Reson. Med.* *61*, 678–685.

Mariappan, Y.K., Glaser, K.J., Hubmayr, R.D., Manduca, A., Ehman, R.L., and McGee, K.P. (2011). MR elastography of human lung parenchyma: Technical development, theoretical modeling and in vivo validation. *J. Magn. Reson. Imaging* *33*, 1351–1361.

Marieb, E., and Hoehn, K. (2014). *Anatomie et physiologie humaines: Livre + eText + plateforme numérique MonLab - Licence étudiant 60 mois* (Pearson Education France).

Martins, J.A.C., Pires, E.B., Salvado, R., and Dinis, P.B. (1998). A numerical model of passive and active behavior of skeletal muscles. *Comput. Methods Appl. Mech. Eng.* *151*, 419–433.

Maurits, N.M., Beenakker, E.A.C., van Schaik, D.E.C., Fock, J.M., and van der Hoeven, J.H. (2004). Muscle ultrasound in children: Normal values and application to neuromuscular disorders. *Ultrasound Med. Biol.* *30*, 1017–1027.

McCullough, M.B., Domire, Z.J., Reed, A.M., Amin, S., Ytterberg, S.R., Chen, Q., and An, K.-N. (2011). Evaluation of muscles affected by myositis using magnetic resonance elastography. *Muscle Nerve* *43*, 585–590.

McGee, K.P., Hubmayr, R.D., and Ehman, R. I. (2008). MR elastography of the lung with hyperpolarized ³He. *Magn. Reson. Med.* *59*, 14–18.

Men, Y., Young, A., Stokes, M., and Crowe, M. (1985). The size and strength of the quadriceps muscles of old. *Clin. Physiol.* *5*, 145–154.

Merletti, R., Botter, A., Troiano, A., Merlo, E., and Minetto, M.A. (2009). Technology and instrumentation for detection and conditioning of the surface electromyographic signal: State of the art. *Clin. Biomech.* *24*, 122–134.

Miller, K. (2000). Constitutive modelling of abdominal organs. *J. Biomech.* *33*, 367–373.

Miller, K., and Chinzei, K. (1997). Constitutive modelling of brain tissue: Experiment and theory. *J. Biomech.* *30*, 1115–1121.

Morse, C.I., Degens, H., and Jones, D.A. (2007). The validity of estimating quadriceps volume from single MRI cross-sections in young men. *Eur. J. Appl. Physiol.* *100*, 267–274.

Murphy, M.C., Huston, J., Jack, C.R., Glaser, K.J., Manduca, A., Felmlee, J.P., and Ehman, R.L. (2011). Decreased brain stiffness in Alzheimer’s disease determined by magnetic resonance elastography. *J. Magn. Reson. Imaging* *34*, 494–498.

Murphy, M.C., Curran, G.L., Glaser, K.J., Rossman, P.J., Huston III, J., Poduslo, J.F., Jack Jr., C.R., Felmlee, J.P., and Ehman, R.L. (2012). Magnetic resonance elastography of the

brain in a mouse model of Alzheimer's disease: initial results. *Magn. Reson. Imaging* 30, 535–539.

Muthupillai, R., Lomas, D., Rossman, P., Greenleaf, J., Manduca, A., and Ehman, R. (1995). Magnetic resonance elastography by direct visualization of propagating acoustic strain waves. *Science* 269, 1854–1857.

Muthupillai, R., Rossman, P.J., Lomas, D.J., Greenleaf, J.F., Riederer, S.J., and Ehman, R.L. (1996). Magnetic resonance imaging of transverse acoustic strain waves. *Magn. Reson. Med.* 36, 266–274.

Myers, B.S., Ee, C.A.V., Camacho, D.L.A., Woolley, C.T., and Best, T.M. (1995). *On the Structural and Material Properties of Mammalian Skeletal Muscle and Its Relevance to Human Cervical Impact Dynamics* (Warrendale, PA: SAE International).

Myers, B.S., Woolley, C.T., Slotter, T.L., Garrett, W.E., and Best, T.M. (1998). The Influence of Strain Rate on the Passive and Stimulated Engineering Stress–Large Strain Behavior of the Rabbit Tibialis Anterior Muscle. *J. Biomech. Eng.* 120, 126–132.

Namani, R., Wood, M.D., Sakiyama-Elbert, S.E., and Bayly, P.V. (2009). Anisotropic mechanical properties of magnetically aligned fibrin gels measured by magnetic resonance elastography. *J. Biomech.* 42, 2047–2053.

Niitsu, M., Michizaki, A., Endo, A., Takei, H., and Yanagisawa, O. (2011). Muscle hardness measurement by using ultrasound elastography: a feasibility study. *Acta Radiol.* 52, 99–105.

Nordez, A., Gennisson, J.L., Casari, P., Catheline, S., and Cornu, C. (2008). Characterization of muscle belly elastic properties during passive stretching using transient elastography. *J. Biomech.* 41, 2305–2311.

Nordez, A., Guével, A., Casari, P., Catheline, S., and Cornu, C. (2009). Assessment of muscle hardness changes induced by a submaximal fatiguing isometric contraction. *J. Electromyogr. Kinesiol.* 19, 484–491.

Normand, V., Lootens, D.L., Amici, E., Plucknett, K.P., and Aymard, P. (2000). New Insight into Agarose Gel Mechanical Properties. *Biomacromolecules* 1, 730–738.

Oida, T., Amano, A., and Matsuda, T. (2004). Magnetic resonance elastography: in vivo measurements of elasticity for human tissue. In *International Conference on Informatics Research for Development of Knowledge Society Infrastructure, 2004. ICKS 2004*, pp. 57–64.

Okamoto, R.J., Clayton, E.H., and Bayly, P.V. (2011). Viscoelastic properties of soft gels: comparison of magnetic resonance elastography and dynamic shear testing in the shear wave regime. *Phys. Med. Biol.* 56, 6379–6400.

Oliphant, T.E., Mahowald, J.L., Ehman, R.L., and Greenleaf, J.F. (1999). Complex-valued quantitative stiffness estimation using dynamic displacement measurements and local inversion of conservation of momentum. In *1999 IEEE Ultrasonics Symposium, 1999. Proceedings*, pp. 1641–1644 vol.2.

- Oliphant, T.E., Manduca, A., Ehman, R.L., and Greenleaf, J.F. (2001). Complex-valued stiffness reconstruction for magnetic resonance elastography by algebraic inversion of the differential equation. *Magn. Reson. Med.* *45*, 299–310.
- Oomens, C.W.J., Maenhout, M., Oijen, C.H. van, Drost, M.R., and Baaijens, F.P. (2003). Finite element modelling of contracting skeletal muscle. *Philos. Trans. R. Soc. Lond. B Biol. Sci.* *358*, 1453–1460.
- Ophir, J., Céspedes, I., Ponnekanti, H., Yazdi, Y., and Li, X. (1991). Elastography: A Quantitative Method for Imaging the Elasticity of Biological Tissues. *Ultrason. Imaging* *13*, 111–134.
- Ophir, J., Alam, S.K., Garra, B., Kallel, F., Konofagou, E., Krouskop, T., and Varghese, T. (1999). Elastography: Ultrasonic estimation and imaging of the elastic properties of tissues. *Proc. Inst. Mech. Eng. [H]* *213*, 203–233.
- Oudry, J., Chen, J., Glaser, K.J., Miette, V., Sandrin, L., and Ehman, R.L. (2009a). Cross-validation of magnetic resonance elastography and ultrasound-based transient elastography: A preliminary phantom study. *J. Magn. Reson. Imaging* *30*, 1145–1150.
- Oudry, J., Vappou, J., Choquet, P., Willinger, R., Sandrin, L., and Constantinesco, A. (2009b). Ultrasound-based transient elastography compared to magnetic resonance elastography in soft tissue-mimicking gels. *Phys. Med. Biol.* *54*, 6979.
- Oudry, J., Lynch, T., Vappou, J., Sandrin, L., and Miette, V. (2014). Comparison of four different techniques to evaluate the elastic properties of phantom in elastography: is there a gold standard? *Phys. Med. Biol.* *59*, 5775–5793.
- Palacio-Torralba, J., Hammer, S., Good, D.W., Alan McNeill, S., Stewart, G.D., Reuben, R.L., and Chen, Y. (2015a). Quantitative diagnostics of soft tissue through viscoelastic characterization using time-based instrumented palpation. *J. Mech. Behav. Biomed. Mater.* *41*, 149–160.
- Palacio-Torralba, J., Hammer, S., Good, D.W., Alan McNeill, S., Stewart, G.D., Reuben, R.L., and Chen, Y. (2015b). Quantitative diagnostics of soft tissue through viscoelastic characterization using time-based instrumented palpation. *J. Mech. Behav. Biomed. Mater.* *41*, 149–160.
- Palevski, A., Gleich, I., Portnoy, S., Linder-Ganz, E., and Gefen, A. (2006). Stress Relaxation of Porcine Gluteus Muscle Subjected to Sudden Transverse Deformation as Related to Pressure Sore Modeling. *J. Biomech. Eng.* *128*, 782–787.
- Papazoglou, S., Rump, J., Braun, J., and Sack, I. (2006). Shear wave group velocity inversion in MR elastography of human skeletal muscle. *Magn. Reson. Med.* *56*, 489–497.
- Papazoglou, S., Hirsch, S., Braun, J., and Sack, I. (2012). Multifrequency inversion in magnetic resonance elastography. *Phys. Med. Biol.* *57*, 2329–2346.
- Peters, A., Wortmann, S., Elliott, R., Staiger, M., Chase, J.G., and Houten, E.V. (2005). Digital Image-Based Elasto-Tomography: First Experiments in Surface Based Mechanical

Property Estimation of Gelatine Phantoms. *JSME Int. J. Ser. C Mech. Syst. Mach. Elem. Manuf.* 48, 562–569.

Pette, D., and Vrbová, G. (1985). Invited review: Neural control of phenotypic expression in mammalian muscle fibers. *Muscle Nerve* 8, 676–689.

Plaghki, L. (1985). Régénération et myogenèse du muscle strié. *J. Physiol. (Paris)* 80, 51–110.

Qin, E.C., Sinkus, R., Rae, C., and Bilston, L.E. (2011a). Investigating anisotropic elasticity using MR-elastography combined with diffusion tensor imaging: validation using anisotropic and viscoelastic phantoms. In *Proc. Intl. Soc. Mag. Reson. Med.*, p. 39.

Qin, E.C., Sinkus, R., Rae, C., and Bilston, L.E. (2011b). Investigating anisotropic elasticity using MR-elastography combined with diffusion tensor imaging: validation using anisotropic and viscoelastic phantoms. In *Proc. Intl. Soc. Mag. Reson. Med.*, p. 39.

Qin, E.C., Sinkus, R., Geng, G., Cheng, S., Green, M., Rae, C.D., and Bilston, L.E. (2013). Combining MR elastography and diffusion tensor imaging for the assessment of anisotropic mechanical properties: A phantom study. *J. Magn. Reson. Imaging* 37, 217–226.

Qin, E.C., Jugé, L., Lambert, S.A., Paradis, V., Sinkus, R., and Bilston, L.E. (2014). In Vivo Anisotropic Mechanical Properties of Dystrophic Skeletal Muscles Measured by Anisotropic MR Elastographic Imaging: The mdx Mouse Model of Muscular Dystrophy. *Radiology* 132661.

Reeves, N.D., and Narici, M.V. (2003). Behavior of human muscle fascicles during shortening and lengthening contractions in vivo. *J. Appl. Physiol.* 95, 1090–1096.

Ridge, M.D., and Wright, V. (1966). Mechanical properties of skin: a bioengineering study of skin structure. *J. Appl. Physiol.* 21, 1602–1606.

Ringleb, S.I., Chen, Q., Lake, D.S., Manduca, A., Ehman, R.L., and An, K.-N. (2005). Quantitative shear wave magnetic resonance elastography: Comparison to a dynamic shear material test. *Magn. Reson. Med.* 53, 1197–1201.

Ringleb, S.I., Bensamoun, S.F., Chen, Q., Manduca, A., An, K.-N., and Ehman, R.L. (2007). Applications of magnetic resonance elastography to healthy and pathologic skeletal muscle. *J. Magn. Reson. Imaging* 25, 301–309.

Roan, E., and Vemaganti, K. (2006). The Nonlinear Material Properties of Liver Tissue Determined From No-Slip Uniaxial Compression Experiments. *J. Biomech. Eng.* 129, 450–456.

Robert, B. (2009). Etude des Propriétés Viscoélastiques des Tissus Mous par Elastographie IRM. Une Approche Multi-Echelle. phdthesis. Université Paris-Diderot - Paris VII.

Robertson, J.D. (1961). Studies on the Chemical Composition of Muscle Tissue II. The Abdominal Flexor Muscles of the Lobster *Nephrops Norvegicus* (L.). *J. Exp. Biol.* 38, 707–728.

- Romano, A., Scheel, M., Hirsch, S., Braun, J., and Sack, I. (2012). In vivo waveguide elastography of white matter tracts in the human brain. *Magn. Reson. Med.* 68, 1410–1422.
- Rouvière, O., Yin, M., Dresner, M.A., Rossman, P.J., Burgart, L.J., Fidler, J.L., and Ehman, R.L. (2006). MR Elastography of the Liver: Preliminary Results. *Radiology* 240, 440–448.
- Rutherford, O.M., and Jones, D.A. (1992). Measurement of fibre pennation using ultrasound in the human quadriceps in vivo. *Eur. J. Appl. Physiol.* 65, 433–437.
- Sack, I., Bernarding, J., and Braun, J. (2002). Analysis of wave patterns in MR elastography of skeletal muscle using coupled harmonic oscillator simulations. *Magn. Reson. Imaging* 20, 95–104.
- Sack, I., Beierbach, B., Hamhaber, U., Klatt, D., and Braun, J. (2008). Non-invasive measurement of brain viscoelasticity using magnetic resonance elastography. *NMR Biomed.* 21, 265–271.
- Sahebjavaher, R.S., Baghani, A., Honarvar, M., Sinkus, R., and Salcudean, S.E. (2013). Transperineal prostate MR elastography: Initial in vivo results. *Magn. Reson. Med.* 69, 411–420.
- Sahebjavaher, R.S., Nir, G., Gagnon, L.O., Ischia, J., Jones, E.C., Chang, S.D., Yung, A., Honarvar, M., Fazli, L., Goldenberg, S.L., et al. (2014). MR elastography and diffusion-weighted imaging of ex vivo prostate cancer: quantitative comparison to histopathology. *NMR Biomed.* n/a – n/a.
- Saito, K., Nakaji, S., Umeda, T., Shimoyama, T., Sugawara, K., and Yamamoto, Y. (2003). Development of predictive equations for body density of sumo wrestlers using B-mode ultrasound for the determination of subcutaneous fat thickness. *Br. J. Sports Med.* 37, 144–148.
- Samani, A., Bishop, J., Luginbuhl, C., and Plewes, D.B. (2003). Measuring the elastic modulus of ex vivo small tissue samples. *Phys. Med. Biol.* 48, 2183.
- Sandrin, L., Tanter, M., Gennisson, J.-L., Catheline, S., and Fink, M. (2002). Shear elasticity probe for soft tissues with 1-D transient elastography. *IEEE Trans. Ultrason. Ferroelectr. Freq. Control* 49, 436–446.
- Sarvazyan, A.P., Rudenko, O.V., Swanson, S.D., Fowlkes, J.B., and Emelianov, S.Y. (1998). Shear wave elasticity imaging: a new ultrasonic technology of medical diagnostics. *Ultrasound Med. Biol.* 24, 1419–1435.
- Scheel, M., von Roth, P., Winkler, T., Arampatzis, A., Prokscha, T., Hamm, B., and Diederichs, G. (2013). Fiber type characterization in skeletal muscle by diffusion tensor imaging. *NMR Biomed.* n/a – n/a.
- Scholten, R. r., Pillen, S., Verrips, A., and Zwarts, M. j. (2003). Quantitative ultrasonography of skeletal muscles in children: Normal values. *Muscle Nerve* 27, 693–698.
- Schregel, K., Wuerfel, E., Wuerfel, J., Petersen, D., and Sinkus, R. (2010). Viscoelastic properties change at an early stage of cuprizone induced affection of oligodendrocytes in the

corpus callosum of C57/black6 mice. In Proceedings of the International Society for Magnetic Resonance in Medicine, pp. 535–539.

Schregel, K., Tysiak, E.W. née, Garteiser, P., Gemeinhardt, I., Prozorovski, T., Aktas, O., Merz, H., Petersen, D., Wuerfel, J., and Sinkus, R. (2012). Demyelination reduces brain parenchymal stiffness quantified in vivo by magnetic resonance elastography. *Proc. Natl. Acad. Sci.* *109*, 6650–6655.

Schwartz, J.-M., Denninger, M., Rancourt, D., Moisan, C., and Laurendeau, D. (2005). Modelling liver tissue properties using a non-linear visco-elastic model for surgery simulation. *Med. Image Anal.* *9*, 103–112.

Serai, S.D., Towbin, A.J., and Podberesky, D.J. (2012). Pediatric Liver MR Elastography. *Dig. Dis. Sci.*

Sherwood, L. (2015). *Human Physiology: From Cells to Systems* (Cengage Learning).

Shinohara, M., Sabra, K., Gennisson, J.-L., Fink, M., and Tanter, M. (2010). Real-time visualization of muscle stiffness distribution with ultrasound shear wave imaging during muscle contraction. *Muscle Nerve* *42*, 438–441.

Sinkus, R., Tanter, M., Catheline, S., Lorenzen, J., Kuhl, C., Sondermann, E., and Fink, M. (2005a). Imaging anisotropic and viscous properties of breast tissue by magnetic resonance-elastography. *Magn. Reson. Med.* *53*, 372–387.

Sinkus, R., Tanter, M., Catheline, S., Lorenzen, J., Kuhl, C., Sondermann, E., and Fink, M. (2005b). Imaging anisotropic and viscous properties of breast tissue by magnetic resonance-elastography. *Magn. Reson. Med.* *53*, 372–387.

Sinkus, R., Daire, J.-L., Van Beers, B.E., and Vilgrain, V. (2010). Elasticity reconstruction: Beyond the assumption of local homogeneity. *Comptes Rendus Mécanique* *338*, 474–479.

Storaa, C., Åberg, P., Lind, B., and Brodin, L.-Å. (2003). Effect of Angular Error on Tissue Doppler Velocities and Strain. *Echocardiography* *20*, 581–587.

Støylen, A. (2001). Strain rate imaging of the left ventricle by ultrasound. *Feasibility Clin. Valid. Physiol. Asp.*

Talwalkar, J.A., Yin, M., Fidler, J.L., Sanderson, S.O., Kamath, P.S., and Ehman, R.L. (2008). Magnetic resonance imaging of hepatic fibrosis: Emerging clinical applications. *Hepatology* *47*, 332–342.

Tanter, M., Bercoff, J., Sinkus, R., Deffieux, T., Gennisson, J.-L., and Fink, M. (2007). L'élastographie par ultrasons ou résonance magnétique : de nouveaux outils de diagnostic en cancérologie. *Médecine Nucl.* *31*, 132–141.

Tanter, M., Bercoff, J., Athanasiou, A., Deffieux, T., Gennisson, J.-L., Montaldo, G., Muller, M., Tardivon, A., and Fink, M. (2008). Quantitative Assessment of Breast Lesion Viscoelasticity: Initial Clinical Results Using Supersonic Shear Imaging. *Ultrasound Med. Biol.* *34*, 1373–1386.

- Tomlinson, M., Daly, C., Odland, G., and Short, J. (1969). In vivo measurement of skin elasticity—a clinical evaluation.
- Tracy, B.L., Ivey, F.M., Jeffrey Metter, E., Fleg, J.L., Siegel, E.L., and Hurley, B.F. (2003). A More Efficient Magnetic Resonance Imaging-Based Strategy for Measuring Quadriceps Muscle Volume. *Med. Sci. Sports Exerc.* 35, 425–433.
- Tse, Z.T.H., Janssen, H., Hamed, A., Ristic, M., Young, I., and Lamperth, M. (2009). Magnetic resonance elastography hardware design: A survey. *Proc. Inst. Mech. Eng. [H]* 223, 497–514.
- Van Turnhout, M., Peters, G., Stekelenburg, A., and Oomens, C. (2005). Passive transverse mechanical properties as a function of temperature of rat skeletal muscle in vitro. *Biorheology* 42, 193–207.
- Vain, A. (1995). Estimation of the functional state of skeletal muscle. *Control Ambulation Using Funct. Neuromuscul. Stimul.* 51–55.
- Vappou, J., Breton, E., Choquet, P., Goetz, C., Willinger, R., and Constantinesco, A. (2007). Magnetic resonance elastography compared with rotational rheometry for in vitro brain tissue viscoelasticity measurement. *Magn. Reson. Mater. Phys. Biol. Med.* 20, 273–278.
- Vappou, J., Breton, E., Choquet, P., Willinger, R., and Constantinesco, A. (2008). Assessment of in vivo and post-mortem mechanical behavior of brain tissue using magnetic resonance elastography. *J. Biomech.* 41, 2954–2959.
- Vappou, J., Luo, J., and Konofagou, E.E. (2010). Pulse Wave Imaging for Noninvasive and Quantitative Measurement of Arterial Stiffness In Vivo. *Am. J. Hypertens.* 23, 393–398.
- Veldi, M., Vasar, V., Vain, A., and Kull, M. (2004). Obstructive sleep apnea and ageing: Myotonometry demonstrates changes in the soft palate and tongue while awake. *Pathophysiology* 11, 159–165.
- Venkatesh, S.K., Yin, M., Glockner, J.F., Takahashi, N., Araoz, P.A., Talwalkar, J.A., and Ehman, R.L. (2008). MR Elastography of Liver Tumors: Preliminary Results. *Am. J. Roentgenol.* 190, 1534–1540.
- Viiir, R., Laiho, K., Kramarenko, J., and Mikkelsen, M. (2006). Repeatability of trapezius muscle tone assessment by a myometric method. *J. Mech. Med. Biol.* 06, 215–228.
- Walton, J.M., Roberts, N., and Whitehouse, G.H. (1997). Measurement of the quadriceps femoris muscle using magnetic resonance and ultrasound imaging. *Br. J. Sports Med.* 31, 59–64.
- Wickiewicz, T.L., Roy, R.R., Powell, P.L., and Edgerton, V.R. (1983). Muscle Architecture of the Human Lower Limb. *Clin. Orthop.* 179.
- Williams, S.E., Heemskerk, A.M., Welch, E.B., Li, K., Damon, B.M., and Park, J.H. (2013). Quantitative effects of inclusion of fat on muscle diffusion tensor MRI measurements. *J. Magn. Reson. Imaging* n/a – n/a.

- Wu, Z., Hoyt, K., Rubens, D.J., and Parker, K.J. (2006). Sonoelastographic imaging of interference patterns for estimation of shear velocity distribution in biomaterials. *J. Acoust. Soc. Am.* *120*, 535–545.
- Xu, L., Lin, Y., Han, J.C., Xi, Z.N., Shen, H., and Gao, P.Y. (2007a). Magnetic Resonance Elastography of Brain Tumors: Preliminary Results. *Acta Radiol.* *48*, 327–330.
- Xu, L., Lin, Y., Xi, Z.N., Shen, H., and Gao, P.Y. (2007b). Magnetic Resonance Elastography of the Human Brain: A Preliminary Study. *Acta Radiol.* *48*, 112–115.
- Yin, M., Talwalkar, J.A., Glaser, K.J., Manduca, A., Grimm, R.C., Rossman, P.J., Fidler, J.L., and Ehman, R.L. (2007). Assessment of Hepatic Fibrosis With Magnetic Resonance Elastography. *Clin. Gastroenterol. Hepatol.* *5*, 1207–1213.e2.
- Yin, M., Rouvière, O., Glaser, K.J., and Ehman, R.L. (2008). Diffraction-biased shear wave fields generated with longitudinal magnetic resonance elastography drivers. *Magn. Reson. Imaging* *26*, 770–780.
- Young, A., Stokes, M., and Crowe, M. (1984). Size and strength of the quadriceps muscles of old and young women*. *Eur. J. Clin. Invest.* *14*, 282–287.
- Yucesoy, C.A., Koopman, B.H.F.J.M., Huijing, P.A., and Grootenboer, H.J. (2002). Three-dimensional finite element modeling of skeletal muscle using a two-domain approach: linked fiber-matrix mesh model. *J. Biomech.* *35*, 1253–1262.
- Zerhouni, E.A., Parish, D.M., Rogers, W.J., Yang, A., and Shapiro, E.P. (1988). Human heart: tagging with MR imaging--a method for noninvasive assessment of myocardial motion. *Radiology* *169*, 59–63.
- Zheng, Y.-P., Mak, A.F.T., and Lue, B. (1999). Objective assessment of limb tissue elasticity : development of a manual indentation procedure. *J. Rehabil. Res. Dev.* *36*, 71–85.
- Zuberi, S.M., Matta, N., Nawaz, S., Stephenson, J.B.P., McWilliam, R.C., and Hollman, A. (1999). Muscle ultrasound in the assessment of suspected neuromuscular disease in childhood. *Neuromuscul. Disord.* *9*, 203–207.

CHAPTER 2

MATERIELS

AND

METHODS

CHAPTER 2 MATERIELS AND METHODS 89

A. Phantom study 92

 1. Phantom preparation 92

 2. Development of phantom with similar muscle architecture 93

 3. Development of a device to stretch the fiber 94

 4. Determination of the mechanical properties 94

 1. Hyper-Frequency Viscoelastic Spectroscopy (HFVS) 94

 2. Magnetic Resonance Elastography tests 95

 2.1 MR elastography set-up for the artificial muscle..... 95

 2.2 Multifrequency MRE set-up performed on the homogeneous phantom..... 96

 2.3 Phase Image processing and data analysis..... 98

 2.4 Summary of the different tests applied to the developed phantoms. 101

B. Thigh muscle study..... 102

 1. Ethics Statement..... 102

 2. Participants..... 102

 3. Experimental configuration..... 102

 4. Acquisition of the anatomical and phase images of the muscle 105

 5. Phase Image Processing and Data Analysis..... 107

 6. Statistical analysis 109

This second chapter will be composed of two parts related to in vitro (phantom) and in vivo (muscle) studies.

The in vitro section is composed of a description of the phantoms manufacture which has similar muscle architecture. Then, mechanical and MRE tests have been performed on the phantoms. The displacement of the wave will be analysed with different pneumatic drivers and the mechanical properties will be determined. In addition, new data processing methods will be tested on the phantoms before in vivo muscle analysis. This study is to develop MRE methods to determine the passive elastic.

The second part is dedicated to in vivo study of thigh muscle tissues with no muscle abnormalities or histories of muscle disease. The developed experimental MRE muscle protocols for the quantification of the elastic properties of all thigh muscle will be presented. In addition, multifrequency (70, 90, 110 Hz) MRE tests associated to a new data-processing method will be described for the viscoelastic measurements.

A. Phantom study

1. Phantom preparation

Homogeneous phantoms were created with different concentrations of liquid plastic (Plastileurre, Bricoleurre, France) and softener (Assouplissant, Bricoleurre, France) in order to mimic the muscle biological tissues. Thus, the phantoms were made with a mixture of softener and liquid plastic (LureCraft, LaGrande, USA), or plastisol (Figure 2.1A), which is a suspension of PVC (polyvinyl chloride) particles in a plasticizer. The advantages of using Plastisol® are performing tests-objects with different elasticities, having a very resistant product, in their chemical composition and in their mechanical properties over time. In addition, the Plastisol® has a density close to that of soft tissue.

The mixture was adjusted from 30% to 70% with a step concentration of 10%, in order to progressively increase the stiffness of the media. Based on previous studies, the phantoms composed of 50% and 70% of plastisol will be used for MRE and mechanical tests. Indeed, we have demonstrated that 50% and 70% plastisol correspond to a passive and active muscle, respectively. Subsequently, both mixtures were heated to 177 °C, and the solution was poured into cylindrical molds (aluminum) (Figure 2.1B) with two different sizes which were resistant to high temperature. The first has a large diameter ($d=14$ cm, height: 15cm) (Figure 2.1C) and is used for MRE test. The other one has a smaller diameter ($d=9.9$ mm, height 76 mm) and is used for mechanical Hyper-Frequency Viscoelastic Spectroscopy (HFVS) tests.

The mixtures left to cool at the room temperature (23°C) until the phantoms were solidified. Then they were stocked and preserved at the room temperature (23°C). The density of the phantoms was evaluated as similar to the biological tissues (1000 kg/m³).

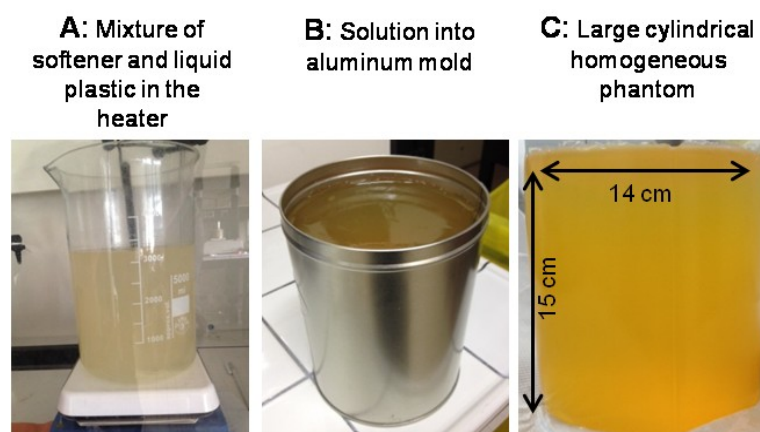


Figure 2.1: Manufacturing protocol for plastic phantoms

2. Development of phantom with similar muscle architecture

The thigh is composed of superficial muscles (RF) and deep (VI) muscles (Figure 2.3A), made of muscle fibers ($10\ \mu\text{m} < D < 100\ \mu\text{m}$) and separated with aponeurosis membrane. To represent the muscle fibers inside the phantom, teflon tubing pipe (internal diameter: 0.6 mm, external diameter: 0.9 mm) were thread in the upper part of the phantom composed of 50% plastisol. The fibers were oriented parallel to the main axis of the phantom (Figure 2.2A).



Figure 2.2: Fibers orientation

To mimick the aponeurosis membrane, a plastic sheet (8 x 15 cm, thickness = 1 mm) was included in the middle of the phantom (Figure 2.3B). The structure of the phantom was visualized through a MRI acquisition (Figure 2.3B).

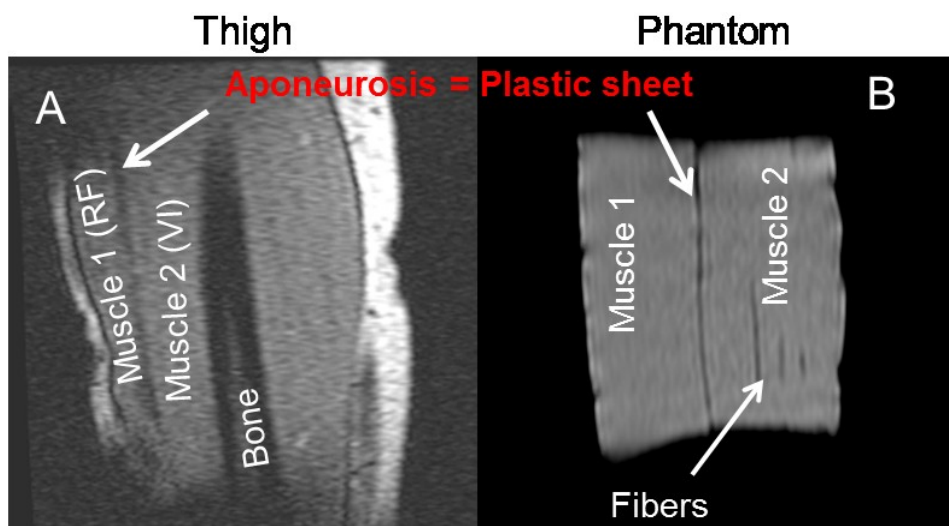


Figure 2.3: MRI sagittal acquisitions of the thigh muscles (A) (RF: rectus femoris, VI: vastus intermedius) and (B) the phantom showing similar structures.

3. Development of a device to stretch the fiber

A mechanical device, compatible MRI, was manufactured in UTC, to mimic a stretch muscle. Thus, the objective was to stretch the fibers inclusion. The teflon fibers are placed between two opposite circles discs which were desined with 50 hols , separatd by a distance of 10 mm. A load cell (5 – 2000 N) was fixed at one end to measure the level of stretch applied to the fibers.

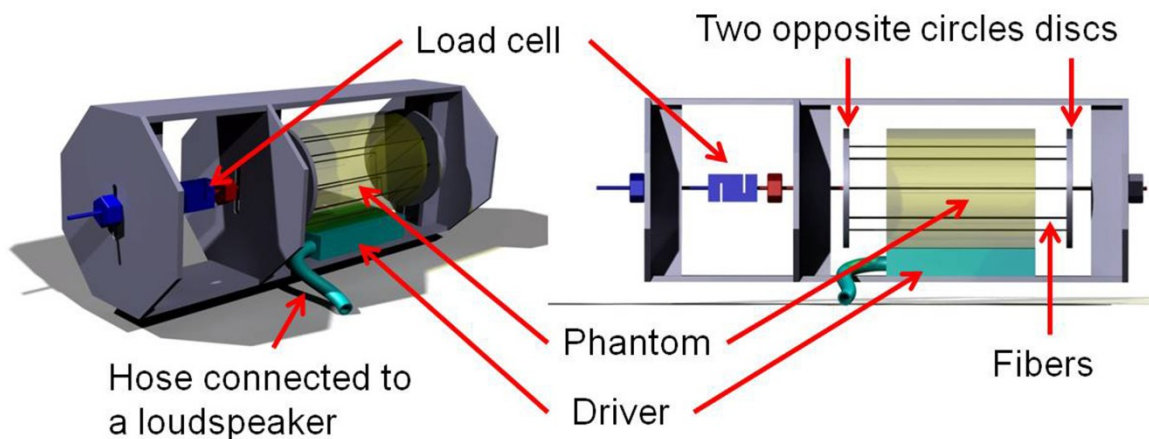


Figure 2.4: Device to stretch the fibers

4. Determination of the mechanical properties

1. Hyper-Frequency Viscoelastic Spectroscopy (HFVS)

The Hyper-Frequency Viscoelastic Spectroscopy (HFVS) mechanical test was performed, in collaboration with Cedric Schmitt from Rheolution Inc, using the RheoSpectris C500 instrument (Montreal, QC, Canada) (Figure 2.5). This instrument is a new generation viscoelastic spectroscope capable of measuring the storage (G') and loss (G'') moduli of materials in a wide frequency range between 10 Hz and 1500 Hz.

The basic principle of this instrument is to generate transient mechanical shear waves inside the probed sample confined into a rigid cylindrical holder and to measure the behavior (vibration) of the entire sample monitored at the surface, using an ultra-sensitive optical sensor to process the viscoelastic spectroscopy. For each measurement, the small phantom (50% of plastisol) was contained in a cylindrical holder ($D=10\text{mm}$) and was placed in the mechanical unit specially designed for cylindrical geometries. From the viscoelastic measurements over

the full frequency range (from 10 Hz to 500 Hz), only 60, 80 and 100 Hz were selected to compare with the same frequencies used during MRE tests.

A study of reproducibility of the measurement was performed according to the protocol which was to remove the sample and then return it to take another measurement. This was done three times for each sample in order to calculate the standard deviation of the measurement.

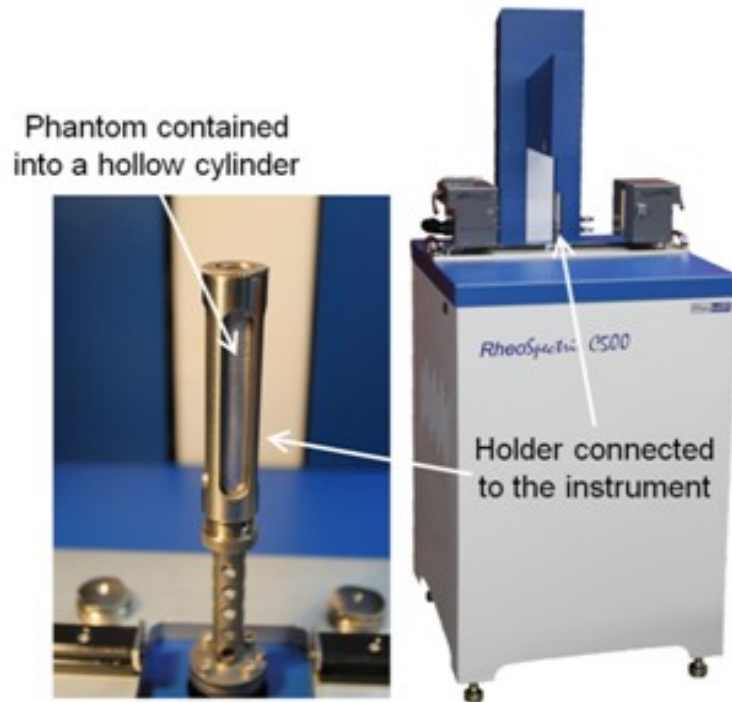


Figure 2.5: Set up of the hyper-frequency viscoelastic spectroscopy tests performed on the different small phantoms

2. Magnetic Resonance Elastography tests

The tests were all performed at the Advanced Medical Imaging Centre (CIMA) and at the Polyclinic Saint-Côme, in Compiègne, in collaboration with Ludovic Robert, MRI radiographer, and Dr charleux, radiologist at CIMA- polyclinic ST-côme.

2.1 MR elastography set-up for the artificial muscle

MRE tests were conducted on the large phantom composed of 50% plastisol, within a 1.5T MRI machine (General Electric HDxt). The phantom was placed on the MRI table with the fibers oriented in the same direction as in vivo muscle MRE test.

To generate the waves within the phantom, two different pneumatic drivers were used to analyze the effect of the driver on the wave propagation. The first one was the same silicone tube used for in vivo muscle (Figure 2.6A). The second one has a round shape, and is used in clinical practice for MRE liver analysis (Figure 2.6B). The tube driver was wrapped and clamped around one extremity of the phantom simulating the in vivo placement of the tube at the end of the distal part of the thigh (Bensamoun et al., 2006b). The round driver (D=15 cm) was placed below and then above the phantom (Figure 2.6B). A long hose was connected to a large active loudspeaker to send the air pressure at the optimal in vivo muscle frequency (f : 90 Hz) (Bensamoun et al, 2006). The MR acquisitions were recorded with the body coil.

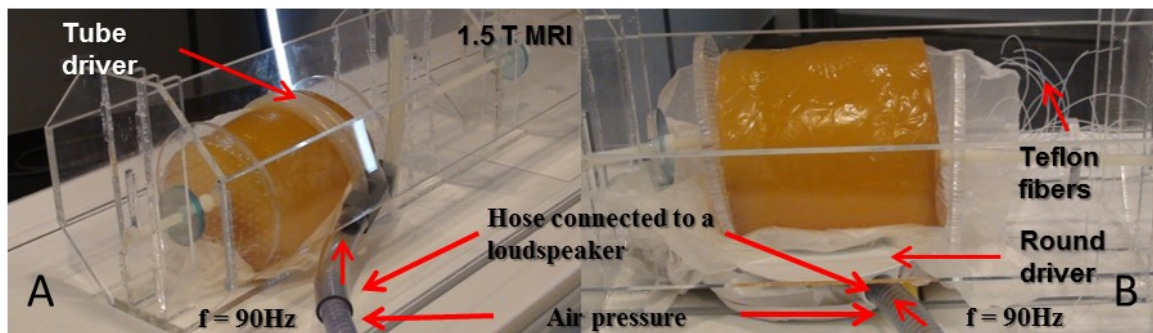


Figure 2.6: MRE tests performed on the large phantom with two different drivers.

MRE sequence was performed with four offsets, a gradient echo sequence, an acquisition matrix of 256 x 64 (interpolated to 256 x 256), a flip angle of 45°, a field of view of 30 cm, TR equal to 50 ms and TE corresponding to the minimum echo time allowing for motion encoding. Phase images, showing the displacement of the shear waves inside the phantom, were collected to analyze the propagation of the wave according to the type of the driver.

2.2 Multifrequency MRE set-up performed on the homogeneous phantom

Multifrequency MRE (MMRE) was realized on a 50% plastic phantom without fiber and sheet inclusion. The phantom was positioned inside the head coil of the scanner with the phantom cylinder perpendicular to the static scanner field. Harmonic compression excitation was generated with home made pneumatic driver having a round (D=15cm) shape similar to the clinical liver driver. It was placed below the phantom (Figure 2.7a).

The main vibration direction was perpendicular to the static B₀-field direction, and waves are propagated parallel to the main axis of the phantom cylinder. Image slices were

acquired in the sagittal plane in order to obtain vertical wave displacement through the phantom (Figures. 2.7b, c, d). Harmonic drive frequencies were performed at 60, 80 and 100 Hz. MRE sequence was realized with the following parameters: TR/TE = 56 ms / 23 ms, 256 × 256 matrix size, 200 × 200 cm FOV, 1.5 mm slice thickness, four offsets.

Phase images, revealing the propagation of the shear waves, were recorded (Figure 2.7b-d).

a

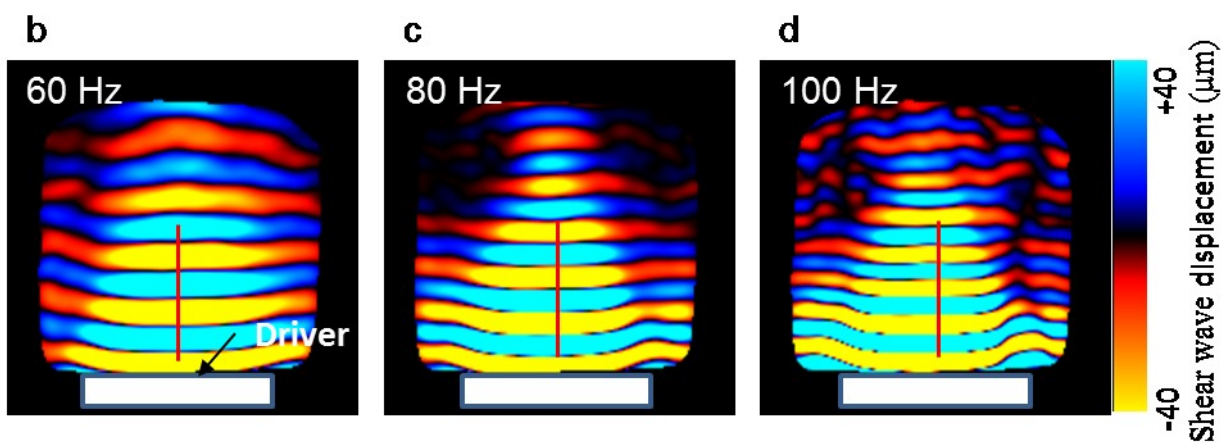
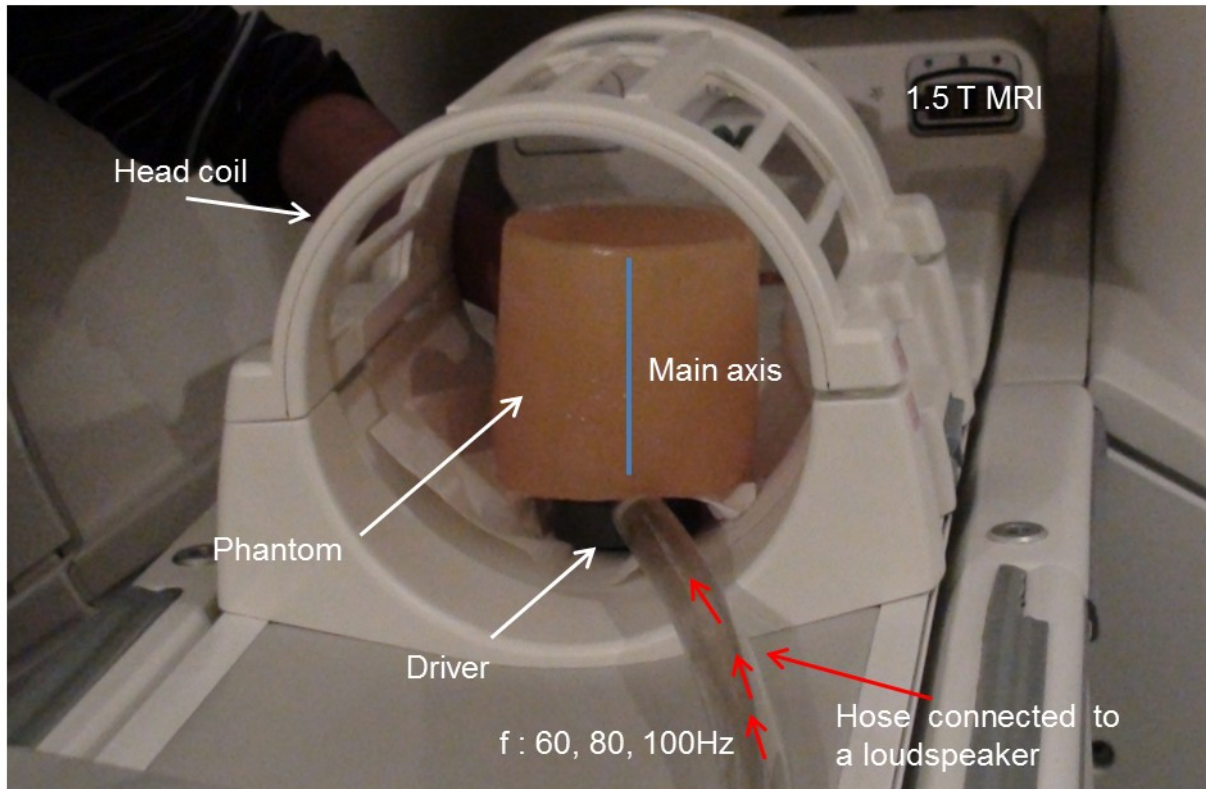


Figure 2.7: MRE Experimental set-up for the homogeneous phantom (a) (50% plastic). Phase images showing wave's displacement inside the phantoms at 60 Hz (b), 80Hz (c) and 100 Hz (d).

2.3 Phase Image processing and data analysis

- Elastic properties

A post-processing was applied with a mask, removing the noise located in the background of the image. Butterworth filter was also applied to suppress interfering wave patterns. The mechanical (elasticity and viscosity) properties of the phantoms were obtained with the following method.

A local stiffness is measured by prescribing a 1D profile drawn along the direction of the shear wave propagation (Figure 2.8a). A representation of the behavior of the wavelength (λ), along the profile, enables to measure the wavelength (Figure 2.8a), which was determined by considering the distance between consecutive picks (Figure 2.8b). The local elastic properties (shear modulus) were calculated at each frequency, from the displacement of the shear wave. Assuming that the media is linear elastic, isotropic, homogeneous and incompressible, the shear modulus was calculated using the following equation $\mu = \rho \cdot (f \cdot \lambda)^2$, where ρ is the muscle density fixed to 1000 kg/m^3 and f is the frequency.

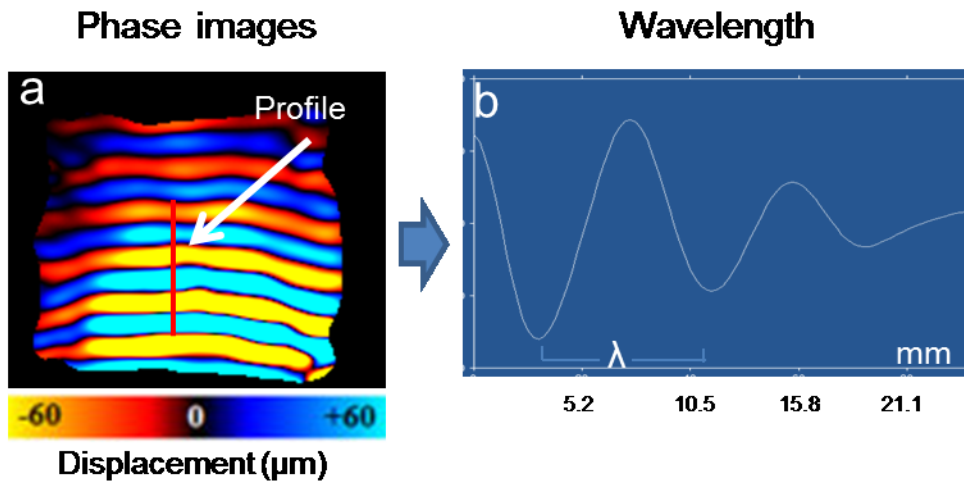


Figure 2.8: a: MRE tests performed on the homogeneous phantom (50%) showing the wave's displacement. B: Behaviors of the waves traveling along the red profile.

- Viscoelastic property

Theory

Experimental ($\underline{G}(\omega)$) and numerical ($\underline{G}_{\text{Model}}(\omega)$) complexe viscoelastic parameters were determined using basic equations that are summarized below.

A black profile (Figure 2.9a) was prescribed in the direction (x) of the wave propagation, and the wave behavior along this profile was extracted (Figure 2.9b). The amplitude of the wave along the profile was referred to as a scalar wave field $u(x, t)$ whose temporal Fourier-transformation was denoted as $\underline{U}(x, \omega)$. Assuming that the medium of propagation was linear, locally homogeneous, isotropic, incompressible, and under pure shear stress, the motion equation (Helmholtz) in the frequency domain was (Klatt et al., 2010):

$$\rho \omega^2 \underline{U} + \underline{G}(\omega) \frac{\partial^2}{\partial x^2} \underline{U} = 0 \quad [1]$$

where $\omega = 2 \pi f$ is the angular driving frequency, $\underline{G}(\omega) = G' + i G''$ is the complex shear modulus, and ρ is the muscle density.

It was assumed that the displacement of the wave followed a harmonic plane wave represented by the equation:

$$\underline{U} = u_0 \exp [-i \underline{k} x] \quad [2]$$

where u_0 is the initial amplitude, and $\underline{k} = k - i \gamma$ is the complex wave number (k and γ are real parameters).

The parameter (k) was linked to the wavelength (λ) by the relationship $k = \frac{2\pi}{\lambda}$. The parameter (γ) corresponded to the attenuation coefficient. These two parameters were measured from the analysis of wave displacement $u(x, t)$ along the red profile (Figure 2.9a). The wavelength (λ) was measured with the different extrema, and the corresponding location (x_i) was extracted from the wave (Figure 2.9b). Two consecutive extrema were separated in (x) by a half period ($\frac{\lambda}{2}$). For better accuracy, the first and last extrema were used to deduce the value of λ (Figure. 9c). This process was applied to each offset and an average of the wavelength was determined.

Subsequently, a logarithmic $\ln(|U_i|)$ representation of the extrema was fitted with a linear least square line, which allowed measurement of the attenuation (γ) parameter (Figure 2.9c). It can be noted that the slope of the line corresponded to $-\gamma$.

Solving Eq. [1] for $\underline{G}(\omega)$ with \underline{U} from Eq. [2], and the parameters (k, γ), gave the following experimental viscoelastic parameters:

$$G'(\omega) = \rho\omega^2 \frac{k^2 - \gamma^2}{(k^2 - \gamma^2)^2 + (2k\gamma)^2} \quad [3]$$

$$G''(\omega) = \rho\omega^2 \frac{2k\gamma}{(k^2 - \gamma^2)^2 + (2k\gamma)^2} \quad [4]$$

The complex modulus was related to elasticity (μ) and viscosity (η) using various rheological models. In this study, the four following models for $\underline{G}_M(\omega)$ were used:

$$\underline{G}_M(\omega) = \begin{cases} \mu + i\omega\eta & \text{Voigt} \\ \frac{i\omega\eta\mu}{\mu + i\omega\eta} & \text{Maxwell} \\ \frac{\mu_1\mu_2 + i\omega\eta(\mu_1 + \mu_2)}{\mu_2 + i\omega\eta} & \text{Zener} \\ \mu^{1-\alpha}\eta^\alpha (i\omega)^\alpha & \text{Springpot} \end{cases} \quad [5]$$

Whereas the Voigt and Maxwell models require two parameters (μ : shear modulus and η : shear viscosity), the Zener (μ_1, μ_2, η) and springpot (μ, η, α) models take three parameters into account. The parameter α represented a weighting factor between a purely elastic behavior ($\alpha = 0$) and a purely viscous behavior ($\alpha = 1$). For the springpot model, (μ) and (η) were linearly dependent, meaning that either the value of (μ) or (η) were fixed. Using the same assumption as in Klatt et al.'s study (2010), we fixed the η value to the data obtained in the Zener model.

The viscoelastic parameters (μ, η, α) from these four models were calculated by minimizing the following error (χ):

$$\chi = \frac{1}{N} \sum_{n=1}^N \sqrt{(\text{Re}[G(\omega_n) - \underline{G}_M(\omega_n)])^2 + (\text{Im}[G(\omega_n) - \underline{G}_M(\omega_n)])^2} \quad [6]$$

where N is the number of experimental driving frequencies ($N=3$).

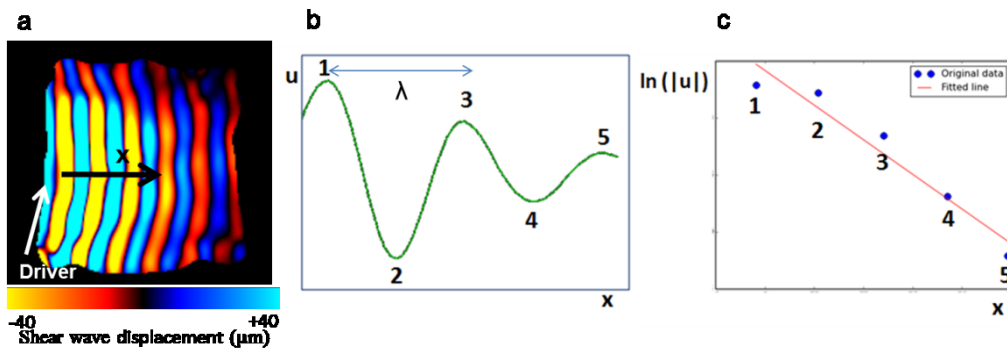


Figure 2.9: Illustration of the process for the evaluation of attenuation. *a*: Phase image with the propagation of the shear wave through the phantom where a profile (black arrow) is

drawn in the direction of propagation. *b*: Amplitude of the profile along the distance *x*. *c*: Plot of the extrema of the amplitude profile and of the least-square fitted line for the calculation of the attenuation coefficient.

- Image processing

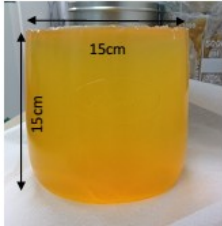
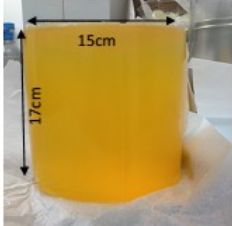
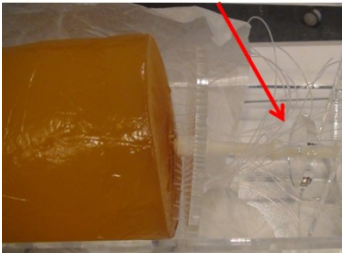

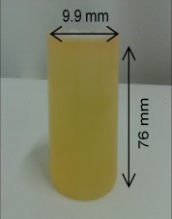
The complex shear modulus $\underline{G}(\omega)$ was then calculated according to equations [3] and [4] assuming a density of 1000 kg.m^{-3} . An average result was obtained over the four offset images. The rheological models were then estimated by minimizing the Eq. 6.

Three relative errors were also computed to compare the quality of fit along the driving frequencies:

$$\chi_{\text{fn}} = 100 \left| \frac{\sqrt{(\text{Re}[\underline{G}_M(\omega_n)])^2 + (\text{Im}[\underline{G}_M(\omega_n)])^2}}{\sqrt{(\text{Re}[\underline{G}(\omega_n)])^2 + (\text{Im}[\underline{G}(\omega_n)])^2}} - 1 \right| \quad [7]$$

where $n = 1, 2, 3$; $\omega_n = 2 \pi f_n$; $f_1 = 70 \text{ Hz}$; $f_2 = 90 \text{ Hz}$; $f_3 = 110 \text{ Hz}$

2.4 Summary of the different tests applied to the developed phantoms.

Phantoms		Techniques	Mechanical parameters
Homogeneous phantoms (50%, 70%) of plastic	50%  = Relaxed muscle	MMRE test	μ, η, G', G''
	70%  = Contracted muscle		
Teflon fiber and plastic sheet inside the phantom (50%) of plastic	Teflon tubing pipe 	MRE test	$\mu, \text{wave behaviours}$
	Plastic sheet 		
Small plastic phantom (50%)		HFVS test	G', G''

B. Thigh muscle study

This section presents the developed experimental MRE muscle protocols and the data-processing for quantifying the passive elasticity and viscosity.

1. Ethics Statement

In this study, the examinations were all performed at the Centre d'Imagerie Médicale Avancée (CIMA), Compiègne hospital, in collaboration with Ludovic Robert, radiographer and with the presence of Dr. Charleux, radiologist.

The human subject ethical approval was sought from the institutional review board of Amiens Hospital, and all the subjects were explained with the experimental protocol and asked to sign the informed consent form prior to the experiment.

2. Participants

The thigh muscles were studied for ninety two healthy volunteers (7 women, 22 men, age range: 21 to 38 years, mean age = 26 ± 3.41 years, BMI (body mass index) range: 18.93 to 33.12; mean BMI = 23.55 ± 3.31) with no muscle abnormalities or histories of muscle disease.

3. Experimental configuration

MRE tests were conducted with a 1.5 T Signa HDx MRI machine (General Electric, Milwaukee, WI, USA). The quadriceps (rectus femoris: RF, vastus intermedius: VI, vastus medialis: VM, vastus lateralis: VL) and sartorius (Sr) muscles were studied in the supine position (Figure 2.10a).

For the characterization of the group of ischio (semitendinosus: ST, semimembranosus: SM, biceps (long and short): BC) and gracilis (Gr) muscles, the subjects were in the prone position (Figure 2.10b). It can be noted that only the supine position could have been used for all the investigated muscles. However, the prone position was used to later characterize the ischio and gracilis muscles in the active state by using the same protocol described, hereafter.

Figure 2.10a shows a homemade ergometer that was used in previous studies (Bensamoun et al., 2006b; Debernard et al., 2011) and which stress the quadriceps muscles. Figure 2.10 shows the right knee positioned in a 30° flexion with the right foot placed on a support and secured with Velcro straps. It can be noted that the present ergometer was used only for the characterization of muscle in passive state. The purpose was firstly to develop the MRE protocols for all the thigh muscles. In future experiments, we have planned to apply these protocols to muscle in active state.

A custom-made Helmholtz surface coil was placed around the thigh and a pneumatic passive driver (silicon tube) consisting of a remote active pressure driver connected to a hose (tube) was wrapped and clamped around the subject's thigh. It can be noted that this tube was the same previously used for the phantom (figure 2.6). For the characterization of the quadriceps and sartorius muscles, the tube was placed on the lower part of the thigh due to a lower thickness of adipose tissue in this area. Subsequently, the tube was moved up to the middle part of the thigh for the investigation of the ischio and gracilis muscles; this enabled a better placement of the driver above a larger volume of muscle. In this study, the mechanical mode of excitation is chosen as compression mode rather than shear mode because the energy of the waves is more efficiently propagating throughout the muscles: as the attenuation is less pronounced in this mode, the shear waves generated deep in the muscle are more present (Sinkus et al., 2005a).

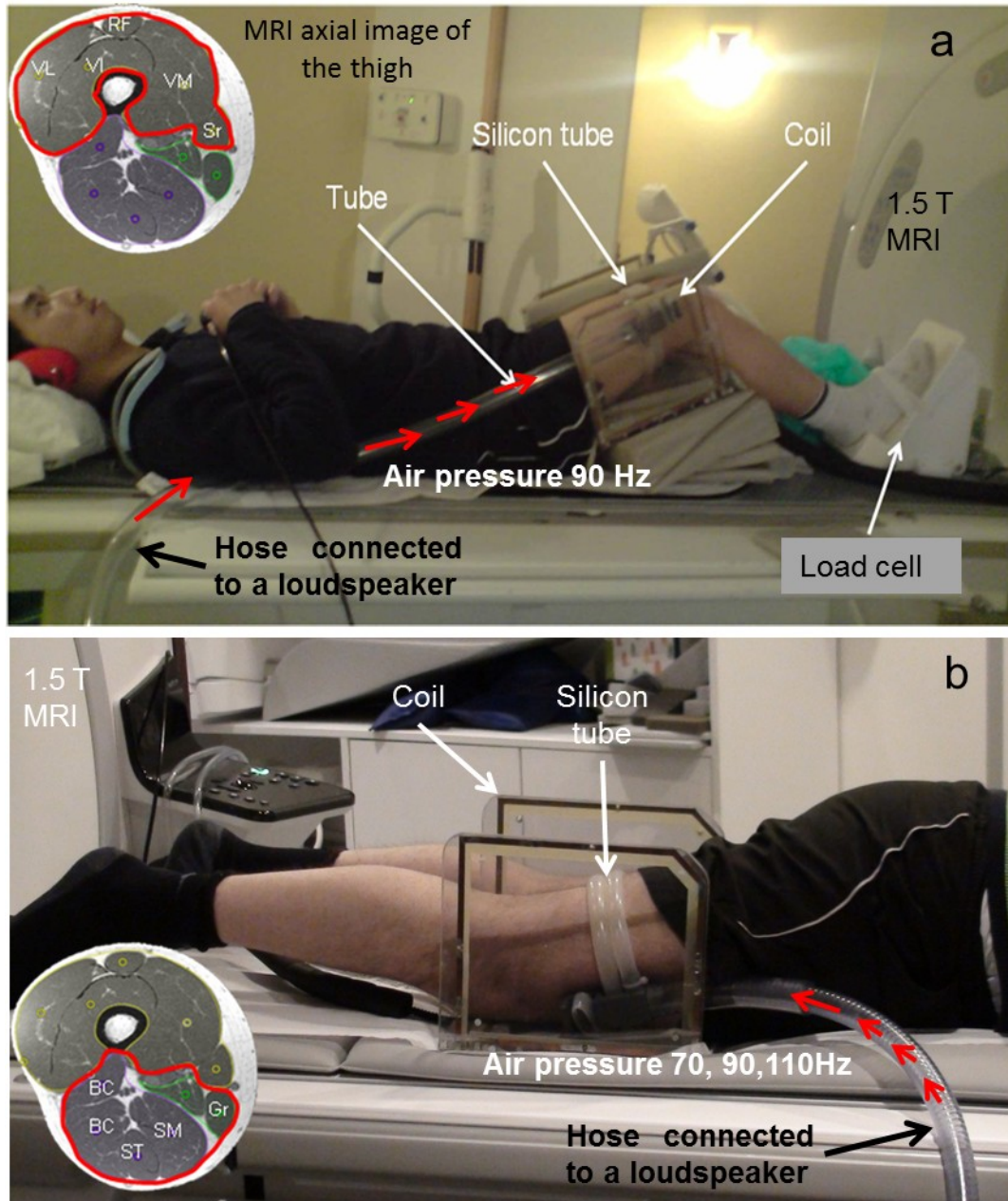


Figure 2.10: MRE setup placed inside a 1.5 T MRI machine. *a:* A participant laid supine on a custom-built ergometer to characterize the quadriceps (VL, RF, VI, and VM) and sartorius (Sr) muscles. *b:* Participant laid in prone position to analyze the ischio (ST, SM, BC) and gracilis (Gr) muscles. Waves were generated at 70 Hz, 90 Hz and 110Hz through a pneumatic driver (silicon tube) attached around the thigh muscles, where a coil was placed. VL: vastus lateralis, RF: rectus femoris, VI: vastus intermedius, VM: vastus medialis, Sr: sartorius, ST: semitendinosus, SM: semimembranosus, BC: biceps, Gr: gracilis.

4. Acquisition of the anatomical and phase images of the muscle

A series of axial scout images were acquired along 20 cm of the thigh with a 2D gradient echo (GRE) MRE sequence. The axial image represented all the distribution of the muscles was selected. Subsequently, five different orientations of imaging planes (IP) (Figure 2.11a) were manually conducted on the axial image of the investigated muscle (represented in red, Figure 2.11a). Each orientation corresponds to a protocol to characterize specific muscles. The accuracy of the orientation of the imaging plan is an important part of the MRE protocol. Thus, the orientation for each imaging plane was slightly rotated, and it was found that a range of ± 4 degrees was acceptable to visualize a clear propagation of the wave.

It can be noted that these orientation of the IP are specific to each muscle due to the muscle fiber orientation and to the localization of the muscle within the thigh (surface vs deep).

Subsequently, sagittal images (Figure 2.11B) showed the entire muscle along the thigh where a clear propagation, represented by a measurable wavelength, of the shear waves was tracked (Figure 2.11C). Moreover, the five sagittal images (Figure 2.11B) could be used as a muscle shape reference to accurately place the imaging plan.

The MRE pulse sequence included a motion-encoding gradient which oscillated, in the Z-direction, at the same frequency as the driver (70, 90, 110 Hz) and was used to image the displacement of the shear waves. Thus, the phase image (Figure 2.11C) was recorded with a GRE sequence, 256×256 acquisition matrix, and two opposite polarities of the motion-encoding gradient having a 2.2 G/cm maximum gradient amplitude limit, a flip angle of 45°, a 24 cm field of view and a slice thickness of 5 mm. Four offsets were recorded for the nine thigh muscles in a relaxed condition.

Periodic variations in air pressure were induced inside the tube at different frequencies 70, 90 and 110 Hz, (frequency: f), resulting in the propagation of acoustic waves within the muscles. These frequencies were chosen as optimal based on previous MRE experiments on thigh muscle with the present tube driver (Bensamoun et al., 2006b; Domire et al., 2009). For each imaging plan, the scan time at 70Hz, 90Hz and 110Hz was 38s with TR/TE of 57.2ms / 26.4 ms, 40s with TR/TE of 55.6ms / 23.2 ms and 33s with TR/TE of 54.6ms / 21.2ms, respectively.

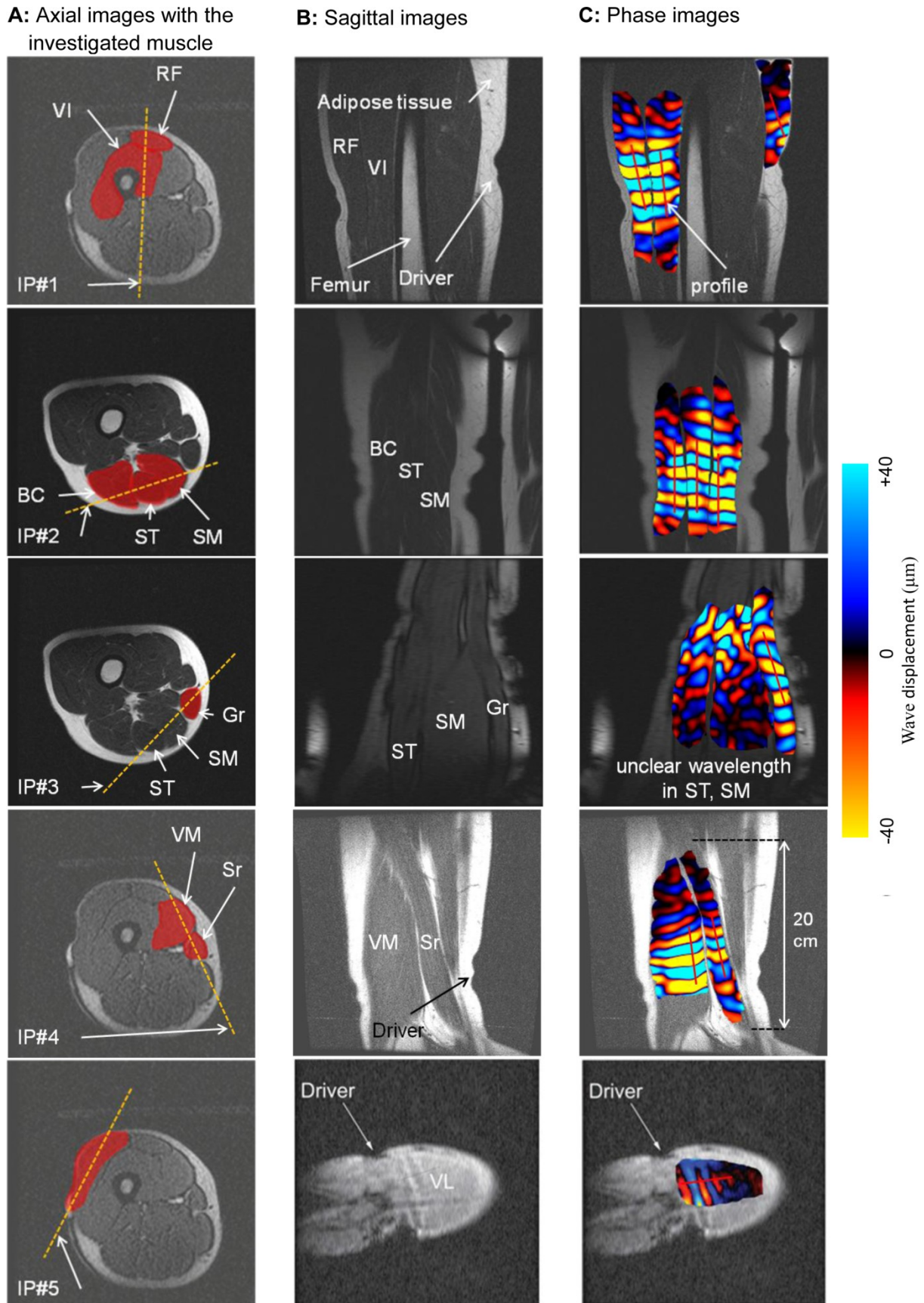


Figure 2.11: Illustration of the three MRE steps to obtain the phase image. A (step #1): The first column showed the orientation of the imaging plan (IP) as represented by a dashed line,

within the target muscle. B (step #2): Sagittal images obtained from step #1 and represented the investigated muscles along the thigh. C (step #3): MRE sequence was performed on the selected sagittal image leading to the acquisition of the phase image, representing the displacement of the shear waves within the muscle.

5. Phase Image Processing and Data Analysis

- Elastic property

The recorded phase images underwent the same post-processing as the phantom (p98, 2.3) by applying a mask, which removed the noise located in the background of the image. In addition, directional filter oriented along the direction of wave propagation, combined with a Butterworth spatial filter were applied to simultaneously remove interfering waves, longitudinal waves, and noise (Manduca et al., 2003). Then, the same operator manually drew a profile within an accuracy of 5° in the direction of the wave propagation following the muscle fascicle paths, inside the following four investigated muscles (Gracilis, Semimembranosus, Semitendinosus and Biceps) in order to calculate the wavelength (λ), which is represented by the distance between consecutive peaks (Figure 2.12).

Assuming that the muscle was linearly elastic, isotropic, homogeneous and incompressible, the shear modulus (μ), which represented the local elasticity, was calculated using the following equation $\mu = \rho \cdot (f \cdot \lambda)^2$, where ρ is the muscle density and assumed to be close to that of water (i.e., 1000 kg/m³).

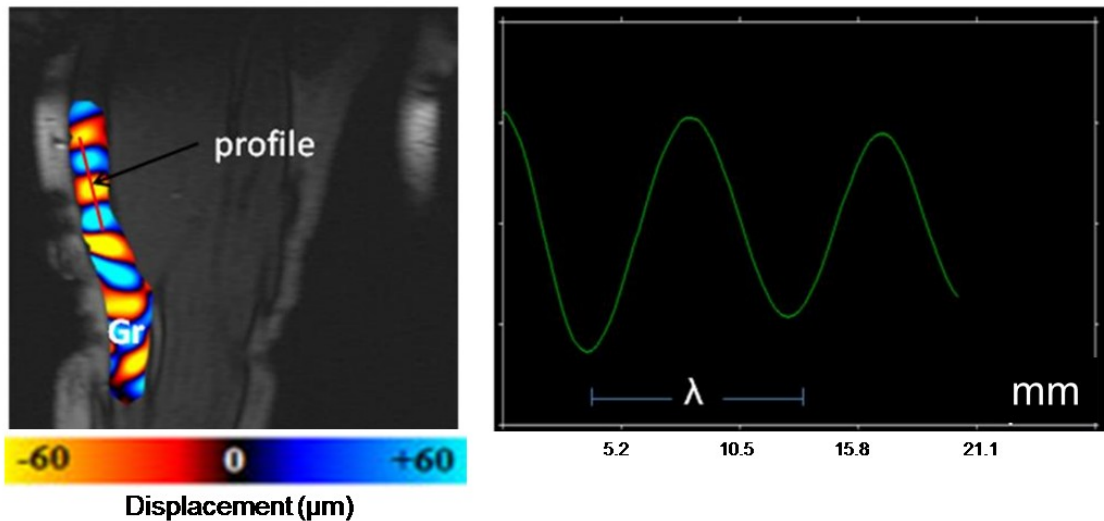


Figure 2.12: Behavior of the shear wave ($f=90\text{Hz}$) along the profile placed in the gracilis (Gr) muscle.

- **Viscoelastic property**

The same theory as for the one applied for the determination of the viscoelastic properties of the phantom was used. Multi frequency MRE tests were performed on SM, ST, BC and Gr muscles and phase images were obtained for each muscle at the three different frequencies (Figure 2.13).

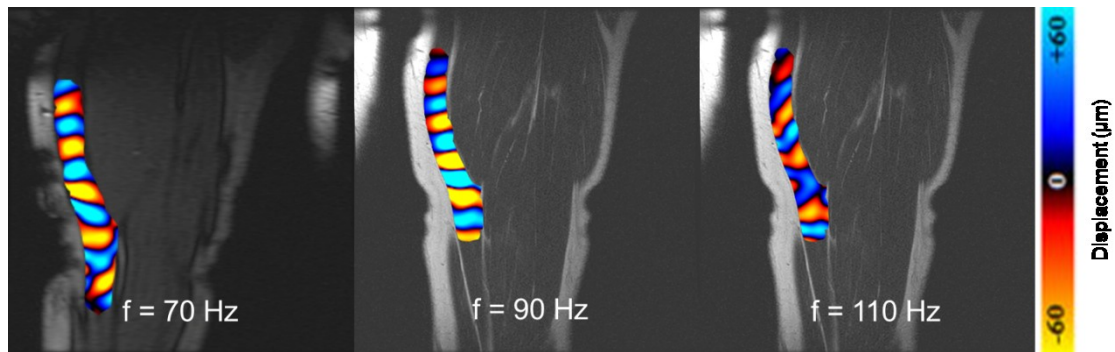


Figure 2.13 : Phase images of Gr muscle at different frequencies (70, 90, 110 Hz)

The complex shear modulus $\underline{G}(w)$ was also calculated based in the viscoelastic theory previously described for the homogeneous phantom (P98).

Phase wave images were first unwrapped and filtered by directional bandpass Butterworth filter to suppress compression waves component and reduce the noise (Manduca et al., 2003).

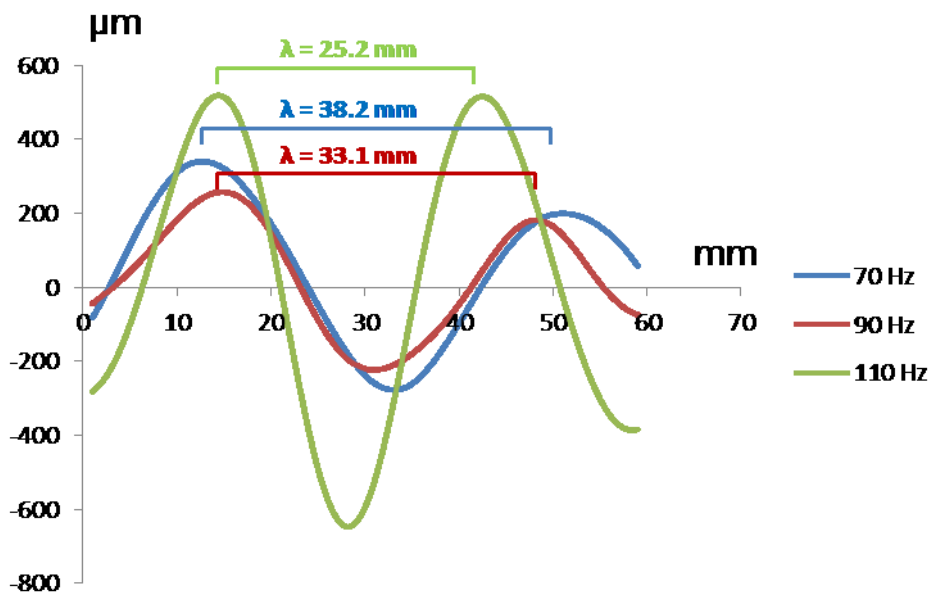


Figure 2.14: Representation of the wavelengths (λ) measured within the gracilis (Gr) muscle, along the red profile, for the three frequencies (70, 90, 110 Hz).

6. Statistical analysis

A Friedman test, post-hoc t-test (Kolmogorov-Smirnov), Analyses of variance (ANOVA) and Student's paired t-test were performed with Statgraphics 5.0 (Sigma Plus, Maryland, USA) software to compare the shear moduli and viscoelastic parameters between the muscles and the subcutaneous adipose tissues.

- Bensamoun, S.F., Ringleb, S.I., Littrell, L., Chen, Q., Brennan, M., Ehman, R.L., and An, K.-N. (2006). Determination of thigh muscle stiffness using magnetic resonance elastography. *J. Magn. Reson. Imaging* 23, 242–247.
- Debernard, L., Robert, L., Charleux, F., and Bensamoun, S.F. (2011). Characterization of muscle architecture in children and adults using magnetic resonance elastography and ultrasound techniques. *J. Biomech.* 44, 397–401.
- Domire, Z.J., McCullough, M.B., Chen, Q., and An, K.-N. (2009). Wave attenuation as a measure of muscle quality as measured by magnetic resonance elastography: Initial results. *J. Biomech.* 42, 537–540.
- Klatt, D., Papazoglou, S., Braun, J., and Sack, I. (2010). Viscoelasticity-based MR elastography of skeletal muscle. *Phys. Med. Biol.* 55, 6445–6459.
- Manduca, A., Lake, D.S., Kruse, S.A., and Ehman, R.L. (2003). Spatio-temporal directional filtering for improved inversion of MR elastography images. *Med. Image Anal.* 7, 465–473.
- Qin, E.C., Jugé, L., Lambert, S.A., Paradis, V., Sinkus, R., and Bilston, L.E. (2014). In Vivo Anisotropic Mechanical Properties of Dystrophic Skeletal Muscles Measured by Anisotropic MR Elastographic Imaging: The mdx Mouse Model of Muscular Dystrophy. *Radiology* 132661.
- Sinkus, R., Tanter, M., Catheline, S., Lorenzen, J., Kuhl, C., Sondermann, E., and Fink, M. (2005). Imaging anisotropic and viscous properties of breast tissue by magnetic resonance-elastography. *Magn. Reson. Med.* 53, 372–387.

CHAPTER 3

RESULTS

CHAPTER 3 RESULTS	111
A. Phantom study	113
1. Elastic properties of the phantoms as a function of the:	113
1.1 Concentration of plastisol	113
1.2 Type of drivers	113
2. Viscoelastic properties of the phantoms:	116
2.1 Hyper-Frequency Viscoelastic Spectroscopy (HFVS) tests	116
2.2 Multifrequency MRE tests	117
B. Muscle thigh study.....	119
1. Propagation of the shear waves within the nine muscles.....	119
2. Comparison of the elastic property between the nine muscles at rest condition	121
3. Comparison of the viscoelastic property between the four muscles (ST, SM, BC, Gr) at rest condition using rheological model	122

A. Phantom study

1. Elastic properties of the phantoms as a function of the:

1.1 Concentration of plastisol

Figure 3.1 showed the recorded phase images, obtained for the homogeneous phantoms (without fiber) composed of 50% (Figure 3.1A) and 70% (Figure 3.1B) of plastisol concentration. A clear visualization of the wave propagation was observed within the phantoms. An increase of the wavelength (λ) was obtained when the plastisol concentration was increased (Figure 3.1B₁). The shear modulus measurements for the phantoms at 50% and 70% of plastisol were $\mu_{50\%} = 2.40 \pm 0.18$ kPa and $\mu_{70\%} = 6.24 \pm 0.21$ kPa, respectively. These elastic properties were similar to the previous elastic properties measured for passive ($\mu = 3.83 \pm 0.24$ kPa) and active ($\mu = 7.33 \pm 1.23$ kPa) thigh muscle (Debernard et al., 2011b).

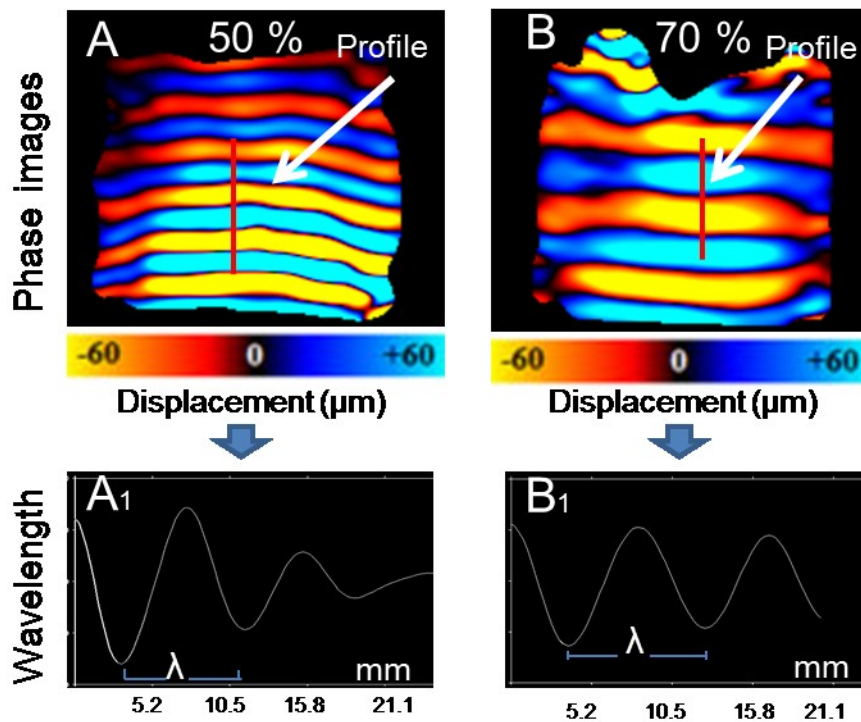


Figure 3.1: A-B: phase images obtained from MRE tests performed on phantoms with different plastic concentrations. A₁-B₁: Behaviors of the waves traveling along the red profile.

1.2 Type of drivers

Different pneumatic drivers were tested on the phantom (50%) composed of fiber inclusion, in order to analyze the impact of the driver on the shear wave displacement. The

results of the phase images, acquired through axial and sagittal scan plans, using the round pneumatic (Figure 3.2) and the silicone tube (Figure 3.3) drivers at the same frequency (90 Hz) are presented hereafter.

Using the round driver (Figure 3.2), the shear modulus measured, along the red profile, on the axial ($\mu_{\text{axial}} = 2.94 \pm 0.18$ kPa) and sagittal ($\mu_{\text{sagittal}} = 3.04 \pm 0.21$ kPa) plans were in the same range. The shear modulus was the same, for each scan plane, in the media with and without inclusion.

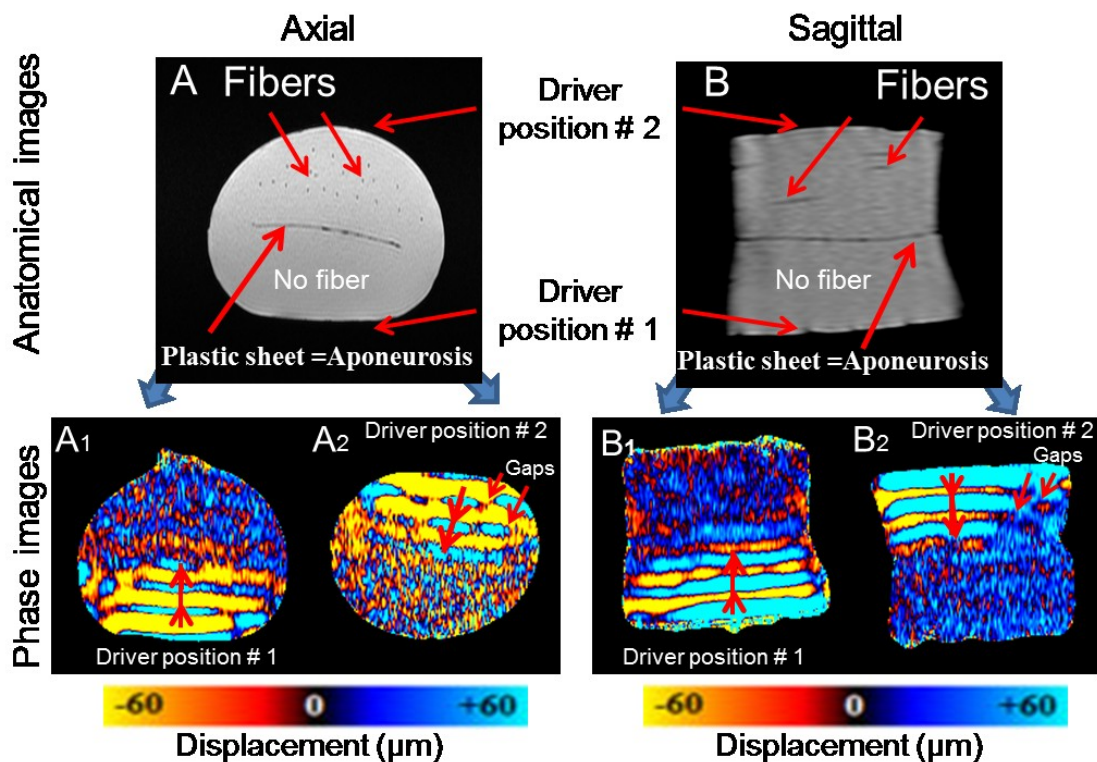


Figure 3.2: A-B: Axial and sagittal anatomical images of the phantom (50%) where the fibers and plastic sheet are localized. Phase images obtained through MRE experiments performed at 90Hz with the round driver in contact with the media without inclusion (A1-B1) and with inclusion (A2-B2). Red arrows indicate the direction of the wave propagation.

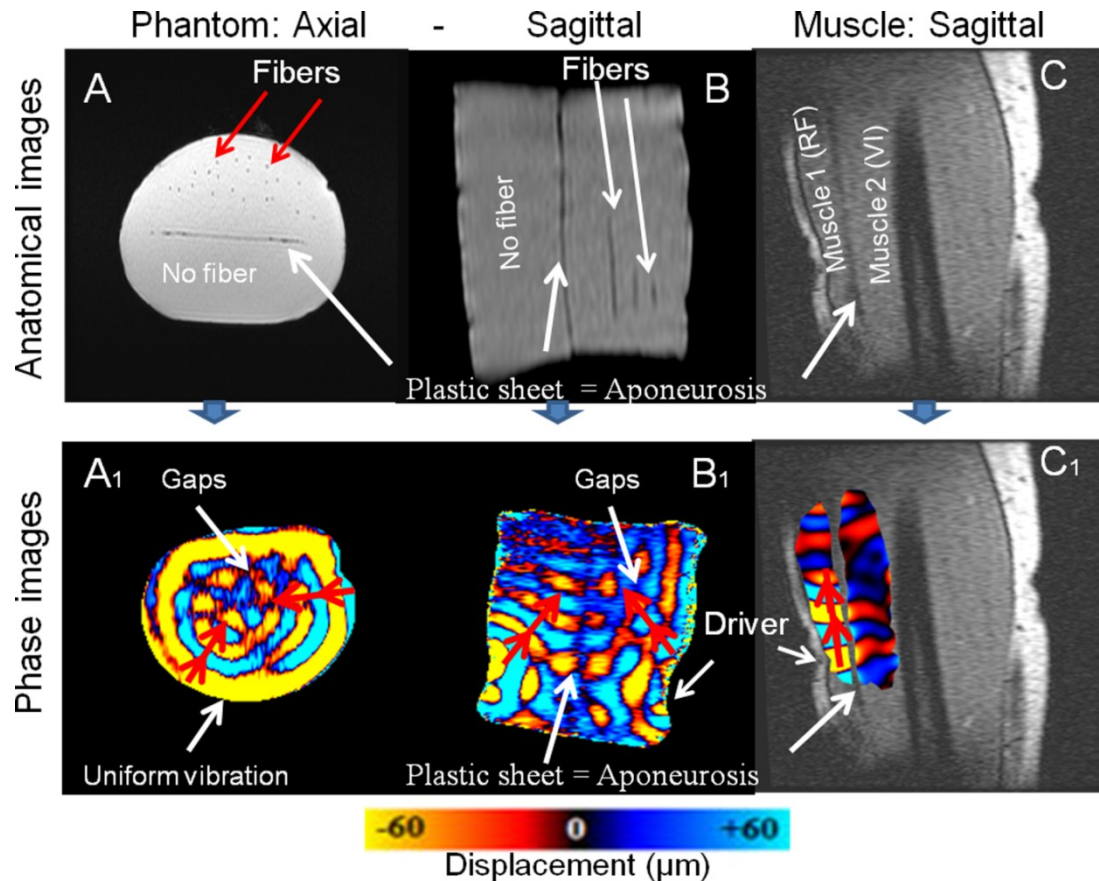


Figure 3.3: A-B-C: Views of the axial (A) and sagittal (B) anatomical images of the phantom (50%) with inclusion and the muscle (C). A₁-B₁: Result of the MRE experiments (90Hz) performed with the tube driver attached around the phantom. C₁: MRE tests (90Hz) performed on thigh muscle. Wave direction indicated by arrows along the red profile.

Using the tube driver (Figure 3.3), the shear modulus measured on the axial ($\mu_{\text{axial}} = 4.47 \pm 0.51$ kPa) image was approximately the same as for the one measured through the sagittal plan ($\mu_{\text{sagittal}} = 4.24 \pm 0.25$ kPa). Moreover, similar elastic properties were found in both side of the phantom.

The comparison of stiffness between the axial and sagittal acquisitions revealed the same range whatever the drivers are. This result demonstrated the homogeneous stiffness inside the phantom.

The comparison of the shear modulus obtained with both drivers showed an effect of the type of driver on the stiffness value. Indeed, higher values ($\mu_{\text{round driver}} = 3.04 \pm 0.21$ kPa vs $\mu_{\text{tube driver}} = 4.24 \pm 0.25$ kPa) were found with the tube driver.

Different shear wave behaviours were found with both drivers. Indeed, Figure 3.2 showed the results of the shear wave displacement when the round driver was placed below (Figure

3.2A₁-B₁) and above (Figure 3.2A₂-B₂) the phantom. It can be noted that the shear wave did not pass through the plastic sheet which plays the role of a separation (aponeurosis) between two muscles. The same result was obtained with the tube driver (Figure 3.3B₁) and a sliding of the wave along the plastic sheet was also visualized. The same phenomena occurred for in vivo MRE muscle study (Figure 3.3C₁).

For both drivers, a uniform propagation of the wave was observed in the media without inclusion. However, the wave behavior was sensitive to the presence of the fibers. Gaps were identified in the media with fiber inclusions (Figure 3.2A₂-B₂ and Figure 3.3A₁-B₁). Similar shear modulus was found in the media with and without inclusion, likely due to the unload fibers.

Figure 3.3A₁ revealed a clear circular wave propagated all around the phantom. This result demonstrated a uniform repartition of the vibration inside the tube which is attached around the phantom. At the opposite, a local source of vibration was observed with the round driver. This result means that this type of driver must be placed close to the investigated tissue.

2. Viscoelastic properties of the phantoms:

2.1 Hyper-Frequency Viscoelastic Spectroscopy (HFVS) tests

The HF viscoelastic spectroscopy technique was performed at a large range of frequency (10-500 Hz) on the small phantom (50%). Within this large frequency range, only the three frequencies (60, 80, 100Hz) were used to compare with those applied during MRE tests. The results revealed an increase of the elastic properties (G') as a function of the frequencies (Figure 3.4A). In addition, the viscous properties (G'') revealed also an increase as a function of the frequencies (Figure 3.4B).

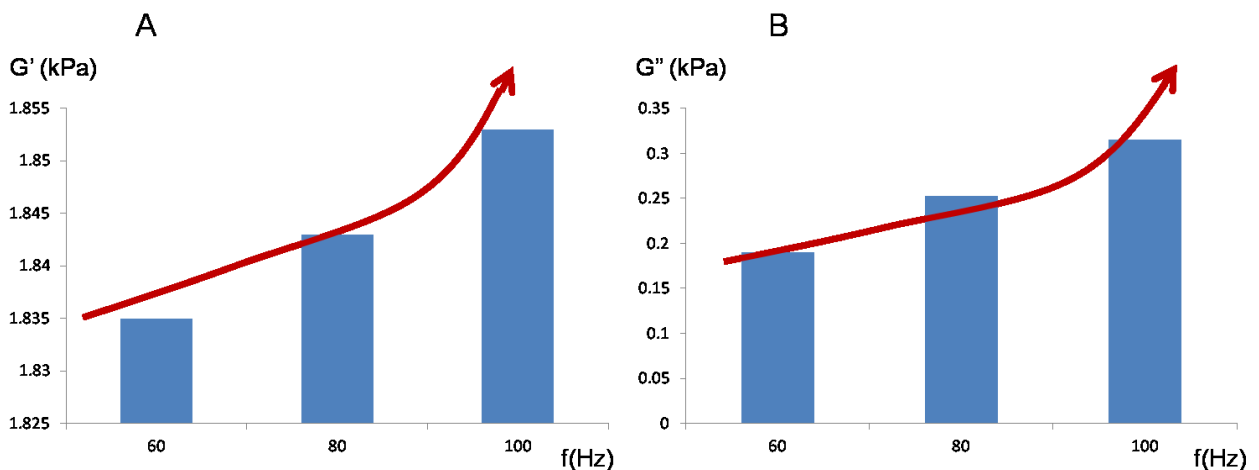


Figure 3.4: Viscoelastic parameters (G' , G'') measured by rheometer

2.2 Multifrequency MRE tests

The phase images recorded on the large homogeneous phantom (50%) showed a decrease of the wavelength as a function of the frequency:

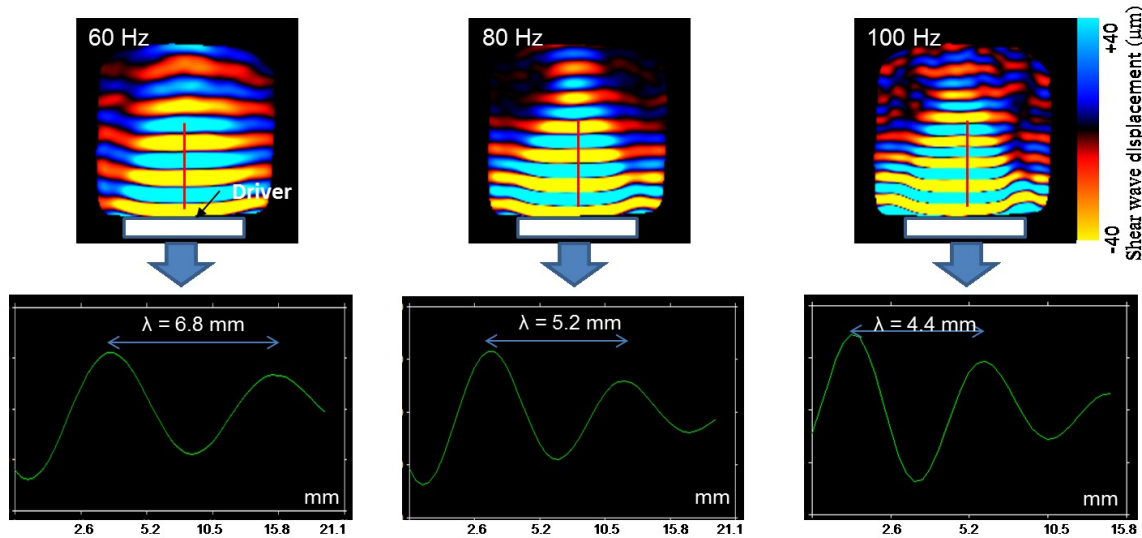


Figure 3.5 : Behaviours of the wave obtained at 60, 80 and 100 Hz

From the experimental wave behaviours, the wavelengths and the attenuation parameters were measured at the different frequencies (60, 80, 100 Hz), to calculate the elastic (G') and the viscous (G'') data.

Method	Parameter	f = 60 Hz	f = 80 Hz	f = 100 Hz
MR elastography	G' (kPa)	1.358 ± 0.013	1.579 ± 0.004	1.574 ± 0.015
	G'' (kPa)	0.2129 ± 0.0092	0.3319 ± 0.0016	$0.4162.0247$

Table 3-1: Experimental viscoelastic data for the large phantom (50%)

Table 3.2 showed the results of the dynamic viscoelastic (G' , G'') parameters obtained with the HFUS technique. It can be noted that our post processing method to experimentally evaluate G' is slightly underestimating using MMRE technique at each frequency (-26 % for 60Hz, -14.3% for 80Hz and -15.1% for 100Hz)

At the opposite, the G'' values are overestimate with MMRE technique compared to HFVS tests: +12%, +31.2% and +32% at 60 Hz, 80 Hz and 100 Hz, respectively.

For both techniques, the results showed higher G' values compared to G'' . It can be concluded that the present developed phantom has an elastic behavior.

Method	Parameter	f = 60 Hz	f = 80 Hz	f = 100 Hz
Rheometer	G' (kPa)	1.835 ± 0.001	1.843 ± 0.001	1.853 ± 0.001
	G'' (kPa)	0.1902 ± 0.0004	0.2530 ± 0.0005	0.3154 ± 0.0006
MR elastography	G' (kPa)	1.358 ± 0.013	1.579 ± 0.004	1.574 ± 0.015
	G'' (kPa)	0.2129 ± 0.0092	0.3319 ± 0.0016	0.4162 ± 0.0247

Table 3-2: Summary of the viscoelastic parameters (G' , G'') measured with MMRE and HFUS technique at three drive frequencies (mean ± standard deviation).

In conclusion, similar elastic (G') values were obtained with both techniques at 60, 80, 100 Hz. Thus, the spectroscopy technique has validated the elastic properties measured with MMRE technique. In addition, the viscous properties obtained with both techniques also revealed an increase as a function of the frequencies.

B. Muscle thigh study

1. Propagation of the shear waves within the nine muscles

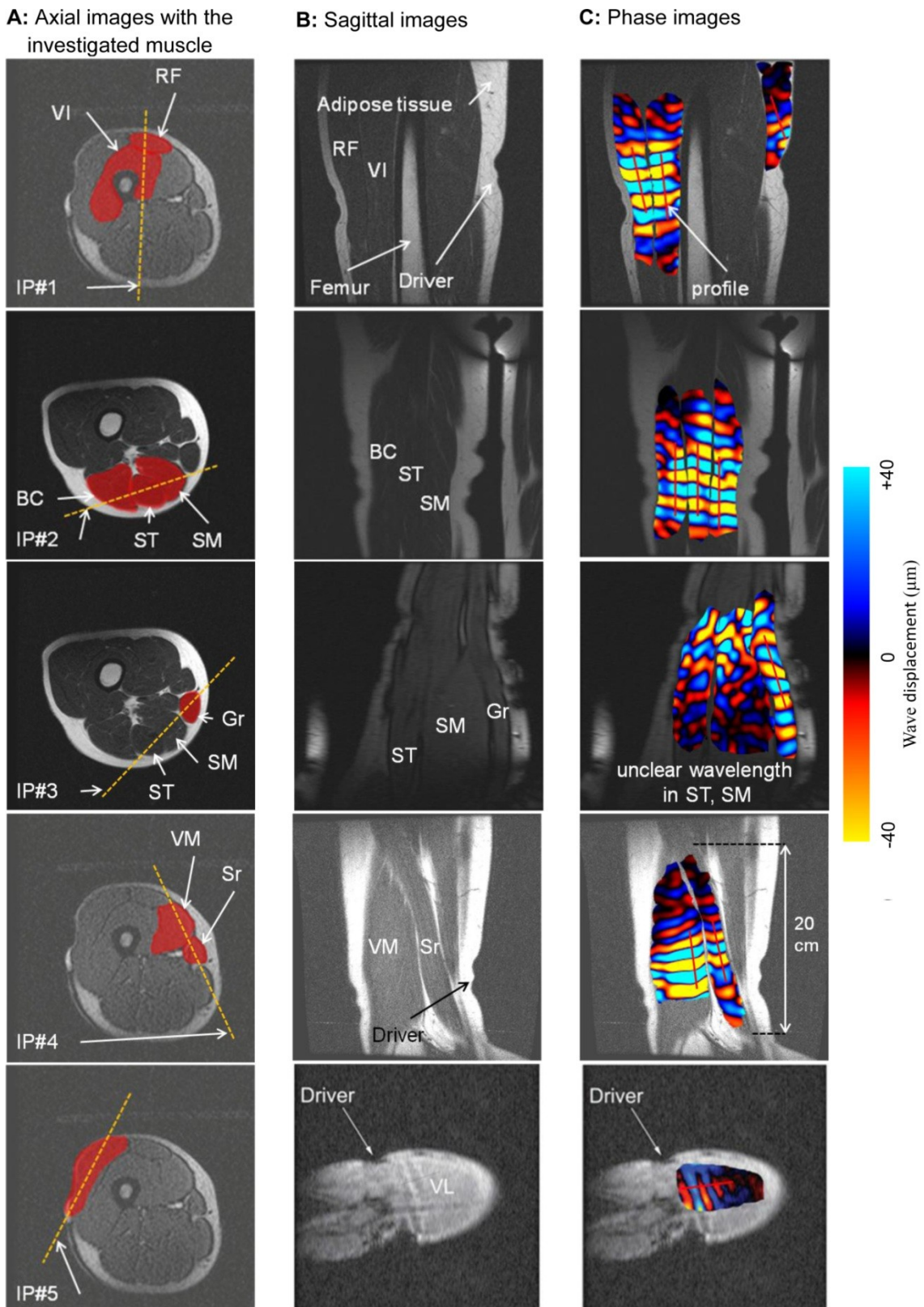


Figure 3.6: Illustration of the three MRE steps to obtain the phase image. A (step #1): The first column showed the orientation of the imaging plan (IP) as represented by a dashed line,

within the target muscle. B (step #2): Sagittal images obtained from step #1 and represented the investigated muscles along the thigh. C (step #3): MRE sequence was performed on the selected sagittal image leading to the acquisition of the phase image, representing the displacement of the shear waves within the muscle.

Figure 3.6 shows the imaging planes used to obtain clear and consistent displacement of the waves for the different muscles. This result was obtained after several rotations of the imaging planes within the investigated muscles.

Imaging plane #1 (IP#1) was vertically placed through the rectus femoris (RF) and vastus intermedius (VI) muscles. IP#1 allowed visualization of wave displacement for both muscles during the same MRE test. Any reflective wave was obtained by the presence of the femur. By using imaging plane #2 (IP#2), all muscles from the ischio group (BC, ST, SM) were characterized in the same phase image (Figure 3.6C). Another imaging plane #3 (IP#3) was used to analyze the gracilis (Gr) muscle. The sagittal image revealed the gracilis, a long (20 cm) and thin muscle, near the SM and ST muscles. Moreover, unclear propagation was obtained through the SM and ST muscles with IP#3, demonstrating the importance of accurate placement of the imaging plane according to muscle architecture and localization within the thigh. Figure 3.7 summarized this last result.

The identification of the imaging plane for the vastus medialis (VM), sartorius (Sr) (IP#4), and vastus lateralis (VL) (IP#5) muscles has been previously determined (Bensamoun et al., 2006). These results are included here (Figure 3.6) to provide complete representation of the MRE protocol and characterization of these thigh muscles.

Characterization of the shear modulus of the adipose tissue was independent of the placement of the imaging plane. The physiological composition of the adipose tissue, being softer than the muscle, provided excellent propagation of the wave within this media around the thigh muscle. A profile was placed, within the subcutaneous adipose tissue layer, in the direction of the wave based on the phase image (Fig 3.6C).

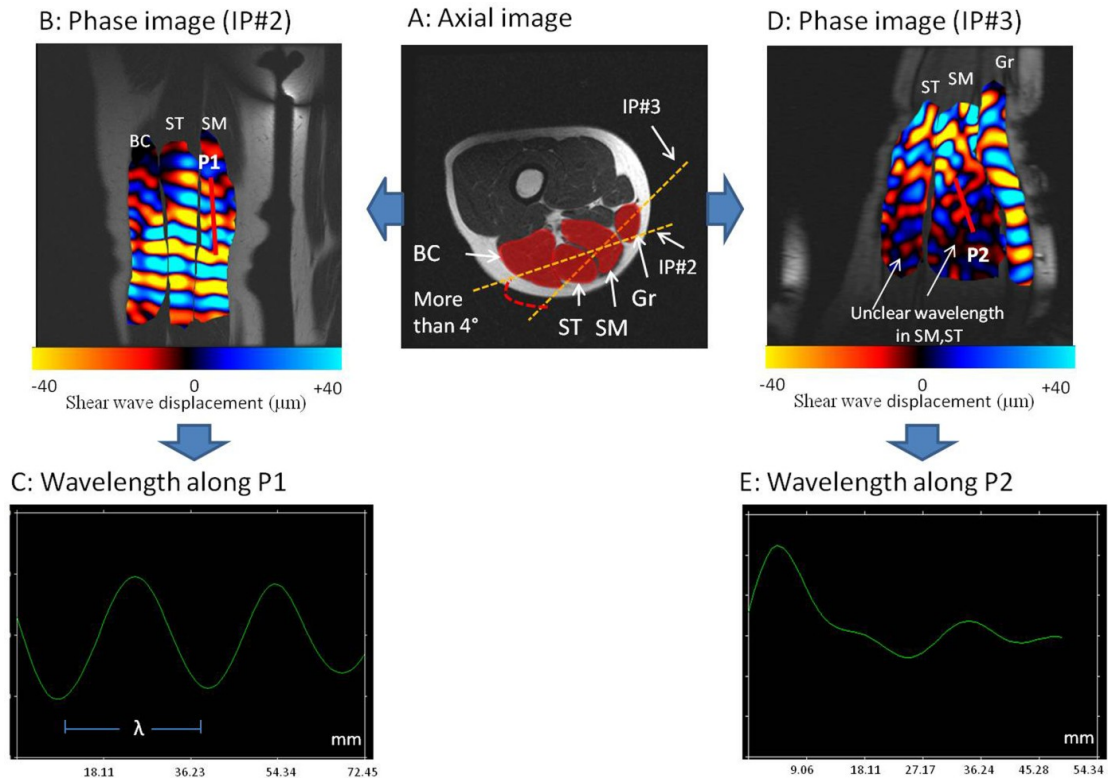


Figure 3.7: Visualization of clear and unclear wave propagation. *A:* Axial image with two different orientations of the imaging planes (IP#2, IP#3) through semimembranosus (SM) and semitendinosus (ST). Phase images showing clear (B) wave with measurable wavelength (λ) (C) and unclear (D) waves with non measurable wavelength (E). P1: Profile 1, P2: Profile 2.

2. Comparison of the elastic property between the nine muscles at rest condition

Due to the high number of acquisitions and time limitations, it was not possible to apply all the imaging planes for each volunteer.

Figure 3.8 shows the values of the shear moduli for the nine muscles and the subcutaneous adipose tissues. Different shear moduli values were found for the muscles in a relaxed state. The gracilis muscle had a significantly ($p < 0.03$) higher shear modulus ($\mu_{Gr} = 6.15 \pm 0.45$ kPa) compared to the other tissues. Two muscles (Sr and ST) also showed significantly ($p < 0.02$) higher shear moduli ($\mu_{Sr} = 5.15 \pm 0.19$ kPa and $\mu_{ST} = 5.32 \pm 0.10$ kPa) compared to the other five muscles (SM, BC, VI, VM, and RF) and the subcutaneous adipose tissue. These remaining tissues (SM, BC, VI, VM, and RF) had similar shear moduli (from $\mu_{RF} = 3.91 \pm 0.16$ kPa to $\mu_{VI} = 4.23 \pm 0.25$ kPa). The shear modulus of the subcutaneous adipose tissue had the lowest ($p < 0.01$) value ($\mu_{adipose\ tissue} = 3.04 \pm 0.12$ kPa) compared to all other

muscles. The reproducibility of the shear moduli was assessed from successive MRE tests with a delay of 5 min between each test.

The reproducibility of the measurements performed twice for all the muscles was evaluated through an intraclass correlation coefficient (ICC) (Fleiss et al., 1986). The result showed an average ICC of ≈ 0.8 (range from 0.72 to 0.87) for the nine muscles and the subcutaneous adipose tissue, attesting to the good reproducibility of the shear moduli.

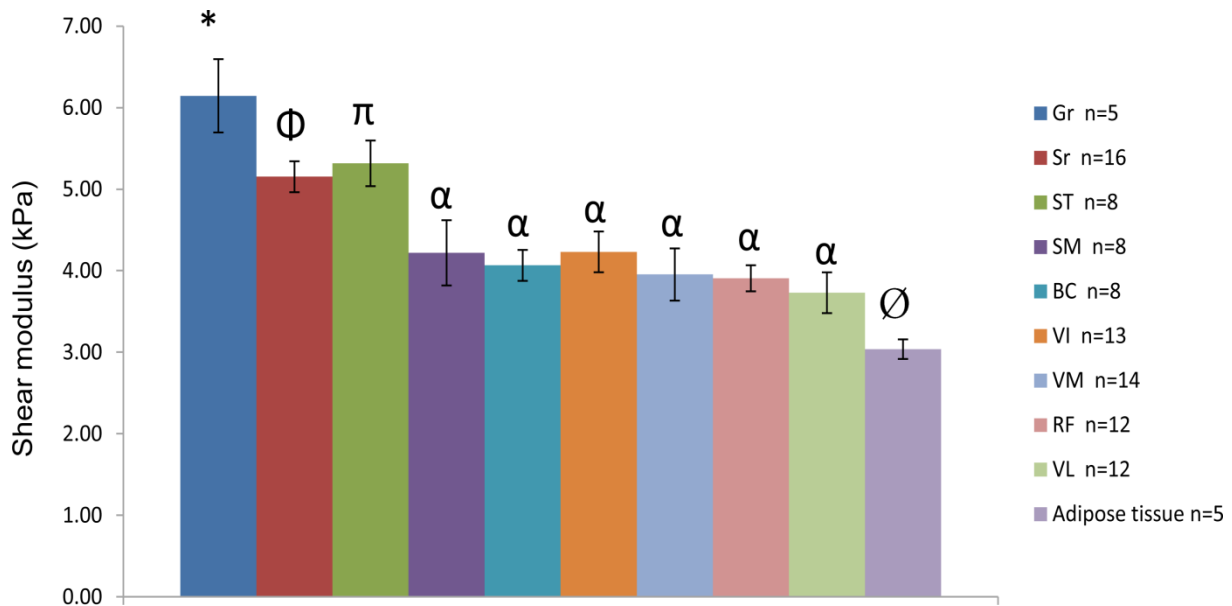


Figure 3.8: Shear modulus (μ) with SEM obtained for the different thigh muscles and adipose tissues.

VL: vastus lateralis, RF: rectus femoris, VI: vastus intermedius, VM: vastus medialis, Sr: sartorius, ST: semitendinosus, SM: semimembranosus, BC: biceps, Gr: gracilis.

*: significantly different to all tissues ($P < 0.03$).

Φ : significantly different to all tissues except ST ($P < 0.02$).

π: significantly different to all tissues except Sr ($P < 0.02$).

α: significantly different to Gr, Sr, ST and adipose tissue ($P < 0.04$).

∅: significantly different to all muscles ($P < 0.01$).

3. Comparison of the viscoelastic property between the four muscles (ST, SM, BC, Gr) at rest condition using rheological model

The results of the MMRE tests performed at different frequencies (70, 90, 110 Hz) on the muscles (ST, SM, BC, and Gr). The phase images (figure 3.9) showed a clear propagation of the shear waves inside the gracilis muscle at different frequencies.

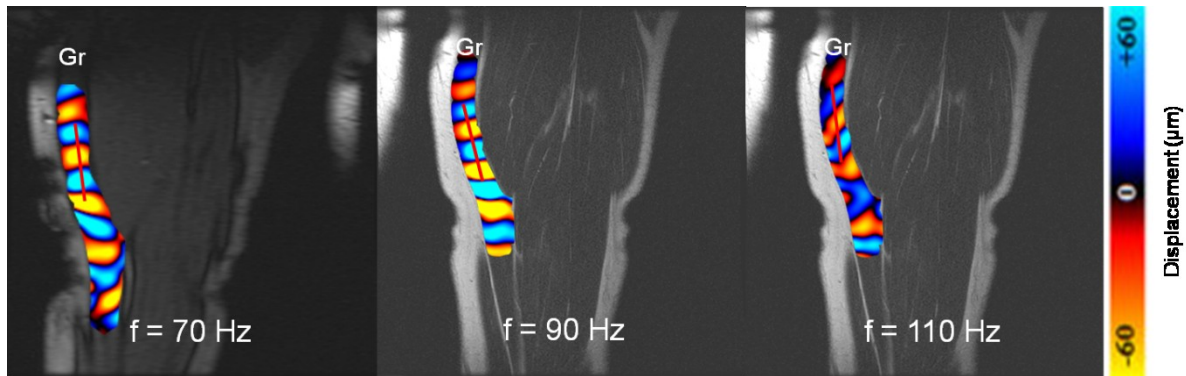


Figure 3.9: Phase images of Gr muscle at different frequencies (70, 90, 110 Hz)

Figure 3.10 shows the behavior of the wavelength for the Gr muscle at the three frequencies. The wave was attenuated along its propagation and had a decrease wavelength (λ) (from 33.1–25.2mm) in accordance with the increase in frequency. Similar results were obtained for the other muscles (ST, SM, and BC). When drawing each profile, care was taken to verify the validity of the waveform and ensure its attenuation value.

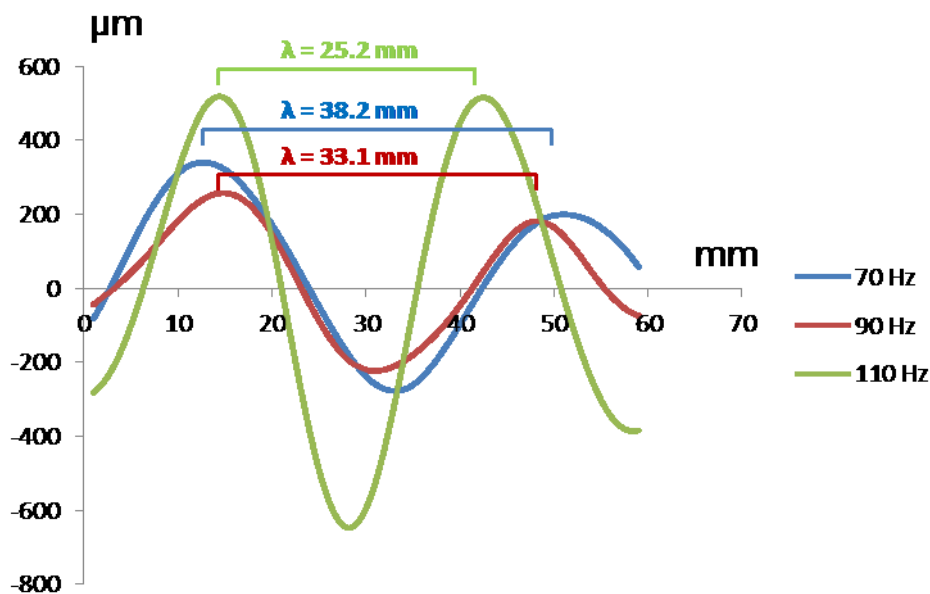


Figure 3.10: Representation of the wavelengths (λ) measured within the gracilis (Gr) muscle, along the red profile, for the three frequencies (70, 90, 110 Hz).

Figure 3.11 presents the results of the experimental viscoelastic (G' and G'') values for the three frequencies. The Gr muscle revealed higher elastic shear modulus (G') values for the three frequencies compared to the other three muscles. In addition, the BC, SM, and ST had

close shear moduli (G') at 90 Hz. This result is likely related to the frequency, which has been previously demonstrated to be optimal at 90 Hz (Bensamoun et al., 2007). Both parameters, (G') and (G'') increased with frequency. The viscous shear modulus showed less variation compared to (G') at each frequency, and between all the muscles. Consequently, the ratio of G''/G' was similar (~ 0.3) at 70 and 90 Hz.

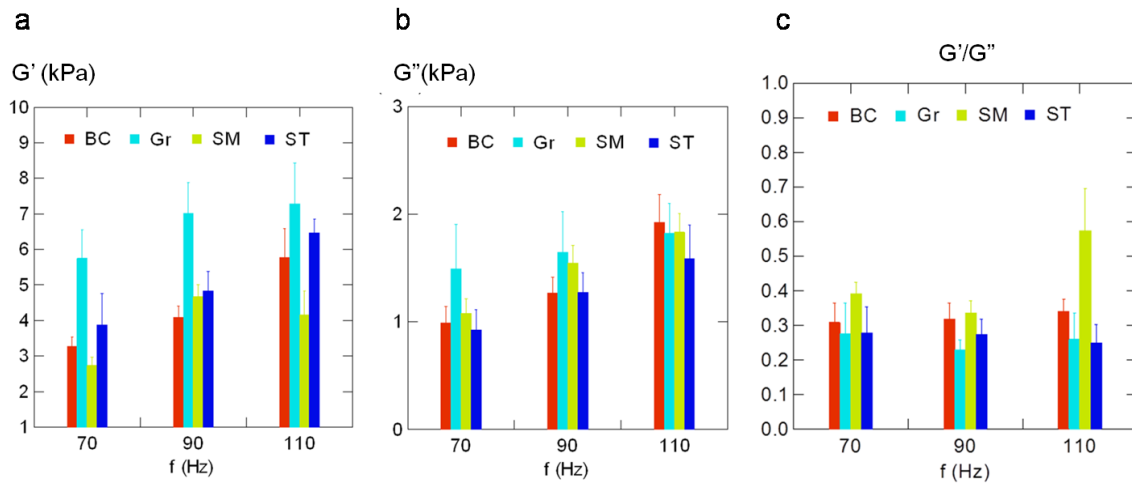


Figure 3.11: Mean \pm SEM of the dynamic experimental viscoelastic parameters (a: G' , b: G'' and c: G''/G') measured with MRE at the three drive frequencies for the semimembranosus (SM), semitendinosus (ST), biceps (BC), and gracilis (Gr) muscles.

Table 3.3 shows the rheological fit for these parameters calculated with the Voigt, Maxwell, Zener, and springpot models, with data taken from the MMRE viscoelastic parameters. The quality of fit was the best for the Zener model for each muscle. This result is represented by the lowest error (χ) value found for this model. This finding supports the fact that the three-parameter Zener model was favored over a two-parameter model. Among the two-parameter models, the springpot also gave a low error value (χ).

Comparisons between the relative errors revealed that $\chi_{90 \text{ Hz}}$ was the smallest value compared to $\chi_{70 \text{ Hz}}$ and $\chi_{110 \text{ Hz}}$. This result was observed for all the models and all the muscles. It can be concluded that the experimental data obtained at 90 Hz gave the best agreement with the rheological models.

Table 3-3: Rheological model parameters (mean \pm SEM) and error of the fit measured from MMRE tests realized from four thigh muscles

Model	Parameter	BC	Gr	SM	ST
Voigt	η (Pa s)	2.51 \pm 0.18	2.85 \pm 0.27	2.93 \pm 0.24	2.20 \pm 0.17
	μ (kPa)	4.38 \pm 0.26	6.88 \pm 0.78	3.86 \pm 0.22	5.00 \pm 0.40
	χ (kPa)	0.35 \pm 0.11	0.46 \pm 0.13	0.42 \pm 0.10	0.41 \pm 0.10
	$\chi_{70\text{ Hz}}$ (%)	12.9 \pm 7.6	11.8 \pm 5.9	17.3 \pm 9.3	9.9 \pm 4.4
	$\chi_{90\text{ Hz}}$ (%)	7.5 \pm 1.1	7.3 \pm 1.3	12.5 \pm 4.3	8.5 \pm 3.5
	$\chi_{110\text{ Hz}}$ (%)	14.0 \pm 2.5	9.6 \pm 1.6	22.5 \pm 5.8	13.7 \pm 3.3
Maxwell	η (Pa s)	25.35 \pm 1.41	55.10 \pm 8.71	18.60 \pm 1.04	40.27 \pm 9.79
	μ (kPa)	4.90 \pm 0.30	7.32 \pm 0.79	4.62 \pm 0.31	5.42 \pm 0.34
	χ (kPa)	0.41 \pm 0.09	0.49 \pm 0.09	0.46 \pm 0.09	0.42 \pm 0.09
	$\chi_{70\text{ Hz}}$ (%)	12.7 \pm 7.7	11.6 \pm 6.0	16.1 \pm 9.1	10.0 \pm 4.5
	$\chi_{90\text{ Hz}}$ (%)	7.3 \pm 1.5	6.9 \pm 1.1	12.3 \pm 4.6	8.7 \pm 3.9
	$\chi_{110\text{ Hz}}$ (%)	13.3 \pm 2.6	9.2 \pm 1.2	22.7 \pm 6.8	13.2 \pm 3.3
Zener	η (Pa s)	3.96 \pm 0.54	6.65 \pm 1.47	4.19 \pm 0.39	4.29 \pm 0.81
	μ_1 (kPa)	3.42 \pm 0.20	5.20 \pm 0.56	2.92 \pm 0.18	3.92 \pm 0.44
	μ_2 (kPa)	6.90 \pm 3.28	6.36 \pm 2.63	7.38 \pm 3.22	3.34 \pm 0.21
	χ (kPa)*	0.31 \pm 0.08	0.37 \pm 0.08	0.38 \pm 0.09	0.35 \pm 0.08
	$\chi_{70\text{ Hz}}$ (%)	10.9 \pm 6.0	9.97 \pm 4.81	14.1 \pm 7.4	8.2 \pm 3.4
	$\chi_{90\text{ Hz}}$ (%)	7.8 \pm 1.6	7.15 \pm 1.33	12.6 \pm 4.4	9.3 \pm 3.9
	$\chi_{110\text{ Hz}}$ (%)	11.9 \pm 1.5	7.77 \pm 1.35	22.0 \pm 6.3	11.4 \pm 2.6
Springpot	η (Pa s)	3.96 \pm 0.54	6.65 \pm 1.47	4.19 \pm 0.39	4.29 \pm 0.81
	μ (kPa)	5.65 \pm 0.33	8.10 \pm 0.80	5.30 \pm 0.29	6.10 \pm 0.38
	α	0.210 \pm 0.009	0.158 \pm 0.012	0.266 \pm 0.010	0.172 \pm 0.022
	χ (kPa)	0.35 \pm 0.08	0.44 \pm 0.09	0.42 \pm 0.09	0.38 \pm 0.08
	$\chi_{70\text{ Hz}}$ (%)	13.5 \pm 6.5	11.1 \pm 4.9	16.5 \pm 8.4	9.3 \pm 3.3
	$\chi_{90\text{ Hz}}$ (%)	7.7 \pm 1.6	7.3 \pm 1.3	12.5 \pm 4.2	8.7 \pm 3.7
	$\chi_{110\text{ Hz}}$ (%)	13.4 \pm 1.6	8.8 \pm 1.8	23.3 \pm 6.2	13.0 \pm 3.0

BC: Biceps; Gr: Gracilis; SM: Semimembranosus; ST: Semitendinosus

* The minimum error χ values are represented in bold.

According to the parameters from the rheological model (Table 3.3), the Zener and springpot models were further compared to muscle viscoelasticity. Figure 3.12 shows the results obtained with the Zener model. We recall that (μ_1) is related to the elasticity of a spring element that is parallel to the Maxwell elements, which is composed of an elastic (μ_2) and a viscous (η) component. For the elastic component (μ_1) (Figure 3.12b), it appeared that the Gr

muscle ($\mu_{1_Gr} = 5.20 \pm 1.26$ kPa) was significantly different to the BC ($\mu_{1_BC} = 3.42 \pm 0.45$ kPa), SM ($\mu_{1_SM} = 2.92 \pm 0.41$ kPa), and ST ($\mu_{1_ST} = 3.92 \pm 0.44$ kPa). The Gr muscle also showed similar greater elastic behavior than the experimental (G') at 90 Hz (Figure 3.11a). The values of Zener's second elastic component (μ_2) were higher than those for (μ_1) for BC, SM, and ST. However, the values of (μ_2) between muscles were not statistically different. Concerning the viscous component (η), a similar range of values was obtained for BC, SM, and ST, with the Gr showing higher values that were not significantly different to those of the other muscles (Figure 3.12).

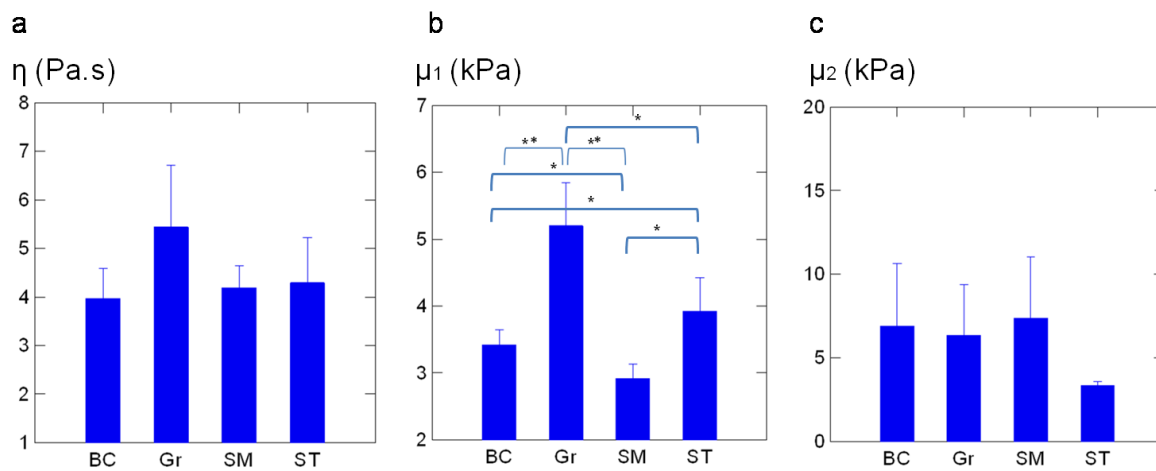


Figure 3.12: Mean \pm SEM of the viscoelastic parameters (**a:** viscosity (η). **b:** elasticity (μ_1). **c:** elasticity (μ_2)) of the four thigh muscles (semimembranosus (SM), semitendinosus (ST), biceps (BC), and gracilis (Gr) muscles) obtained from the Zener model. (** $P < 0.05$, * $P < 0.1$).

Concerning the springpot model (Figure 3.13), significant higher values of (μ) were observed for the Gr muscle ($\mu = 8.1 \pm 1.8$ kPa) compared to the other muscles. This result was similar to the experimental elastic shear modulus obtained at 90 Hz (Figure 3.11a). Concerning the α values, the SM muscle had a higher ($\alpha = 0.266 \pm 0.023$) value compared to the other muscles (Figure 3.13a). Moreover, the trend of α values for each muscle was equivalent to that obtained for the ratio G''/G' at 90 Hz (Figure 3.11c).

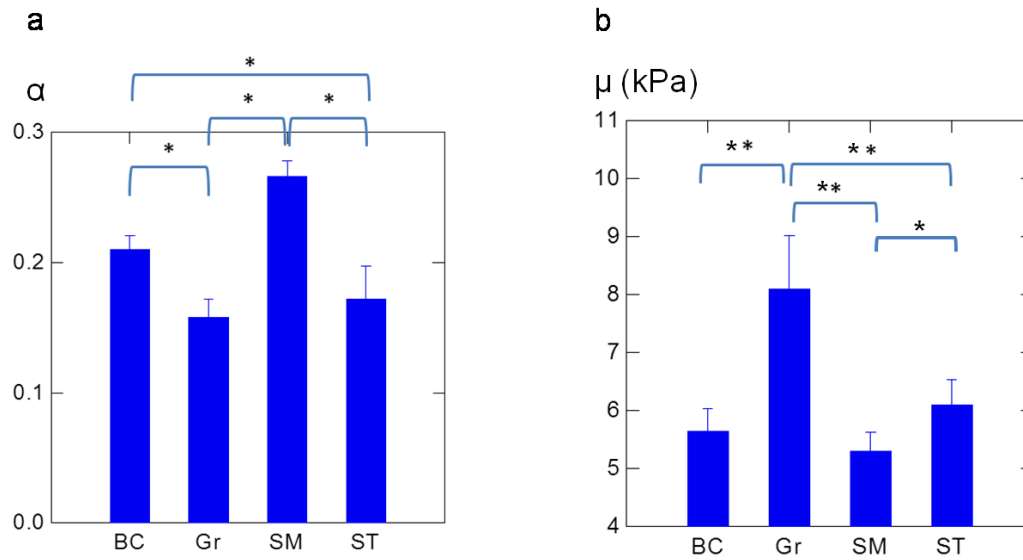


Figure 3.13: Comparison of the viscoelastic parameters (mean \pm SEM) (**a:** ratio α . **b:** elasticity μ).of the four thigh muscles (semimembranosus (SM), semitendinosus (ST), biceps (BC), and gracilis (Gr) muscles) obtained from the springpot model. (** $P < 0.05$, * $P < 0.1$).

CHAPTER 4

DISCUSSION AND PERSPECTIVES

CHAPTER 4	128
DISCUSSION AND PERSPECTIVES	128
A. Phantom study	130
B. Thigh muscle study	131
1. Elastic property	131
2. Viscoelastic property.....	133

A. Phantom study

Skeletal muscle is a physiological complex material, with a hierarchical organization, anisotropic and non-linear behaviors acting in passive and active states. The originality of this study was to develop a phantom able to mimic the architecture (fiber, aponeurosis ...) and the passive mechanical properties of the muscle. The next step will be to incorporate the viscosity of the muscle to have the real viscoelastic behavior of this tissue.

The characterization of the surface muscles is easier compared to the deep ones which are unreachable. Thus, the present cylindrical phantom will allow to test different drivers to improve the deep propagation of the wave, and to test other MRE parameters to develop an optimal protocol as a function of the target muscle.

The comparison between *in vivo* and *in vitro* (Figures 3.3B1- C₁) studies showed a similar behavior of the wave displacement which did not pass through the muscle membrane (aponeurosis). Moreover, equivalent shear moduli were found between *in vivo* and *in vitro* study using the tube driver, usually used for *in vivo* MRE muscle test. These results revealed that the present phantom could be a suitable object to set up new protocols for the deep muscles.

It can be noted that the phantom was placed in a device adapted to stretch the fibers at different levels. A stress muscle could be therefore simulated with the present phantom. In addition, the orientation of the muscle fibers inside the phantom could be changed to better study the behavior of the wave as a function of the fiber orientation. This phantom called “artificial muscle” could be used to set-up diffusion tensor imaging (DTI) sequence for the determination of the muscle anisotropic structure of the muscle. Then DTI and MRE results could be correlated to accurately characterize the muscle behavior.

This test object will be further developed with surrounded environmental tissue such as the adipose tissue. In this study, the *in vivo* elastic properties of the fat tissue was determined and by adjusting the plastic concentration level it could be possible to also simulate this material within the phantom. Moreover, the fibrosis tissue identified within pathological muscle (Duchenne, myopathy) (Bensamoun S. F. et al., 2014) could be also incorporated within the present phantom. Indeed, we have previously measured a stiffer media in

Duchenne muscle in passive condition. However, the displacement of the wave was difficult to follow due to this muscle composition. Thus, the phantom could help to better interpret the changes of the wave behavior within myopathic muscle which are composed of broken muscle fibers and fibrosis infiltration. This “artificial muscle” will help to develop, to optimize, MRE protocol for the characterization of this type of myopathy.

In addition, the homogenous phantoms could be used for the calibration of MRE technique used in clinical practice for liver tissue and new MRE sequence, new drivers, etc... could be tested *in vitro* before to apply *in vivo* protocols. One example in this application was the validation of the present post processing data tested *in vitro* before to apply *in vivo* this method.

This *in vitro* study is a first step toward an artificial muscle allowing the development of *in vivo* MRE protocol, to mimic healthy and pathological muscles.

B. Thigh muscle study

1. Elastic property

The development of non-invasive protocols to assess functional tissue properties has provided useful information. This study shows the feasibility of developing MRE muscle protocols to quantify the shear modulus of all nine healthy thigh muscles. It could be used as a method to identify problems within injured or diseased muscles and to follow the effects of treatments and therapies. These data, obtained from healthy resting muscles, could be used as a baseline model by clinicians. Moreover, human *in vivo* data for modeling the mechanical properties of the muscle are lacking. Thus, our obtained values will be of interest for modeling purposes in implementing the true *in vivo* characteristics of lower limb muscles.

In 2006, the first MRE protocol was published for the characterization of the vasti (VL, VM) and sartorius (Sr) muscles (Bensamoun et al., 2006b). This previous protocol used the same tube driver and similar imaging planes as the present study. Similar ranges of the shear modulus for VL, VM and Sr, were found between both studies. Other studies have established MRE muscle protocols with different drivers, and MR sequences, to also determine the

mechanical properties (i.e., elasticity) of individual muscles as function of age, muscle condition (Debernard et al., 2011b; McCullough et al., 2011) , and disease (Domire et al., 2009), such as myopathy (Bensamoun et al., 2007; Bensamoun et al., 2014). In cases of muscle pathologies or injuries, it appears that different muscles had different physiological and functional changes. Thus, it was important to develop other muscle protocols allowing a complete behavior of a group of muscles. These new shear modulus data will improve our understanding of the changes in muscle elasticity at rest and during a contraction and will enable to adapt the treatment as a function of the muscle damage.

One of the challenges of developing a successful MRE technique is to be able to characterize deep muscles. This method based on the interpretation of the wave propagation along the muscle fiber but this architecture doesn't show through the MRE acquisition. However, ultrasound technique revealed the muscle fiber orientation and the anisotropic behavior by rotating the probe. Nevertheless, ultrasound is limited by the penetrating depth of the beam (Ballyns et al., 2012), and electromyography requires the use of a needle to reach deep muscles. The present study demonstrated the ability and the potential of the MRE technique to quantify the shear modulus of deep muscles in the thigh at rest. In addition, MRI acquisition provides a larger field of view compared with ultrasound and can reveal a complete view of the muscle (e.g., gracilis) from the distal to proximal sides of the thigh. This representation is of importance and can identify the affected muscle area and localize future treatments such as pharmaco-gene therapeutic trials for Duchenne muscular dystrophy (Bensamoun et al., 2014).

The present study has demonstrated different shear moduli values between the muscles. The gracilis, sartorius, and semitendinosus muscles showed higher shear modulus compared with the other thigh muscles. Similar trends were also found for the sartorius and semitendinosus muscles. These differences in shear moduli could have been caused by the position (supine vs prone), the subject's knee angle, and the placement of the scanning planes. However, the muscles (Gr, Sr) were tested in both positions and revealed similar mechanical properties, demonstrating that position had no influence on these two muscles. It is thus assumed that the physiological and architectural compositions of the muscles have impacts on wave displacement. Moreover, the lower shear modulus for the adipose tissue was may be due to its physiological composition which differed to that of muscle tissue (Debernard et al.,

2011). To better analyze the physiological and structural composition of the different muscles, diffusion (Froeling et al., 2012; Li et al., 2014; Scheel et al., 2013; Williams et al., 2013) imaging technique could be performed. Moreover, it would be of interest to couple the MR elastographic sequence with diffusion imaging to characterized the anisotropic (Green et al., 2013b; Qin et al., 2011a, 2013) properties when there is muscle disease (Qin et al., 2014).

The setup of the present MRE muscle protocols is mainly related to the orientation of the imaging planes which are important in achieving good wave displacement. The good reproducibility result showed the reliability of the study. This work is the first step of the development of a muscle atlas that could be improved by including other parameters, such as viscosity (Green et al., 2012; Klatt et al., 2010b; Qin et al., 2011a), anisotropy (Green et al., 2013b), fiber type, muscle volume, and percentages of water and adipose tissues.

The present MRE protocols were developed for muscles in rest condition and it is assumed that the positions (supine and prone) have any impact on the passive elasticity result. However, this statement is not validated in active state due to the initial morphology (length of the fiber, aponeurosis angle) of the muscle which may influence the contractile result. In previous studies, it was demonstrated that shear modulus increased as a function of the level of contraction (Debernard et al., 2011b). Preliminary tests performed on the rectus femoris in a contracted state (10% and 20% MVC) confirmed this statement ($\mu_{RF_relax} = 3.91 \pm 0.16$ kPa, $\mu_{RF_10\%} = 5.54 \pm 0.08$ kPa, and $\mu_{RF_20\%} = 6.56 \pm 0.15$ kPa). Therefore, it is expected that the other muscles have increased elasticity. The present homemade ergometer was adapted to stress the quadriceps muscle and may be further developed to stress other muscles. Preliminary tests were also performed for the vastus intermedius in a contracted state (20% MVC). The phase image shows a non-uniform wave displacement compared to the clear propagation obtained when the muscle was at rest. Consequently, it was difficult to have an accurate measurement of the shear modulus. The next step will be to adapt the developed protocols for muscle in active condition.

2. Viscoelastic property

The novelty of the study is its direct method to extract the *in vivo* viscoelastic parameters from experimental wavelength and attenuation measurements. This data

processing was validated first on the phantom before being applied to muscles. Indeed, it was demonstrated that the experimental G' and G'' values provided by the hyper-frequency viscoelastic spectroscopy technique are in agreement with those measured by our method using multifrequency MRE tests. Moreover, our approach was based on a profile placed within the region of interest on the muscle and within the direction of wave propagation. This made the present method more sensitive to changes in the muscle's mechanical properties. Another advantage of our method was that it did not need to calculate the Laplacian operator $(\frac{\partial^2}{\partial x^2} \underline{U})$ in Eq. 1. Only the locations of the extrema in the waveform were needed.

In this study, our approach was based on the local homogeneity of the biological tissue by local measurement along the profile: thus we assumed that the spatial derivatives of shear modulus $(\frac{\partial}{\partial x} \underline{G})$ were negligible (Sinkus et al., 2005). A more realistic model for muscle tissue may have used the assumption of a transversely isotropic and incompressible medium (Sinkus et al., 2005; Qin et al., 2011). In case of compressibility, the Helmholtz equation $(\rho \omega^2 \underline{U} + \underline{G}(\omega) \frac{\partial^2}{\partial x^2} \underline{U} = 0)$ must be corrected by an additional term for pressure (Sinkus et al., 2010), which requires the acquisition of a 3D MR phase image to calculate the curl operator. In addition, a transversely isotropic medium assumes to reconstruct two shear moduli (parallel and perpendicular to the muscle fibers) with a diffusion tensor imaging sequence (Sinkus et al., 2005). Muscle is a complex biological tissue composed of multiple parameters, which need to be all taken into account but which is not compatible with general clinical investigations due to the increase times of MR acquisition.

This study focused on four relaxed healthy muscles (BC, Gr, SM, ST) and is a follow-on study on work in which we quantified the passive elastic properties of nine thigh muscles. The present results have extended this previous database using passive viscoelastic data from MMRE tests. Comparison of viscoelastic measurements with other studies on muscles is difficult because of the different experimental setups and methods of data processing. Moreover, some studies have characterized isolated muscles, such as the vastus medialis and sartorius (Debernard et al., 2011b), whereas others have measured the viscoelastic properties of a group of femoral muscles (Klatt et al., 2010b). For instance, Klatt et al.'s study used the

same criterion of fit (Eq. [6]; p: 100) as in our present study, but the MMRE tests were performed at a lower frequency range (25–62.5 Hz), with a shear motion driver, and a group of femoral muscles were analyzed. As a consequence, comparisons of the elastic values obtained with the springpot model for the BC ($\mu = 5.65 \pm 0.33$ kPa), Gr ($\mu = 8.10 \pm 0.80$ kPa), SM ($\mu = 5.30 \pm 0.29$ kPa), and ST ($\mu = 6.10 \pm 0.38$ kPa) muscles are not within same range as in Klatt et al.'s study for the femoral muscle ($\mu = 2.68 \pm 0.23$ kPa).

Another example is Debernard et al.'s study (Debernard et al., 2011b), where they used the same driver frequencies for the MMRE tests as in our present study, but their fit of the rheological model differed to ours. Theirs was based on a cost function composed of the speed of the experimental shear wave whereas we used the experimental wavelength and attenuation to measure (G') and (G'') (Eq. [6]; p: 100). Even though, comparisons could be biased, the viscosities (η , Zener) of the vastus medialis (3.57 ± 0.92 Pa.s) and sartorius (6.37 ± 1.13 Pa.s), as reported by Debernard et al., were within the same range as for BC (3.96 ± 0.54 Pa.s), SM (4.19 ± 0.39 Pa.s), ST (4.29 ± 0.81 Pa.s), and Gr (6.61 ± 1.47 Pa.s).

Comparison between the Zener and springpot models showed a similar trend regarding the elastic components for each muscle. The Gr muscle showed higher elastic values in both models compared to the other muscles. This has been reported previously (Bensamoun et al., 2007) and additional spectroscopic investigations are needed to further characterize the structural properties that explain this higher elasticity. The μ_1 parameter from the Zener model could be a marker for the function of the Gr muscle, which is a long spindle-shaped muscle that plays a major role in the flexibility of the hip and knee.

The springpot model also provided an insight into muscle physiology (Klatt et al., 2010b; Anantawaraskul, 2005). Indeed, it is known that the parameter α is determined by the degree of freedom in the underlying network of tissue (Gurtovenko et al., 2005). Thus, the low α -value (0.155) for the phantom revealed a homogeneous media, which is in agreement with the uniform preparation of the phantom. It can be noted that this α value was close to those obtained for the Gr and ST muscles. Higher α values were calculated for BC (0.210 ± 0.020) and SM (0.266 ± 0.023) muscles whereas Gr (0.158 ± 0.012) and ST (0.172 ± 0.022) muscles had significantly lower values. These results indicate a more hierarchical structure for BC and SM muscles, represented by the presence of more cross-bridges between muscle

filaments at the micro-structural level. This range of values was also found by Klatt et al.'s study (Klatt et al., 2010) for the femoral muscles (0.253 ± 0.009). In addition, the trend of α values for each muscle was similar to the experimental ratio G''/G' at 90 Hz. This last result demonstrates that the optimal frequency to characterize muscle using MMRE is 90 Hz.

In conclusion, the present MMRE tests associated with the data processing method showed that the complex shear modulus of passive muscle can be analyzed using two rheological models (Zener, springpot). The elastic and viscous data could be used as a reference for future assessment of muscular dysfunction. Further experiments will be performed on the other thigh muscles under active conditions in order to obtain a complete muscle database of their functional properties.

In perspective, the elastic muscle database for the thigh will be completed with the elasticity of active muscle at different levels of contraction. In the same way, the viscoelastic properties of the remaining thigh muscles will be also characterized.

Anantawaraskul, S. (2005). *Polymer Analysis/Polymer Theory* (Springer Science & Business Media).

Ballyns, J.J., Turo, D., Otto, P., Shah, J.P., Hammond, J., Gebreab, T., Gerber, L.H., and Sikdar, S. (2012). Office-Based Elastographic Technique for Quantifying Mechanical Properties of Skeletal Muscle. *J. Ultrasound Med.* *31*, 1209–1219.

Bensamoun, S.F., Ringleb, S.I., Littrell, L., Chen, Q., Brennan, M., Ehman, R.L., and An, K.-N. (2006). Determination of thigh muscle stiffness using magnetic resonance elastography. *J. Magn. Reson. Imaging* *23*, 242–247.

Bensamoun, S.F., Ringleb, S.I., Chen, Q., Ehman, R.L., An, K.-N., and Brennan, M. (2007). Thigh muscle stiffness assessed with magnetic resonance elastography in hyperthyroid patients before and after medical treatment. *J. Magn. Reson. Imaging* *26*, 708–713.

Bensamoun S. F., Charleux F., and Themar-Noel C. (2014). Elastic properties of skeletal muscle and subcutaneous tissues in Duchenne muscular dystrophy by magnetic resonance elastography (MRE): a feasibility study. *Innov. Res. Biomed. Eng. IRBM*.

Chen, Q., Ringleb, S.I., Hulshizer, T., and An, K.-N. (2005). Identification of the testing parameters in high frequency dynamic shear measurement on agarose gels. *J. Biomech.* *38*, 959–963.

Chen, Q., Ringleb, S.I., Manduca, A., Ehman, R.L., and An, K.-N. (2006). Differential effects of pre-tension on shear wave propagation in elastic media with different boundary conditions as measured by magnetic resonance elastography and finite element modeling. *J. Biomech.* *39*, 1428–1434.

Chen, Q., Bensamoun, S., Basford, J.R., Thompson, J.M., and An, K.-N. (2007). Identification and Quantification of Myofascial Taut Bands With Magnetic Resonance Elastography. *Arch. Phys. Med. Rehabil.* *88*, 1658–1661.

Chen, Q., Basford, J., and An, K.-N. (2008). Ability of magnetic resonance elastography to assess taut bands. *Clin. Biomech.* *23*, 623–629.

Debernard, L., Robert, L., Charleux, F., and Bensamoun, S.F. (2011). Analysis of thigh muscle stiffness from childhood to adulthood using magnetic resonance elastography (MRE) technique. *Clin. Biomech.* *26*, 836–840.

Domire, Z.J., McCullough, M.B., Chen, Q., and An, K.-N. (2009). Wave attenuation as a measure of muscle quality as measured by magnetic resonance elastography: Initial results. *J. Biomech.* *42*, 537–540.

Froeling, M., Nederveen, A.J., Heijtel, D.F.R., Lataster, A., Bos, C., Nicolay, K., Maas, M., Drost, M.R., and Strijkers, G.J. (2012). Diffusion-tensor MRI reveals the complex muscle architecture of the human forearm. *J. Magn. Reson. Imaging* *36*, 237–248.

Green, M.A., Sinkus, R., Gandevia, S.C., Herbert, R.D., and Bilston, L.E. (2012). Measuring changes in muscle stiffness after eccentric exercise using elastography. *NMR Biomed.* *25*, 852–858.

- Green, M.A., Geng, G., Qin, E., Sinkus, R., Gandevia, S.C., and Bilston, L.E. (2013). Measuring anisotropic muscle stiffness properties using elastography. *NMR Biomed.* n/a – n/a.
- Klatt, D., Papazoglou, S., Braun, J., and Sack, I. (2010). Viscoelasticity-based MR elastography of skeletal muscle. *Phys. Med. Biol.* 55, 6445–6459.
- Leclerc, G.E., Debernard, L., Foucart, F., Robert, L., Pelletier, K.M., Charleux, F., Ehman, R., Ho Ba Tho, M.-C., and Bensamoun, S.F. (2012). Characterization of a hyper-viscoelastic phantom mimicking biological soft tissue using an abdominal pneumatic driver with magnetic resonance elastography (MRE). *J. Biomech.* 45, 952–957.
- McCullough, M.B., Domire, Z.J., Reed, A.M., Amin, S., Ytterberg, S.R., Chen, Q., and An, K.-N. (2011). Evaluation of muscles affected by myositis using magnetic resonance elastography. *Muscle Nerve* 43, 585–590.
- Qin, E.C., Sinkus, R., Rae, C., and Bilston, L.E. (2011a). Investigating anisotropic elasticity using MR-elastography combined with diffusion tensor imaging: validation using anisotropic and viscoelastic phantoms. In *Proc. Intl. Soc. Mag. Reson. Med.*, p. 39.
- Qin, E.C., Sinkus, R., Rae, C., and Bilston, L.E. (2011b). Investigating anisotropic elasticity using MR-elastography combined with diffusion tensor imaging: validation using anisotropic and viscoelastic phantoms. In *Proc. Intl. Soc. Mag. Reson. Med.*, p. 39.
- Qin, E.C., Sinkus, R., Geng, G., Cheng, S., Green, M., Rae, C.D., and Bilston, L.E. (2013). Combining MR elastography and diffusion tensor imaging for the assessment of anisotropic mechanical properties: A phantom study. *J. Magn. Reson. Imaging* 37, 217–226.
- Qin, E.C., Jugé, L., Lambert, S.A., Paradis, V., Sinkus, R., and Bilston, L.E. (2014). In Vivo Anisotropic Mechanical Properties of Dystrophic Skeletal Muscles Measured by Anisotropic MR Elastographic Imaging: The mdx Mouse Model of Muscular Dystrophy. *Radiology* 132661.
- Scheel, M., von Roth, P., Winkler, T., Arampatzis, A., Prokscha, T., Hamm, B., and Diederichs, G. (2013). Fiber type characterization in skeletal muscle by diffusion tensor imaging. *NMR Biomed.* n/a – n/a.
- Sinkus, R., Tanter, M., Catheline, S., Lorenzen, J., Kuhl, C., Sondermann, E., and Fink, M. (2005). Imaging anisotropic and viscous properties of breast tissue by magnetic resonance-elastography. *Magn. Reson. Med.* 53, 372–387.
- Sinkus, R., Daire, J.-L., Van Beers, B.E., and Vilgrain, V. (2010). Elasticity reconstruction: Beyond the assumption of local homogeneity. *Comptes Rendus Mécanique* 338, 474–479.
- Williams, S.E., Heemskerk, A.M., Welch, E.B., Li, K., Damon, B.M., and Park, J.H. (2013). Quantitative effects of inclusion of fat on muscle diffusion tensor MRI measurements. *J. Magn. Reson. Imaging* n/a – n/a.

CHAPTER 5

SUMMARIES

A. Summary of the in vitro studies

The objective of this in vitro study was to create a phantom with the same muscle architecture (fiber, aponeurosis ...) and mechanical properties of muscle in passive and active states.

Two homogeneous phantoms were manufactured with different concentrations of plastisol to simulate the muscle elastic properties in passive (50% of plastisol) and active (70% of plastisol) muscle conditions. Moreover, teflon tubing pipes ($D = 0.9$ mm) were thread in the upper part of the phantom (50%) to represent the muscle fibers and a plastic sheet (8 x 15 cm) was also included in the middle of the phantom to mimic the aponeurosis structure.

Subsequently, MRE tests were performed at 90Hz with two different pneumatic drivers, tube and round shapes, to analyze the effect of the type of driver on the wave propagation. The wavelength was measured from the phase images and the elastic properties (shear modulus) were calculated. Both phantoms revealed elastic properties which were in the same range as in vivo muscle in passive (2.40 ± 0.18 kPa) and active (6.24 ± 0.21 kPa) states. The impact of the type of driver showed higher values with the tube (range: 1.2 kPa to 1.53 kPa).

The analysis of the wave behavior revealed a sliding along the plastic sheet as it was observed for in vivo muscle study. The wave was also sensitive to the presence of the fibers where gaps were identified.

A new post processing method was established to measure G' and G'' from experimental multi frequencies (60, 80, 100 Hz) MRE (MMRE) tests and rheological models. This method was tested on the phantom (50%) made without fiber. Cross validation of the viscoelastic (G' , G'') results was made with Hyper-Frequency Viscoelastic Spectroscopy (HFVS). Both techniques showed similar range of values for G' and G'' at the same frequencies. This last result validated our new data processing for the viscoelastic measurement.

B. Summary of the in vivo studies

The objective of this in vivo study was to develop MRE protocols to characterize the elastic properties (shear modulus) of the nine thigh muscles. These tests were performed at a single frequency (90Hz).

Different shear moduli were found between the muscles. The gracilis revealed the highest elastic properties compared to all the other muscles. These different elasticities may be due to different physiological and architectural compositions between the tissues.

Then the viscoelastic properties of the ischio (ST, SM, and BC) and Gr muscles were determined based on our new data-processing method (validated on the phantom 50%) using MMRE tests (70, 90 and 120Hz) and rheological models. The results revealed that two rheological models, zener and springpot, can be used to measure the viscoelastic properties in passive state. A similar trend was found between the experimental ratios G''/G' obtained at 90 Hz and the α value of the springpot model.

The present MRE muscle protocol, and the viscoelastic data base, could be used as non-invasive diagnostic tools to evaluate tissue alterations, the progression of diseases, and the effect of treatments, such as the ongoing therapeutic trials for Duchenne muscular dystrophy.

CHAPTER 6

RESUMES

A. Résumé de l'étude in vitro

L'objectif de cette étude in vitro était de créer un fantôme avec la même architecture musculaire (fibre, aponévrose ...) et les mêmes propriétés mécaniques que le muscle en condition passive et active.

Deux fantômes homogènes ont été fabriqués avec différentes concentrations de plastisol pour simuler les propriétés élastiques du muscle en condition passive (50% plastisol) et active (70% de plastisol). Pour cela, des fils en Téflon ($d = 0,9$ mm) ont été insérés dans la partie supérieure du fantôme (50%) pour représenter les fibres musculaires. De plus, une feuille en matière plastique (8×15 cm) a également été placée au milieu du fantôme pour imiter la structure de l'aponévrose.

Ensuite, des tests ERM ont été effectués à 90 Hz avec deux stimulateurs pneumatiques de différentes formes (tube en silicone, membrane circulaire) pour analyser l'effet du type du stimulateur sur la propagation des ondes. La longueur d'onde a été mesurée à partir des images phase et les propriétés élastiques (module de cisaillement) ont été calculées. Les deux fantômes (50% et 70%) ont montré des propriétés élastiques similaires à celles du muscle à l'état passif ($2,40 \pm 0,18$ kPa) et actif ($6,24 \pm 0,21$ kPa). Le stimulateur en forme de tube a donné des valeurs plus élevées (environ 1,2 kPa à 1,53 kPa).

L'analyse du comportement des ondes a révélé un glissement le long de la feuille plastique. Ce phénomène a aussi été observé in vivo le long de l'aponévrose. L'onde a également été sensible à la présence des fils en téflon car des coupures, des trous, ont été identifiés au cours de la propagation de l'onde.

Une nouvelle méthode de post-traitement a été créée pour mesurer les paramètres G' et G'' à partir de tests ERM réalisés à plusieurs fréquences (60, 80, 100 Hz) et en utilisant des modèles rhéologiques. Cette méthode a été testée sur un fantôme (50%) qui n'avait pas d'inclusion. Les résultats des mesures viscoélastiques (G' , G'') ont été validés avec la technique HFVS (Hyper-Fréquence viscoélastique Spectroscopy). Des valeurs similaires, G' et G'' , ont été obtenues avec les deux techniques. Ce dernier résultat valide la nouvelle méthode de post-traitement pour mesurer les propriétés viscoélastiques.

B. Résumé de l'étude in vivo

L'objectif de cette étude in vivo a été de développer des protocoles ERM pour caractériser les propriétés élastiques (module de cisaillement) des neuf muscles de la cuisse. Ces tests ont été effectués à une seule fréquence (90 Hz).

Différents modules de cisaillement ont été trouvés entre les muscles. Le gracilis a révélé des propriétés élastiques plus élevées que les autres muscles. Ces différentes élasticités peuvent être dues à différentes compositions physiologiques et architecturales entre les tissus.

Ensuite, les propriétés viscoélastiques des muscles ischio (ST, SM, et la BC) et du muscle Gr ont été déterminées en appliquant la nouvelle méthode de post-traitement des données (précédemment validée sur le fantôme 50%) avec des tests ERM multi fréquences (70, 90 et 120 Hz) et en utilisant des modèles rhéologiques. Les résultats ont montré que deux modèles rhéologiques, Zener et springpot, peuvent être utilisés pour mesurer les propriétés viscoélastiques des muscles à l'état passif. De plus, des résultats similaires ont été trouvés entre G''/G' , obtenus expérimentalement à 90 Hz, et la valeur α du modèle de springpot.

Les différents protocoles ERM développés pour le muscle, et la base de données des propriétés viscoélastiques, pourraient être utilisés comme un outil de diagnostic non invasif pour évaluer des altérations des tissus musculaires, pour suivre la progression des maladies, et évaluer l'effet des traitements, tels que les essais thérapeutiques en cours pour la myopathie de Duchenne.

A. Publications

Accepted papers

1. Chakouch MK, Charleux F, and Bensamoun SF, “Definition of imaging plans for quantifying elastic property of nine thigh muscles using magnetic resonance elastography (MRE),” PLoS ONE, 2015.
2. Chakouch MK, Charleux F, Philippe Pouletaut and Bensamoun SF, “Viscoelastic shear properties of in vivo thigh muscles measured by magnetic resonance elastography,” Journal of Magnetic Resonance Imaging, 2015.

B. International Communications

1. Chakouch MK, Charleux F, and Bensamoun SF, “Development of a phantom mimicking the functional and structural behaviors of the thigh muscles characterized with magnetic resonance elastography technique,,” 37TH ANNUAL INTERNATIONAL CONFERENCE OF THE IEEE Engineering in Medicine and Biology Society, Milan, Italy, Aug-2015.
2. Chakouch MK, Charleux F, and Bensamoun SF, “MECHANICAL BEHAVIOURS OF NINE THIGH MUSCLES USING MAGNETIC RESONANCE ELASTOGRAPHY,” 21st Congr. Eur. Soc. Biomech. Prague Czech Repub., July-2015.
3. Chakouch MK, Charleux F, and Bensamoun SF, “Phantoms mimicking the viscoelastic behavior of healthy and fibrotic livers with Magnetic Resonance Elastography technique,” 3rd Int. Conf. Adv. Biomed. Eng (IEEE). Beirut, Sep-2015.
4. Chakouch MK, Charleux F., Bensamoun S.F. “ Quantification of the elastic properties for all the thigh muscles using magnetic resonance elastography (MRE)“. MORAA (Mayo Orthopedic Research Alumni Association) International Symposium. Rochester, MN, USA, 2015

C. National Communications

1. M. K. Chakouch, F. Charleux, and S. F. Bensamoun, “New magnetic resonance elastography protocols to characterise deep back and thigh muscles,,” Comput. Methods Biomech. Biomed. Engin., vol. 17 Suppl 1, pp. 32–33, 2014.